

# Hunting for quantum-classical crossover in condensed matter problems

Nobuyuki Yoshioka,<sup>1,2,3,\*</sup> Tsuyoshi Okubo,<sup>4,3,†</sup> Yasunari Suzuki,<sup>5,3,‡</sup> Yuki Koizumi,<sup>5</sup> and Wataru Mizukami<sup>6,7,3,§</sup>

<sup>1</sup>*Department of Applied Physics, University of Tokyo,  
7-3-1 Hongo, Bunkyo-ku, Tokyo 113-8656, Japan*

<sup>2</sup>*Theoretical Quantum Physics Laboratory, RIKEN Cluster for Pioneering Research (CPR), Wako-shi, Saitama 351-0198, Japan*

<sup>3</sup>*JST, PRESTO, 4-1-8 Honcho, Kawaguchi, Saitama, 332-0012, Japan*

<sup>4</sup>*Institute for Physics of Intelligence, University of Tokyo,  
7-3-1 Hongo, Bunkyo-ku, Tokyo 113-0033, Japan*

<sup>5</sup>*NTT Computer and Data Science Laboratories, Musashino 180-8585, Japan*

<sup>6</sup>*Center for Quantum Information and Quantum Biology,  
Osaka University, 1-2 Machikaneyama, Toyonaka, Osaka, 560-0043, Japan*

<sup>7</sup>*Graduate School of Engineering Science, Osaka University,  
1-3 Machikaneyama, Toyonaka, Osaka 560-8531, Japan.*

The intensive pursuit for quantum algorithms with speedup in terms of computational complexity has further led to this modernized crucial question: *When and how will quantum computers outperform classical computers?* The next milestone in the context of this quantum transcendence is undoubtedly the realization of quantum acceleration in practical problems. Here we provide a clear evidence and arguments that the primary target is likely to be condensed matter physics. Our primary contributions are summarized as follows: 1) Proposal of systematic error/runtime analysis on state-of-the-art classical algorithm based on tensor networks; 2) Dedicated and high-resolution analysis on quantum resource performed at the level of executable logical instructions; 3) Clarification of quantum-classical cusp for ground-state simulation to be within runtime of hours using only a few hundreds of thousand physical qubits for 2d Heisenberg and 2d Fermi-Hubbard models. To our knowledge, we argue that condensed matter problems offer the earliest platform for demonstration of practical quantum advantage that is order-of-magnitude more feasible than ever known candidates, in terms of both qubit counts and total runtime.

## INTRODUCTION

When and how will quantum computers outperform classical computers? Indeed, we have witnessed such achievements of quantum supremacy in some specialized tasks as random sampling by exploiting the quantum computers that are fully exposed to noise [1–5]. We foresee that the precedent milestone after this quantum transcendence is the realization of quantum acceleration for practical problems. In this regard, an outstanding question is the following: *in which problem next?* This involves researchers in broad fields including natural science, computer science, and of course quantum technology.

Studies on quantum acceleration are underway mainly in two areas: cryptanalysis and quantum chemistry. Regarding the former, there has been a significant advancement made since the Shor’s proposal of polynomial time quantum algorithm for factoring integers and finding discrete logarithms [6–10]. Gidney et al. has estimated that a fully fault-tolerant quantum computer with 20 million ( $2 \times 10^7$ ) qubits can solve the 2048-bit RSA cipher in eight hours. This has shown a nearly hundred-fold improvement regarding the spacetime volume of the algorithm over comparable works, which ordinary estimated order of days. Considering that the security of essentially all asymmetric cryptosystems relies on the classical intractability of integer factoring or discrete logarithm findings [11–13], the realizability of Shor’s algorithm is crucial to ensure the robustness of modern and future

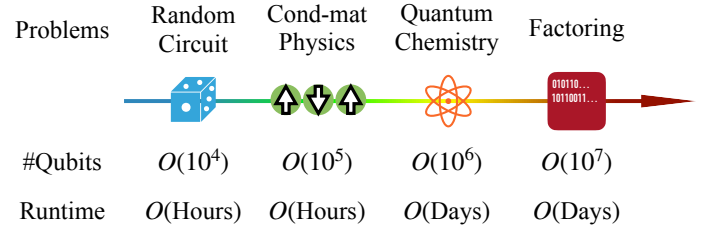


FIG. 1. Schematic diagram for scaling of computational resource required to achieve quantum advantage using fault-tolerant quantum computers.

communication.

The potential impact of speeding up quantum chemical calculations, or the first-principles calculations, is equally huge. Due to its wide application in materials science and life sciences, it has been pointed out that the computational chemistry, although not necessarily quantum chemistry, consumes as much as 40% of HPC resources [14]. Among numerous benchmarks, one of the most prominent target with striking impact is the quantum acceleration in the computation of energies of a molecule called FeMoco in the reaction center of a nitrogen-fixing enzyme [15–18]. With the best current algorithms, the ground-state-energy calculation of FeMoco is expected to take around four days on a fault-tolerant quantum computer with four million ( $4 \times 10^6$ ) physical qubits [18]. Also, Goings et al. have performed

a comparison between quantum computers and the current state-of-the-art heuristic classical algorithm for cytochrome P450 enzymes to suggest that the quantum advantage occurs only in calculations that take place over four days [19].

Practical quantum advantage in two areas have been argued to occur in the time scale of days even with millions of physical qubits, which may not be the ideal target as the earliest application of fault-tolerant quantum computers. The aim of this paper is to shed light on condensed matter physics as a novel candidate (See Fig. 1). We emphasize that the models in condensed matter physics encode various fundamental quantum many-body phenomena, yet its structure is more simple than quantum chemistry Hamiltonians. Lattice quantum spin models and lattice fermionic models are cradles to foster strong quantum correlations that account for quantum magnetism, quantum condensation, topological order, quantum criticality, and so on. Considering the exoticity and abundancy of models, and further the challenge of simulating large-scale systems using classical algorithms even with the state-of-the-art techniques, it would be truly beneficial to reveal the location of the crosspoint based on runtime analysis.

We present our work that contributes to the community in the following three-fold ways: 1) Proposal of systematic analysis method that allows one to estimate runtime to simulate quantum state within target energy accuracy using the extrapolation techniques, 2) End-to-end runtime analysis of quantum resource performed at the level of executable logical instructions, 3) Manifest indication of quantum-classical crosspoint for ground-state simulation to be within *hours* using physical qubits of order  $10^5$ . To our knowledge, this offers the earliest platform of crossover that is both practical and plausible.

## I. TARGET MODELS

Condensed matter physics deals with intricate interplay between microscopic degrees of freedom such as spins and electrons that in many case constitute translationally symmetric structure. Our focus is on lattice systems that not only extract exotic and profound nature of quantum many-body phenomena, but also await to be solved despite the existing intensive studies:

(1) *Antiferromagnetic Heisenberg model*. Paradigmatic quantum spin models frequently involve frustration between interactions as source of complex quantum correlation. One of the most notoriously involved example is the spin-1/2  $J_1$ - $J_2$  Heisenberg model on the square lattice, whose ground state property has been long-lasting problem over decades:

$$H = J_1 \sum_{\langle p,q \rangle} \sum_{\alpha \in \{X,Y,Z\}} S_p^\alpha S_q^\alpha + J_2 \sum_{\langle\langle p,q \rangle\rangle} \sum_{\alpha \in \{X,Y,Z\}} S_p^\alpha S_q^\alpha,$$

where  $\langle \cdot \rangle$  and  $\langle\langle \cdot \rangle\rangle$  denote pairs of (next-)nearest-neighboring sites that is coupled via Heisenberg inter-

action with amplitude  $J_{1(2)}$ , and  $S_p^\alpha$  is the  $\alpha$ -component of spin-1/2 operator on the  $p$ -th site. Due to the strange competition between the  $J_1$  and  $J_2$  interaction, formation of any long-range order is hampered at  $J_2/J_1 \sim 0.5$ , at which quantum spin liquid phase is expected to realize [20–24]. In the following we set  $J_2 = 0.5$  with  $J_1$  to be unity, and focus on cylindrical boundary conditions.

(2) *Fermi-Hubbard model*. One of the most successful model that capture the essence of electronic and magnetic behaviour in quantum materials is the Fermi-Hubbard model. Despite the concise construction, it shows abundant feature such as the unconventional superfluidity/superconductivity, quantum magnetism, and interaction-driven insulating phase (or Mott insulator) [25–29]. With this in mind, we consider the following half-filled Hamiltonian:

$$H = -t \sum_{\langle p,q \rangle, \sigma} (c_{p,\sigma}^\dagger c_{q,\sigma} + \text{h.c.}) + U \sum_p c_{p,\uparrow}^\dagger c_{p,\uparrow} c_{p,\downarrow}^\dagger c_{p,\downarrow},$$

where  $t = 1$  is the hopping amplitude and  $U$  is the repulsive onsite potential for annihilation (creation) operators  $c_{p,\sigma}^{(\dagger)}$  defined for a fermion that resides on site  $p$  with spin  $\sigma$ . Here the summation on the hopping is taken over all pairs of nearest-neighboring sites  $\langle p, q \rangle$ . Note that one may further introduce nontrivial chemical potential to search for non-half-filled case, while we leave this as a future work.

## II. CLASSICAL AND QUANTUM ALGORITHMS

Our argument on quantum-classical crossover is based on the runtime analysis to compute ground state energy within desired total energy accuracy  $\epsilon$ . Underlying assumption is that, we want to provide a framework that elucidates the quantum-classical crosspoint for systems in which there is a constant or polynomially-shrinking spectral gap; we envision it is totally unclear whether there is any feasible crosspoint at all when the gap closes exponentially.

It is important to keep in mind that condensed matter physics often requires to extract physical properties beyond energy, such as magnetization, correlation function, or dynamical response. In this regard, it is natural to define runtime as required time to actually realize the quantum state. This is significant for the classical algorithm, namely the Density-Matrix Renormalization Group (DMRG) method, since it involves extrapolation to estimate error; it is not the total time to gather data to perform extrapolation within target accuracy, but it is the runtime to execute optimization until desired precision.

	Formal scaling (Lattice system)	2d $J_1$ - $J_2$ Heisenberg ( $J_2=0.5$ )				2d Fermi-Hubbard ( $U=4$ )			
	$N$ :#Total qubits	$6 \times 6$	$10 \times 10$	$20 \times 20$	$100 \times 100$	$6 \times 6$	$10 \times 10$	$20 \times 20$	$100 \times 100$
qDRIFT	$O(N^2/\epsilon^2)$	2.19e+13	1.99e+14	3.69e+15	2.86e+18	1.50e+13	1.29e+14	2.29e+15	1.73e+18
Random Trotter (2nd)	$O(N^2/\epsilon^{3/2})$	1.36e+10	1.12e+11	1.96e+12	1.46e+15	4.58e+11	3.78e+12	6.56e+13	4.86e+16
Taylorization	$O(N^2 K/\epsilon)$	5.25e+09	3.30e+10	4.36e+11	2.94e+14	4.30e+09	2.50e+10	3.11e+11	2.00e+14
Qubitization	$O(N^2/\epsilon)$	<b>7.08e+08</b>	<b>4.22e+08</b>	<b>5.76e+09</b>	<b>3.39e+12</b>	<b>5.65e+07</b>	<b>3.08e+08</b>	<b>3.92e+09</b>	<b>2.21e+12</b>

TABLE I.  $T$ -count required to perform the quantum phase estimation on lattice Hamiltonians based on various Hamiltonian simulation algorithms. Here, we denote the total qubit count by  $N$ , target energy accuracy by  $\epsilon (= 0.01)$ , and  $K = \log(N/\epsilon)/\log \log(N/\epsilon)$  as Taylorization order. Note that the post-Trotter methods, namely the Taylorization and qubitization algorithms, consume ancillary qubits of  $O(\log N)$  to block-encode the action of Hamiltonian simulation into truncated Hilbert space. This is comparable to those required by the quantum Fourier transformation that require ancillary qubits of  $O(\log(N/\epsilon))$ .

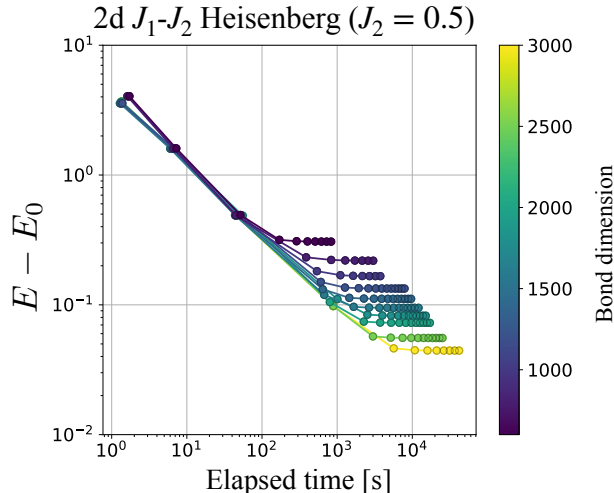


FIG. 2. Elapsed time scaling of DMRG algorithm in  $J_1$ - $J_2$  Heisenberg model at  $J_2 = 0.5$  with lattice size  $10 \times 10$ . Although the simulation itself does not reach  $\epsilon = 0.01$ , learning curves for different bond dimensions ranging from  $D = 600$  to  $D = 3000$  collapse into a single curve, which implies the adequacy to estimate runtime according to the obtained scaling law. All DMRG simulations are executed using ITensor library [30].

### A. Classical algorithm

Among the numerous powerful classical methods, here we choose the DMRG algorithm, which has been established as one of the most powerful and reliable numerical tools to study strongly-correlated quantum lattice models especially in one dimension (1d) [31, 32]. In short, the DMRG algorithm performs variational optimization on tensor-network-based ansatz named Matrix Product State (MPS) [33, 34]. Although MPS is designed to capture 1d area-law entangled quantum states efficiently [35], the powerfulness of DMRG algorithm allows one to explore quantum many-body physics beyond 1d including quasi-1d, 2d systems, and even all-

to-all connected models as considered in quantum chemistry [36, 37].

A remarkable characteristic of the DMRG algorithm is that it provides a means to perform systematic error analysis. This is deeply related with the construction of ansatz, or the MPS, which compresses the quantum state by performing site-by-site truncation of the full Hilbert space. The compression process explicitly yields a quantity called the “truncation error,” from which we can extrapolate the truncation-free energy  $E_0$  to estimate the ground truth. By tracking the deviation from the zero-truncation result  $E - E_0$ , we find that the computation time and error typically obeys scaling law (See Fig. 2 for an example of such a scaling behavior in 2d  $J_1$ - $J_2$  Heisenberg model). The resource estimate is done by combining the actual simulation results and the estimation from the scaling law. [See Appendix S2 for detailed analysis.]

### B. Quantum algorithm

Quantum phase estimation (QPE) is a quantum algorithm designed to extract the eigenphase  $\phi$  of a given unitary  $U$  by using ancilla qubits to indirectly read out the complex phase of the target system. More concretely, given a trial state  $|\psi\rangle$  whose fidelity with the  $k$ -th eigenstate  $|k\rangle$  of the unitary is given as  $f_k = \|\langle k|\psi\rangle\|^2$ , a single run of QPE projects the state to  $|k\rangle$  with probability  $f_k$ , and return a random variable  $\hat{\phi}$  which corresponds to a  $m$ -digit readout of  $\phi_k$ .

It was originally proposed by Ref. [38] that eigenenergies of a given Hamiltonian can be computed efficiently via QPE by taking advantage of quantum computers to perform Hamiltonian simulation, e.g.,  $U = \exp(-iH\tau)$ . Note that, even with fully fault-tolerant quantum computers, the simulation of ground state of general local Hamiltonian requires exponential cost (known to be in the complexity class of Quantum Merlin Arthur, or QMA) [39, 40]. Meanwhile, the Hamiltonian simulation itself falls into the class of BQP (which stands for Bounded-error Quantum Polynomial), meaning that it is a task that can be solved with polynomial cost with a

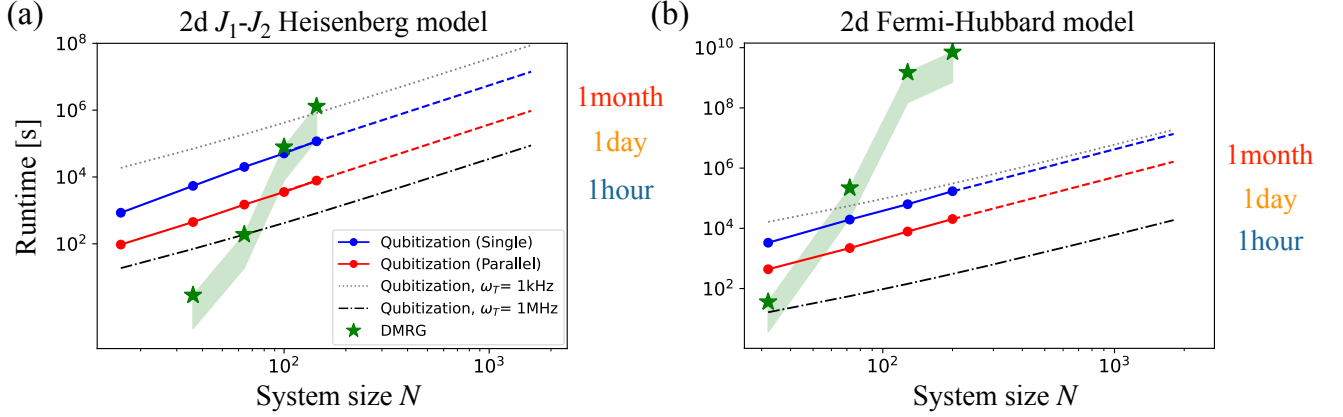


FIG. 3. Quantum-classical crossover in (a) 2d  $J_1$ - $J_2$  Heisenberg model of  $J_2/J_1 = 0.5$  and (b) 2d Fermi-Hubbard model of  $U/t = 4$ . The blue and red circles are the runtime estimate for the quantum phase estimation based on the qubitization technique, whose analysis involves quantum circuit compilation of all the steps (I), (II), and (III). All the gates are compiled under the Clifford+ $T$  formalism with each logical qubits encoded by the surface code with code distance  $d$  around 17 to 25 (See Appendix S8). Here, the number of magic factories  $n_F$  and number of parallelization threads  $n_{th}$  are taken as  $(n_F, n_{th}) = (16, 16)$  and  $(1, 1)$ , respectively. The dotted and dash-dotted chain lines are estimates that only involve the analysis of step (II); calculation is based solely on the  $T$ -count of the algorithm with realistic  $T$ -gate consumption rate of 1kHz and 1MHz, respectively. The green stars are data obtained from the actual simulation results of classical DMRG algorithm, with the shaded region denoting the potential room for improvement by using the most advanced computational resource (See Appendix S2). Note that the system size is related with the lattice size  $M \times M$  as  $N = 2M^2$  in the Fermi-Hubbard model.

fault-tolerant quantum computer [41]. The fact that the subroutine of the quantum phase estimation cannot be replaced efficiently by classical algorithm already implies that, potentially there are problems that can be solved efficiently on quantum computers. Accordingly numerous works have been devoted to analyze the error scaling under various Hamiltonian simulation techniques (especially the Trotter-based ones) [42–46]. We nevertheless point out that crucial questions remains unclear; which technique is the best practice to achieve the earliest quantum advantage for condensed matter problems, and at which point the crossover occurs.

Here we perform resource estimation under the following common assumptions: (1) logical qubits are encoded using the formalism of surface codes [47]; (2) quantum gate implementation is based on Clifford+ $T$  formalism; (3) circuit runtime is dominated by the Hamiltonian simulation (See Appendix S3 for discussion). We first address the first question cast above by compare among various Hamiltonian simulation algorithms the total number of  $T$ -gates, or  $T$ -count, because the application of  $T$ -gate involves time-consuming procedure called the magic-state distillation. Although not necessarily, this procedure is considered to dominate the runtime in many realistic setups. Therefore, we argue that  $T$ -count shall provide sufficient information to determine the best practice. Then, we further perform high-resolution analysis on the runtime, by considering concrete quantum circuit compilation with specific physical/logical qubit configuration that is compatible with the surface code.

Let us first compute the  $T$ -counts to compare the state-of-the-art Hamiltonian simulation techniques: (random-

ized) Trotter product formula [44, 48], qDRIFT [46], Taylorization [49–51], and qubitization [52]. The former two commonly relies on the Trotter decomposition to approximate the unitary time evolution with sequential application of (controlled) Pauli rotations, while the latter two, dubbed to be included in “post-Trotter methods,” are rather based on the technique called the *block-encoding*, which make use of ancillary qubits to encode desired (non-unitary) operations on target systems. While post-Trotter methods are known to be exponentially more efficient in terms of gate complexity regarding the simulation accuracy [49], it is nontrivial to ask which is the best practice in the crossover regime, where the prefactor plays a significant role.

As we show the details in Appendix S3, we have compiled quantum circuits based on existing error analysis to reveal the required  $T$ -counts. From results presented in Table I, we find that the qubitization algorithm provides the most efficient implementation in order to reach the target energy accuracy  $\epsilon = 0.01$ . Although the post-Trotter methods, i.e., the Taylorization and qubitization algorithms require additional ancillary qubits of  $O(\log N)$  to perform the block encoding, we regard this overhead is not a serious roadblock, since the target system itself and the quantum Fourier transformation requires qubits of  $O(N)$  and  $O(\log(N/\epsilon))$ , respectively.

The above result motivates us to study the quantum-classical crossover entirely using the qubitization technique as the subroutine for the QPE. As is detailed in Appendix S7, our runtime analysis involves the following steps:

(I) *Hardware configuration.* Determine the architec-



ture of quantum computers (e.g., number of magic state factory, qubit connectivity etc.).

- (II) *Circuit synthesis and transpilation.* Translate high-level description of quantum circuits to Clifford+ $T$  formalism with the provided optimization level.
- (III) *Compilation to executable instructions.* Decompose logical gates into the sequence of executable instruction sets based on lattice surgery.

It should be noted that the ordinary runtime estimation only involves the step (II); simply multiplying the execution time of  $T$ -gate to  $T$ -count as  $N_T t_T$ . However, we emphasize that this estimation method loses several vital factors in time analysis which may eventually lead to deviation of a one or two orders of magnitudes. In sharp contrast, our runtime analysis comprehensively takes all steps into account to yield reliable estimation under realistic quantum computing platforms.

### III. RESOURCE ESTIMATES AND CROSSOVERS

Now we are ready to present our main results. Figure 3 shows the runtime in classical/quantum algorithms to simulate the ground state energy in 2d  $J_1$ - $J_2$  Heisenberg model and 2d Fermi-Hubbard model. In both figures, we observe clear evidence of quantum-classical crossovers below a hundred-qubit system (at lattice size of  $10 \times 10$  and  $6 \times 6$ , respectively) within plausible runtime. Furthermore, a significant difference from ab initio quantum chemistry calculations are highlighted in the feasibility of system size  $N \sim 1000$  logical qubit simulations, especially in simulation of 2d Heisenberg model that relies on parallelization of the oracles (See Appendix S7 for details).

For concreteness, let us focus on the simulation of systems with lattice size of  $10 \times 10$ , at which we find the quantum algorithm to outperform the classical one. Using the error scaling, we find that the DMRG simulation is estimated to take about  $10^5$  and  $10^9$  seconds in 2d Heisenberg and 2d Fermi-Hubbard models, respectively. On the other hand, the estimation based on the dedicated quantum circuit compilation with the most pessimistic equipment (denoted as “Single” in Fig. 3) achieves runtime below  $10^5$  seconds in both models, which is improved by an order by assuming more abundant quantum resource. Concretely, using a quantum computer with a multiple magic state factory ( $n_F=16$ ) that performs multi-thread execution of the Hamiltonian simulation ( $n_{Th} = 16$ ), quantum advantage shall be accomplished in the realm of computational time of hours. We find that it is also informative to display the ordinary  $T$ -count-based estimation to assess their soundness; it is indeed reasonable to assume the clock rate of 1-10kHz for a single-thread execution, while its precise value fluctuates depending on the problem instance.

We mention that the classical algorithm (DMRG) experiences exponential increase in the runtime to reach desired total energy accuracy  $\epsilon = 0.01$ . This outcome is somewhat expected, since one must enforce the MPS to represent 2d quantum correlation into 1d via cylindrical boundary condition [53, 54]. One may argue that we shall alternatively employ two-dimensional tensor network states such as the Projected Entangled-Pair State (PEPS) or Tensor Product State (TPS) [55, 56]. Asymptotic scaling for large sizes are indeed better in higher-dimension tensor networks while for small systems the larger prefactor negates the advantage of using them. We point out that the cusp occurs in relatively small system size such that the DMRG algorithm is a well-suited methodology to represent the runtime of classical algorithms.

### IV. DISCUSSION

Our work has conveyed detailed analysis on the quantum-classical crossover in condensed matter physics, namely, the point where the early application of fault-tolerant quantum computers show benefit over classical algorithms. Unlike past work, which mainly considers exact simulation techniques to represent classical methods, we have proposed to utilize the error scaling to estimate runtime in one of the most powerful variational simulation method, or the DMRG algorithm. Execution times of quantum algorithms are also investigated in depth by conducting high-resolution analysis that considers topological restrictions on physical qubit connectivity, parallelization of Hamiltonian simulation oracles, etc. This has led us to conclude that the crossover is expected to occur at the system size of a hundred within feasible runtime of hours. Our work provides a reliable guiding principle to establish milestones for various platform of quantum technologies.

Various future directions can be envisioned. Here, we mention main three of them. The first is the runtime analysis on broader class of classical methods. While in this work we have exclusively focused on the DMRG algorithms for their simplicity in runtime analysis, other quantum many-body computation methods such as quantum Monte Carlo (e.g. path-integral Monte Carlo, variational Monte Carlo etc.), coupled-cluster techniques, or other tensor-network-based methods are equally significant. Establishing a systematic way to perform estimates on Monte Carlo methods shall be non-trivial in particular. Secondly, it is important to further develop quantum simulation algorithms that are designed to extract physics beyond the eigenenergy, such as the spacial/temporal correlation function, nonequilibrium phenomena, finite temperature properties, and so on. It shall be fruitful to subsequently perform error analysis on such objective. Thirdly, it is intriguing to consider classical-quantum hybrid approach. This may involve twirling of Solovay-Kitaev errors into stochastic

errors that can be eliminated by quantum error mitigation techniques originally developed for near-future quantum computers without error correction [57, 58].

*Acknowledgements.*— N.Y. wishes to thank JST PRESTO No. JPMJPR2119 and the support from IBM Quantum. T.O. wishes to thank JST PRESTO Grant Number JPMJPR1912, JSPS KAKENHI Nos. 22K18682 and 22H01179, and support by the Endowed Project for Quantum Software Research and Education, The Uni-

versity of Tokyo (<https://qsw.phys.s.u-tokyo.ac.jp/>). Y. S. wishes to thank JST PRESTO Grant Number JPMJPR1916 and JST Moonshot R&D Grant Number JPMJMS2061. W.M. wishes to thank JST PRESTO No. JPMJPR191A, JST COI-NEXT program Grant No. JPMJPF2014 and MEXT Quantum Leap Flagship Program (MEXT Q-LEAP) Grant Number JPMXS0118067394 and JPMXS0120319794. A part of computations were performed using the Institute of Solid State Physics at the University of Tokyo.

\* [nyoshioka@ap.t.u-tokyo.ac.jp](mailto:nyoshioka@ap.t.u-tokyo.ac.jp)

† [t-okubo@phys.s.u-tokyo.ac.jp](mailto:t-okubo@phys.s.u-tokyo.ac.jp)

‡ [yasunari.suzuki.gz@hco.ntt.co.jp](mailto:yasunari.suzuki.gz@hco.ntt.co.jp)

§ [mizukami.wataru.qiqb@osaka-u.ac.jp](mailto:mizukami.wataru.qiqb@osaka-u.ac.jp)

- [1] Frank Arute, Kunal Arya, Ryan Babbush, Dave Bacon, Joseph C Bardin, Rami Barends, Rupak Biswas, Sergio Boixo, Fernando GSL Brandao, David A Buell, Brian Burkett, Yu Chen, Zijun Chen, Ben Chiaro, Roberto Collins, William Courtney, Andrew Dunsworth, Edward Farhi, Brooks Foxen, Austin Fowler, Craig Gidney, Marissa Giustina, Rob Graff, Keith Guerin, Steve Habegger, Matthew P. Harrigan, Michael J. Hartmann, Alan Ho, Markus Hoffmann, Trent Huang, Travis S. Humble, Sergey V. Isakov, Evan Jeffrey, Zhang Jiang, Dvir Kafri, Kostyantyn Kechedzhi, Julian Kelly, Paul V. Klimov, Sergey Knysh, Alexander Korotkov, Fedor Kostritsa, David Landhuis, Mike Lindmark, Erik Lucero, Dmitry Lyakh, Salvatore Mandrà, Jarrod R. McClean, Matthew McEwen, Anthony Megrant, Xiao Mi, Kristel Michielsen, Masoud Mohseni, Josh Mutus, Ofer Naaman, Matthew Neeley, Charles Neill, Murphy Yuezhen Niu, Eric Ostby, Andre Petukhov, John C. Platt, Chris Quintana, Eleanor G. Rieffel, Pedram Roushan, Nicholas C. Rubin, Daniel Sank, Kevin J. Satzinger, Vadim Smelyanskiy, Kevin J. Sung, Matthew D. Trevithick, Amit Vainsencher, Benjamin Villalonga, Theodore White, Z. Jamie Yao, Ping Yeh, Adam Zalcman, Hartmut Neven, and John M. Martinis, “Quantum supremacy using a programmable superconducting processor,” *Nature* **574**, 505–510 (2019).
- [2] Han-Sen Zhong, Hui Wang, Yu-Hao Deng, Ming-Cheng Chen, Li-Chao Peng, Yi-Han Luo, Jian Qin, Dian Wu, Xing Ding, Yi Hu, Peng Hu, Xiao-Yan Yang, Wei-Jun Zhang, Hao Li, Yuxuan Li, Xiao Jiang, Lin Gan, Guangwen Yang, Lixing You, Zhen Wang, Li Li, Nai-Le Liu, Chao-Yang Lu, and Jian-Wei Pan, “Quantum computational advantage using photons,” *Science* **370**, 1460–1463 (2020), <https://www.science.org/doi/pdf/10.1126/science.abe8770>.
- [3] Han-Sen Zhong, Yu-Hao Deng, Jian Qin, Hui Wang, Ming-Cheng Chen, Li-Chao Peng, Yi-Han Luo, Dian Wu, Si-Qiu Gong, Hao Su, Yi Hu, Peng Hu, Xiao-Yan Yang, Wei-Jun Zhang, Hao Li, Yuxuan Li, Xiao Jiang, Lin Gan, Guangwen Yang, Lixing You, Zhen Wang, Li Li, Nai-Le Liu, Jelmer J. Renema, Chao-Yang Lu, and Jian-Wei Pan, “Phase-programmable gaussian boson sampling using stimulated squeezed light,” *Phys. Rev. Lett.* **127**, 180502 (2021).
- [4] Yulin Wu, Wan-Su Bao, Sirui Cao, Fusheng Chen, Ming-Cheng Chen, Xiawei Chen, Tung-Hsun Chung, Hui Deng, Yajie Du, Daojin Fan, Ming Gong, Cheng Guo, Chu Guo, Shaojun Guo, Lianchen Han, Linyin Hong, He-Liang Huang, Yong-Heng Huo, Liping Li, Na Li, Shaowei Li, Yuan Li, Futian Liang, Chun Lin, Jin Lin, Hao-ran Qian, Dan Qiao, Hao Rong, Hong Su, Lihua Sun, Liangyuan Wang, Shiyu Wang, Dachao Wu, Yu Xu, Kai Yan, Weifeng Yang, Yang Yang, Yangsen Ye, Jianghan Yin, Chong Ying, Jiale Yu, Chen Zha, Cha Zhang, Haibin Zhang, Kaili Zhang, Yiming Zhang, Han Zhao, Youwei Zhao, Liang Zhou, Qingling Zhu, Chao-Yang Lu, Cheng-Zhi Peng, Xiaobo Zhu, and Jian-Wei Pan, “Strong quantum computational advantage using a superconducting quantum processor,” *Phys. Rev. Lett.* **127**, 180501 (2021).
- [5] Lars S Madsen, Fabian Laudenbach, Mohsen Falamarzi Askarani, Fabien Rortais, Trevor Vincent, Jacob FF Bulmer, Filippo M Miatto, Leonhard Neuhaus, Lukas G Helt, Matthew J Collins, *et al.*, “Quantum computational advantage with a programmable photonic processor,” *Nature* **606**, 75–81 (2022).
- [6] Peter W Shor, “Polynomial-time algorithms for prime factorization and discrete logarithms on a quantum computer,” *SIAM review* **41**, 303–332 (1999).
- [7] Austin G. Fowler, Matteo Mariantoni, John M. Martinis, and Andrew N. Cleland, “Surface codes: Towards practical large-scale quantum computation,” *Phys. Rev. A* **86**, 032324 (2012).
- [8] N. Cody Jones, Rodney Van Meter, Austin G. Fowler, Peter L. McMahon, Jungsang Kim, Thaddeus D. Ladd, and Yoshihisa Yamamoto, “Layered architecture for quantum computing,” *Phys. Rev. X* **2**, 031007 (2012).
- [9] Vlad Gheorghiu and Michele Mosca, “Benchmarking the quantum cryptanalysis of symmetric, public-key and hash-based cryptographic schemes,” (2019), [1902.02332](https://arxiv.org/abs/1902.02332).
- [10] Craig Gidney and Martin Ekerå, “How to factor 2048 bit RSA integers in 8 hours using 20 million noisy qubits,” *Quantum* **5**, 433 (2021).
- [11] R. L. Rivest, A. Shamir, and L. Adleman, “A method for obtaining digital signatures and public-key cryptosystems,” *Commun. ACM* **21**, 120–126 (1978).
- [12] Cameron F Kerry and Patrick D Gallagher, “Digital signature standard (dss),” FIPS PUB , 186–4 (2013).
- [13] W. Diffie and M. Hellman, “New directions in cryptography,” *IEEE Transactions on Information Theory* **22**, 644–654 (1976).
- [14] C David Sherrill, David E Manolopoulos, Todd J Martínez, and Angelos Michaelides, “Electronic structure software,” *The Journal of Chemical Physics* **153**,

- 070401 (2020).
- [15] Markus Reiher, Nathan Wiebe, Krysta M. Svore, Dave Wecker, and Matthias Troyer, “Elucidating reaction mechanisms on quantum computers,” *Proceedings of the National Academy of Sciences* (2017), 10.1073/pnas.1619152114.
  - [16] Dominic W Berry, Craig Gidney, Mario Motta, Jarrod R McClean, and Ryan Babbush, “Qubitization of arbitrary basis quantum chemistry leveraging sparsity and low rank factorization,” *Quantum* **3**, 208 (2019).
  - [17] Vera von Burg, Guang Hao Low, Thomas Häner, Damian S. Steiger, Markus Reiher, Martin Roetteler, and Matthias Troyer, “Quantum computing enhanced computational catalysis,” *Phys. Rev. Research* **3**, 033055 (2021).
  - [18] Joonho Lee, Dominic W. Berry, Craig Gidney, William J. Huggins, Jarrod R. McClean, Nathan Wiebe, and Ryan Babbush, “Even more efficient quantum computations of chemistry through tensor hypercontraction,” *PRX Quantum* **2**, 030305 (2021).
  - [19] Joshua J. Goings, Alec White, Joonho Lee, Christofer S. Tautermann, Matthias Degroote, Craig Gidney, Toru Shiozaki, Ryan Babbush, and Nicholas C. Rubin, “Reliably assessing the electronic structure of cytochrome p450 on today’s classical computers and tomorrow’s quantum computers,” *Proceedings of the National Academy of Sciences* **119**, e2203533119 (2022), <https://www.pnas.org/doi/pdf/10.1073/pnas.2203533119>.
  - [20] Guang-Ming Zhang, Hui Hu, and Lu Yu, “Valence-bond spin-liquid state in two-dimensional frustrated spin-1/2 heisenberg antiferromagnets,” *Phys. Rev. Lett.* **91**, 067201 (2003).
  - [21] Hong-Chen Jiang, Hong Yao, and Leon Balents, “Spin liquid ground state of the spin- $\frac{1}{2}$  square  $J_1$ - $J_2$  heisenberg model,” *Phys. Rev. B* **86**, 024424 (2012).
  - [22] Wen-Jun Hu, Federico Becca, Alberto Parola, and Sandro Sorella, “Direct evidence for a gapless  $Z_2$  spin liquid by frustrating néel antiferromagnetism,” *Phys. Rev. B* **88**, 060402 (2013).
  - [23] Ling Wang and Anders W. Sandvik, “Critical level crossings and gapless spin liquid in the square-lattice spin-1/2  $J_1 - J_2$  heisenberg antiferromagnet,” *Phys. Rev. Lett.* **121**, 107202 (2018).
  - [24] Yusuke Nomura and Masatoshi Imada, “Dirac-type nodal spin liquid revealed by refined quantum many-body solver using neural-network wave function, correlation ratio, and level spectroscopy,” *Phys. Rev. X* **11**, 031034 (2021).
  - [25] John Hubbard, “Electron correlations in narrow energy bands,” *Proceedings of the Royal Society of London. Series A. Mathematical and Physical Sciences* **276**, 238–257 (1963).
  - [26] John Hubbard, “Electron correlations in narrow energy bands. ii. the degenerate band case,” *Proceedings of the Royal Society of London. Series A. Mathematical and Physical Sciences* **277**, 237–259 (1964).
  - [27] Tilman Esslinger, “Fermi-hubbard physics with atoms in an optical lattice,” *Annual Review of Condensed Matter Physics* **1**, 129–152 (2010), <https://doi.org/10.1146/annurev-conmatphys-070909-104059>.
  - [28] Daniel P. Arovas, Erez Berg, Steven A. Kivelson, and Srinivas Raghu, “The hubbard model,” *Annual Review of Condensed Matter Physics* **13**, 239–274 (2022), <https://doi.org/10.1146/annurev-conmatphys-031620-102024>.
  - [29] Mingpu Qin, Thomas Schäfer, Sabine Andergassen, Philippe Corboz, and Emanuel Gull, “The hubbard model: A computational perspective,” *Annual Review of Condensed Matter Physics* **13**, 275–302 (2022), <https://doi.org/10.1146/annurev-conmatphys-090921-033948>.
  - [30] Matthew Fishman, Steven R. White, and E. Miles Stoudenmire, “The ITensor Software Library for Tensor Network Calculations,” *SciPost Phys. Codebases*, 4 (2022).
  - [31] Steven R. White, “Density matrix formulation for quantum renormalization groups,” *Phys. Rev. Lett.* **69**, 2863–2866 (1992).
  - [32] Steven R. White and David A. Huse, “Numerical renormalization-group study of low-lying eigenstates of the antiferromagnetic  $s=1$  heisenberg chain,” *Phys. Rev. B* **48**, 3844–3852 (1993).
  - [33] Stellan Östlund and Stefan Rommer, “Thermodynamic limit of density matrix renormalization,” *Phys. Rev. Lett.* **75**, 3537–3540 (1995).
  - [34] J Dukelsky, M. A Martín-Delgado, T Nishino, and G Sierra, “Equivalence of the variational matrix product method and the density matrix renormalization group applied to spin chains,” *Europhysics Letters (EPL)* **43**, 457–462 (1998).
  - [35] J. Eisert, M. Cramer, and M. B. Plenio, “Colloquium: Area laws for the entanglement entropy,” *Rev. Mod. Phys.* **82**, 277–306 (2010).
  - [36] Sebastian Wouters and Dimitri Van Neck, “The density matrix renormalization group for ab initio quantum chemistry,” *The European Physical Journal D* **68**, 272 (2014).
  - [37] Alberto Baiardi and Markus Reiher, “The density matrix renormalization group in chemistry and molecular physics: Recent developments and new challenges,” *The Journal of Chemical Physics* **152**, 040903 (2020), <https://doi.org/10.1063/1.5129672>.
  - [38] Daniel S. Abrams and Seth Lloyd, “Quantum algorithm providing exponential speed increase for finding eigenvalues and eigenvectors,” *Phys. Rev. Lett.* **83**, 5162–5165 (1999).
  - [39] Alexei Yu Kitaev, Alexander Shen, Mikhail N Vyalyi, and Mikhail N Vyalyi, *Classical and quantum computation*, 47 (American Mathematical Soc., 2002).
  - [40] Julia Kempe, Alexei Kitaev, and Oded Regev, “The complexity of the local hamiltonian problem,” *Siam journal on computing* **35**, 1070–1097 (2006).
  - [41] Seth Lloyd, “Universal quantum simulators,” *Science* **273**, 1073–1078 (1996), <https://www.science.org/doi/pdf/10.1126/science.273.5278.1073>.
  - [42] Masuo Suzuki, “General correction theorems on decomposition formulae of exponential operators and extrapolation methods for quantum monte carlo simulations,” *Phys. Lett. A* **113**, 299–300 (1985).
  - [43] J Huyghebaert and H De Raedt, “Product formula methods for time-dependent schrodinger problems,” *Journal of Physics A: Mathematical and General* **23**, 5777–5793 (1990).
  - [44] Andrew M. Childs, Aaron Ostrander, and Yuan Su, “Faster quantum simulation by randomization,” *Quantum* **3**, 182 (2019).

- [45] Andrew M. Childs, Yuan Su, Minh C. Tran, Nathan Wiebe, and Shuchen Zhu, “Theory of trotter error with commutator scaling,” *Phys. Rev. X* **11**, 011020 (2021).
- [46] Earl Campbell, “Random compiler for fast hamiltonian simulation,” *Phys. Rev. Lett.* **123**, 070503 (2019).
- [47] A Yu Kitaev, “Quantum computations: algorithms and error correction,” *Russ. Math. Surv.* **52**, 1191–1249 (1997).
- [48] Masuo Suzuki, “General theory of fractal path integrals with applications to many-body theories and statistical physics,” *Journal of Mathematical Physics* **32**, 400–407 (1991), <https://doi.org/10.1063/1.529425>.
- [49] Dominic W. Berry, Andrew M. Childs, Richard Cleve, Robin Kothari, and Rolando D. Somma, “Exponential improvement in precision for simulating sparse hamiltonians,” in *Proceedings of the Forty-Sixth Annual ACM Symposium on Theory of Computing*, STOC ’14 (Association for Computing Machinery, New York, NY, USA, 2014) p. 283–292.
- [50] Dominic W. Berry, Andrew M. Childs, Richard Cleve, Robin Kothari, and Rolando D. Somma, “Simulating hamiltonian dynamics with a truncated taylor series,” *Phys. Rev. Lett.* **114**, 090502 (2015).
- [51] Richard Meister, Simon C. Benjamin, and Earl T. Campbell, “Tailoring Term Truncations for Electronic Structure Calculations Using a Linear Combination of Unitaries,” *Quantum* **6**, 637 (2022).
- [52] Guang Hao Low and Isaac L Chuang, “Hamiltonian simulation by qubitization,” *Quantum* **3**, 163 (2019).
- [53] J. P. F. LeBlanc, Andrey E. Antipov, Federico Becca, Ireneusz W. Bulik, Garnet Kin-Lic Chan, Chia-Min Chung, Youjin Deng, Michel Ferrero, Thomas M. Henderson, Carlos A. Jiménez-Hoyos, E. Kozik, Xuan-Wen Liu, Andrew J. Millis, N. V. Prokof’ev, Mingpu Qin, Gustavo E. Scuseria, Hao Shi, B. V. Svistunov, Luca F. Tocchio, I. S. Tupitsyn, Steven R. White, Shiwei Zhang, Bo-Xiao Zheng, Zhenyue Zhu, and Emanuel Gull (Simons Collaboration on the Many-Electron Problem), “Solutions of the two-dimensional hubbard model: Benchmarks and results from a wide range of numerical algorithms,” *Phys. Rev. X* **5**, 041041 (2015).
- [54] Ling Wang and Anders W. Sandvik, “Critical level crossings and gapless spin liquid in the square-lattice spin-1/2  $J_1 - J_2$  heisenberg antiferromagnet,” *Phys. Rev. Lett.* **121**, 107202 (2018).
- [55] Tomotoshi Nishino, Yasuhiro Hieida, Kouichi Okunishi, Nobuya Maeshima, Yasuhiro Akutsu, and Andrej Gendiar, “Two-Dimensional Tensor Product Variational Formulation,” *Progress of Theoretical Physics* **105**, 409–417 (2001), <https://academic.oup.com/ptp/article-pdf/105/3/409/5191613/105-3-409.pdf>.
- [56] F. Verstraete and J. I. Cirac, “Renormalization algorithms for quantum-many body systems in two and higher dimensions,” (2004).
- [57] Yasunari Suzuki, Suguru Endo, Keisuke Fujii, and Yuuki Tokunaga, “Quantum error mitigation for fault-tolerant quantum computing,” *arXiv preprint arXiv:2010.03887* (2020).
- [58] Christophe Piveteau, David Sutter, Sergey Bravyi, Jay M. Gambetta, and Kristan Temme, “Error mitigation for universal gates on encoded qubits,” *Phys. Rev. Lett.* **127**, 200505 (2021).
- [59] F. D. M. Haldane, “Nonlinear field theory of large-spin heisenberg antiferromagnets: Semiclassically quantized solitons of the one-dimensional easy-axis néel state,” *Phys. Rev. Lett.* **50**, 1153–1156 (1983).
- [60] F.D.M. Haldane, “Continuum dynamics of the 1-d heisenberg antiferromagnet: Identification with the o(3) nonlinear sigma model,” *Physics Letters A* **93**, 464–468 (1983).
- [61] M B Hastings, “An area law for one-dimensional quantum systems,” *Journal of Statistical Mechanics: Theory and Experiment* **2007**, P08024–P08024 (2007).
- [62] Ulrich Schollwöck, “The density-matrix renormalization group in the age of matrix product states,” *Annals of Physics* **326**, 96–192 (2011), january 2011 Special Issue.
- [63] U. Schollwöck, “The density-matrix renormalization group,” *Rev. Mod. Phys.* **77**, 259–315 (2005).
- [64] Örs Legeza and Gábor Fáth, “Accuracy of the density-matrix renormalization-group method,” *Phys. Rev. B* **53**, 14349–14358 (1996).
- [65] E. M. Stoudenmire and Steven R. White, “Real-space parallel density matrix renormalization group,” *Phys. Rev. B* **87**, 155137 (2013).
- [66] Hiroshi Ueda and Koichi Kusakabe, “Determination of boundary scattering, magnon-magnon scattering, and the haldane gap in heisenberg spin chains,” *Phys. Rev. B* **84**, 054446 (2011).
- [67] F. D. M. Haldane, “Nonlinear field theory of large-spin heisenberg antiferromagnets: Semiclassically quantized solitons of the one-dimensional easy-axis néel state,” *Phys. Rev. Lett.* **50**, 1153–1156 (1983).
- [68] A Yu Kitaev, “Quantum measurements and the abelian stabilizer problem,” *arXiv preprint quant-ph/9511026* (1995).
- [69] William Kirby, Mario Motta, and Antonio Mezzacapo, “Exact and efficient lanczos method on a quantum computer,” *arXiv preprint arXiv:2208.00567* (2022).
- [70] Earl Campbell, “Shorter gate sequences for quantum computing by mixing unitaries,” *Phys. Rev. A* **95**, 042306 (2017).
- [71] Matthew B. Hastings, “Turning gate synthesis errors into incoherent errors,” *Quantum Info. Comput.* **17**, 488–494 (2017).
- [72] Ryan Babbush, Dominic W Berry, Ian D Kivlichan, Annie Y Wei, Peter J Love, and Alán Aspuru-Guzik, “Exponentially more precise quantum simulation of fermions in second quantization,” *New Journal of Physics* **18**, 033032 (2016).
- [73] Dominic W. Berry, Mária Kieferová, Artur Scherer, Yuval R. Sanders, Guang Hao Low, Nathan Wiebe, Craig Gidney, and Ryan Babbush, “Improved techniques for preparing eigenstates of fermionic hamiltonians,” *npj Quantum Information* **4**, 22 (2018).
- [74] David Poulin, Alexei Kitaev, Damian S. Steiger, Matthew B. Hastings, and Matthias Troyer, “Quantum algorithm for spectral measurement with a lower gate count,” *Phys. Rev. Lett.* **121**, 010501 (2018).
- [75] Ryan Babbush, Craig Gidney, Dominic W. Berry, Nathan Wiebe, Jarrod McClean, Alexandru Paler, Austin Fowler, and Hartmut Neven, “Encoding electronic spectra in quantum circuits with linear t complexity,” *Phys. Rev. X* **8**, 041015 (2018).
- [76] John M. Martyn, Zane M. Rossi, Andrew K. Tan, and Isaac L. Chuang, “Grand unification of quantum algorithms,” *PRX Quantum* **2**, 040203 (2021).
- [77] Wojciech Górecki, Rafał Demkowicz-Dobrzański,



- Howard M. Wiseman, and Dominic W. Berry, “ $\pi$ -corrected heisenberg limit,” *Phys. Rev. Lett.* **124**, 030501 (2020).
- [78] Pablo A. M. Casares, Roberto Campos, and M. A. Martin-Delgado, “TFermion: A non-Clifford gate cost assessment library of quantum phase estimation algorithms for quantum chemistry,” *Quantum* **6**, 768 (2022).
- [79] Craig Gidney, “Halving the cost of quantum addition,” *Quantum* **2**, 74 (2018).
- [80] Peter Selinger, “Efficient clifford+t approximation of single-qubit operators,” *Quantum Info. Comput.* **15**, 159–180 (2015).
- [81] V.V. Shende, S.S. Bullock, and I.L. Markov, “Synthesis of quantum-logic circuits,” *IEEE Transactions on Computer-Aided Design of Integrated Circuits and Systems* **25**, 1000–1010 (2006).
- [82] Eric Dennis, Alexei Kitaev, Andrew Landahl, and John Preskill, “Topological quantum memory,” *Int. J. Theor. Phys.* **43**, 4452–4505 (2002).
- [83] Sergey B Bravyi and A Yu Kitaev, “Quantum codes on a lattice with boundary,” arXiv preprint quant-ph/9811052 (1998).
- [84] Austin G Fowler and Craig Gidney, “Low overhead quantum computation using lattice surgery,” arXiv preprint arXiv:1808.06709 (2018).
- [85] Austin G. Fowler, Matteo Mariantoni, John M. Martinis, and Andrew N. Cleland, “Surface codes: Towards practical large-scale quantum computation,” *Physical Review A* **86**, 032324 (2012).
- [86] Clare Horsman, Austin G Fowler, Simon Devitt, and Rodney Van Meter, “Surface code quantum computing by lattice surgery,” *New Journal of Physics* **14**, 123011 (2012).
- [87] Daniel Litinski, “A game of surface codes: Large-scale quantum computing with lattice surgery,” *Quantum* **3**, 128 (2019).
- [88] Christopher Chamberland and Earl T. Campbell, “Universal quantum computing with twist-free and temporally encoded lattice surgery,” *PRX Quantum* **3** (2022), 10.1103/prxquantum.3.010331.
- [89] Michael Beverland, Vadym Kliuchnikov, and Eddie Schoute, “Surface code compilation via edge-disjoint paths,” *PRX Quantum* **3**, 020342 (2022).
- [90] Leon Riesebos, Xiang Fu, Savvas Varsamopoulos, Carmen G Almudever, and Koen Bertels, “Pauli frames for quantum computer architectures,” in *Proceedings of the 54th Annual Design Automation Conference 2017* (2017) pp. 1–6.
- [91] Austin G Fowler, “Time-optimal quantum computation,” arXiv preprint arXiv:1210.4626 (2012).
- [92] Adam Holmes, Mohammad Reza Jokar, Ghasem Pasandi, Yongshan Ding, Massoud Pedram, and Frederic T Chong, “NISQ+: Boosting quantum computing power by approximating quantum error correction,” in *2020 ACM/IEEE 47th Annual International Symposium on Computer Architecture (ISCA)* (IEEE, 2020) pp. 556–569.
- [93] Yosuke Ueno, Masaaki Kondo, Masamitsu Tanaka, Yasunari Suzuki, and Yutaka Tabuchi, “QULATIS: A quantum error correction methodology toward lattice surgery,” in *2022 IEEE International Symposium on High-Performance Computer Architecture (HPCA)* (IEEE, 2022).
- [94] Guang Hao Low, Vadym Kliuchnikov, and Luke Schaeffer, “Trading t-gates for dirty qubits in state preparation and unitary synthesis,” arXiv preprint arXiv:1812.00954 (2018).

# Supplementary Materials for: Hunting for quantum-classical crossover in condensed matter problems

## CONTENTS

Introduction	1
I. Target models	2
II. Classical and quantum algorithms	2
A. Classical algorithm	3
B. Quantum algorithm	3
III. Resource estimates and Crossovers	5
IV. Discussion	5
References	6
S1. Definition of Target models	11
A. Spin-1/2 2d $J_1$ - $J_2$ Heisenberg model	11
B. 2d Fermi-Hubbard model	11
C. Spin-1 Heisenberg chain	12
S2. Classical simulation of ground state using density-matrix renormalization group	12
A. Overview of DMRG algorithm	12
B. Error analysis and computation time estimate for two-dimensional models	12
C. Error analysis and computation time estimate for one-dimensional $S = 1$ Heisenberg model	16
S3. Quantum algorithms for estimating energy spectra	16
A. Overview on quantum phase estimation	16
B. General cost estimation strategy for phase estimation	18
C. Trotter-based Hamiltonian Simulation methods for phase estimation	19
1. $T$ -count in Trotter-based methods	20
D. Post-Trotter Hamiltonian simulation methods for quantum phase estimation	21
1. Block encoding for linear combination of unitaries	21
2. Qubitization	22
3. Taylorization	24
S4. Post-Trotter oracles for lattice models	25
A. Abstract structure of <b>PREPARE</b>	25
B. Abstract structure of <b>SELECT</b>	27
C. Explicit construction of oracles	28
1. 2d J1J2 Heisenberg model	28
2. 2d Fermi-Hubbard model	30
3. Spin-1 antiferromagnetic Heisenberg chain	32
S5. Complexity of basic quantum operations	33
S6. Szegedy quantum walk with imperfect <b>PREPARE</b>	33
S7. Runtime analysis of qubitization-based quantum phase estimation	35
A. Overview	35
B. Surface code and lattice surgery	35
C. Time estimation without topological restriction	36
D. Placement of logical qubits and routing for lattice surgery	37
E. Parameter estimation and numerical evaluation	38

S8. Estimation of the number of physical qubits, code distances, and actual runtime	40
A. Quantum resource under various algorithmic/hardware requirements	41

## S1. DEFINITION OF TARGET MODELS

In this paper, we discuss the quantum-classical crossover in condensed matter problems where the Hamiltonian is defined on  $d$ -dimensional translationally symmetric lattice with at most  $G$ -local terms:

$$H = \sum_{\mathbf{p}} \sum_{\{\boldsymbol{\mu}, \alpha\}} w_{\boldsymbol{\mu}, \alpha} \hat{\Lambda}_{\mathbf{p}}^{(\alpha_1)} \hat{\Lambda}_{\mathbf{p}+\boldsymbol{\mu}_1}^{(\alpha_2)} \cdots \hat{\Lambda}_{\mathbf{p}+\boldsymbol{\mu}_{G-1}}^{(\alpha_G)}, \quad (\text{S1})$$

where  $\mathbf{p} = (p_1, \dots, p_d)$  labels the lattice site (including the sublattice structure),  $\boldsymbol{\mu} = (\boldsymbol{\mu}_1, \dots, \boldsymbol{\mu}_{G-1})$  is a set of vectors that identifies the connection between interacting sites,  $\alpha$  discriminates the interaction on the sites,  $\hat{\Lambda}_{\mathbf{p}}^{(\alpha)}$  is an operator for microscopic degrees of freedom (e.g. spin, fermion, boson) on site  $\mathbf{p}$ , and  $w_{\boldsymbol{\mu}, \alpha}$  is the amplitude of the interaction. In particular, we employ three representative models with long-standing problems; 2d  $J_1$ - $J_2$  Heisenberg model, 2d Fermi-Hubbard model, and spin-1 Heisenberg chain. In the following, we provide the definition of the target models accompanied with brief descriptions.

### A. Spin-1/2 2d $J_1$ - $J_2$ Heisenberg model

The physical nature of the paradigmatic  $J_1$ - $J_2$  Heisenberg model on the square lattice is under debate for over decades, especially regarding the property of the ground state [20–24]. The frustration, i.e., the competition between interactions that precludes satisfying all the energetic gain, is considered to suppress the formation of long-range order, and thus it amplifies the nontrivial effect of quantum fluctuation. Together with geometrically frustrated magnets defined on e.g., triangular, Kagomé, and pyrochlore lattices, the  $J_1$ - $J_2$  Heisenberg model on square lattice has been investigated intensively by classical algorithms. Considering that the model is commonly recognized as one of the most challenging and physically intriguing quantum spin models, it is genuinely impactful to elucidate the quantum-classical crossover if exists at all.

The Hamiltonian of spin-1/2  $J_1$ - $J_2$  Heisenberg model on the square lattice is defined as

$$H = J_1 \sum_{\langle p, q \rangle} \sum_{\alpha \in \{X, Y, Z\}} S_p^\alpha S_q^\alpha + J_2 \sum_{\langle\langle i, j \rangle\rangle} \sum_{\alpha \in \{X, Y, Z\}} S_p^\alpha S_q^\alpha, \quad (\text{S2})$$

where the summation of the first and second terms concern pairs of nearest-neighbor and next-nearest-neighbor sites, respectively, and  $S_p^\alpha$  is the spin-1/2 operator on the  $p$ -th site that is related with the  $\alpha$ -th component of the Pauli matrices as  $S_p^\alpha = \frac{1}{2}\sigma_p^\alpha$ .

### B. 2d Fermi-Hubbard model

As the second representative model, we choose the Fermi-Hubbard model on the square lattice. The emergent phenomena in Fermi-Hubbard model is truly abundant, and provides a significant insights into electronic and magnetic properties of materials; the unconventional superfluidity or superconductivity, Mott insulating behaviour, and quantum magnetism. However, the intricate nature of Fermi statistics has hindered us from performing scalable and quantitative description in the truly intriguing zero-temperature regime.

The Hamiltonian of Fermi-Hubbard model on the square lattice reads

$$H = -t \sum_{\langle p, q \rangle, \sigma} (c_{p, \sigma}^\dagger c_{q, \sigma} + \text{h.c.}) + U \sum_p n_{p, \uparrow} n_{p, \downarrow}, \quad (\text{S3})$$

where  $c_{p, \sigma}^{(\dagger)}$  is the fermionic annihilation (creation) operator on site  $p$  with spin  $\sigma \in \{\uparrow, \downarrow\}$ ,  $n_{p, \sigma} = c_{p, \sigma}^\dagger c_{p, \sigma}$  is the corresponding number operator,  $t$  is the hopping amplitude, and  $U$  is the repulsive onsite potential.

### C. Spin-1 Heisenberg chain

The gap structure of translation and  $U(1)$ -invariant antiferromagnetic spin- $S$  chain has been argued to differ according to whether  $S$  is half-integer or integer. Such a statement has been known as the Haldane conjecture [59, 60], which has attracted interest of condensed matter physicists for over decades. While the ground states for half-integer  $S$  cases are considered to be gapless and hence there is no supporting argument to be simulated classically by polynomial time, it is reasonable to expect for integer  $S$  cases to be computed efficiently using, e.g., the matrix product state (MPS), since the entanglement entropy shall obey area law if the system is gapped as is predicted in Haldane conjecture [61]. In this context, it is not clear if there is any quantum advantage at all for simulating the ground state or the gap structure in integer- $S$  Heisenberg chain.

In this paper, we consider the simplest gapped case in which quantum advantage is unlikely; the spin-1 antiferromagnetic Heisenberg chain. The Hamiltonian reads

$$H = \sum_p \sum_{\alpha \in \{X, Y, Z\}} S_p^\alpha S_{p+1}^\alpha, \quad (\text{S4})$$

where  $S_p^\alpha$  is the spin-1 operator acting on the  $p$ -th site.

## S2. CLASSICAL SIMULATION OF GROUND STATE USING DENSITY-MATRIX RENORMALIZATION GROUP

### A. Overview of DMRG algorithm

The Density-Matrix Renormalization Group (DMRG) has been established as one of the most powerful numerical tools to investigate the strongly correlated one-dimensional (1d) quantum lattice models [31]. DMRG can be understood as a variational calculation based on the Matrix Product State (MPS) [33, 34]. Thanks to the area law of the entanglement entropy expected to hold for low-energy states of the 1d quantum lattice models [35], MPS is a quantitatively accurate variational ansatz for ground states of many quantum many-body systems [62]. Although MPS cannot cover the area law scaling for two or higher dimensional systems, DMRG is still applicable for quasi 1d cylinders or finite-size 2d systems. Indeed, we can find recent applications of DMRG to the 2d models treated in this study [53, 54]. We can also consider a 2d tensor network state, called Projected Entangled-Pair State (PEPS) or Tensor Product State (TPS), to calculate 2d lattice models [55, 56]. Although it might be more suitable than DMRG for simulating 2d systems because PEPS/TPS can cover 2d area law of the entanglement entropy, it has been widely used for direct simulations of the infinite 2d systems, and as far as we know, for a small 2d systems treated in this study, DMRG works more efficiently.

One problem with applying DMRG to 2d systems is that its computation cost may increase exponentially as we increase the system size  $N_{\text{site}}$  with keeping the same accuracy in the ground state energy. Because computation cost of PEPS/TPS is expected to increase polynomially as we increase  $N_{\text{site}}$ , it can be more efficient than DMRG for larger  $N_{\text{site}}$ . However, as we see in the main text, the crossover between classical and quantum computations seems to occur at the relatively small systems for the models we treated. Thus, we believe DMRG gives proper estimations of computational resources to simulate 2d systems in classical computer.

The computation time to obtain the ground state energy within a given target accuracy can depend on both the bond-dimension  $D$  and the optimization steps. Although the error in a ground state energy calculated by DMRG is expected to decrease exponentially as a function of  $D$  asymptotically, its general relationship depends on details of the target models. Similarly, it is not easy to estimate the necessary optimization steps *a priori*. Thus, to estimate the problem sizes where quantum computation will be superior to DMRG, we need to perform actual classical computations. In DMRG simulation, the computation time for the one optimization step, usually called sweep, scales as  $O(N_{\text{site}} D^3)$ , where  $N_{\text{site}}$  is the number of lattice sites.

### B. Error analysis and computation time estimate for two-dimensional models

In this subsection, we explain our procedure to estimate the computation time for the ground state energy estimation in 2d systems. For both the  $J_1$ - $J_2$  Heisenberg and the Hubbard models, we consider  $L_x \times L_y$  square lattice with the periodic boundary condition along  $x$  direction and the open boundary condition at  $y$  direction, so that the system forms a cylinder. In the DMRG calculation, the MPS string wraps around the cylinder as shown in Fig. S1.

To estimate the computation times in the ground state calculation by classical computer, we performed DMRG simulation using ITensor [30]. Typically, we set the maximum bond-dimension as  $D = D_{\text{max}}$ , and optimized the state



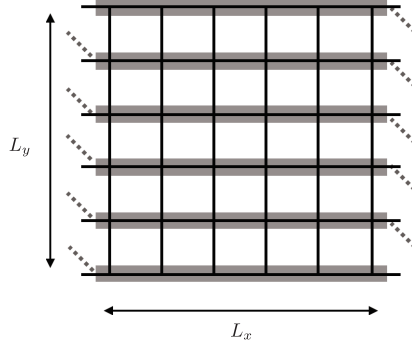


FIG. S1.  $L_x \times L_y$  square lattice used in the DMRG calculations. We consider the periodic boundary conditions along  $y$  direction and the open boundary condition along  $x$  direction. The gray lines indicate the assignment of MPS to the lattice sites.

starting from a random MPS with  $D = 10$ . We used  $U(1)$  symmetric DMRG for the Heisenberg models, and similarly we used particle number conservation for the Hubbard model. The most of the calculations have been done by a single cpu, AMD EPYC 7702, 2.0GHz, in the ISSP super computer center the University of Tokyo. We performed multithreading parallelization using four cores.

The estimation of computational time to reach desired total energy accuracy  $\epsilon$  is performed by the following three steps. Firstly, we optimize quantum states with various  $D_{\max}$ 's, and estimate the ground state energy by extrapolation. Then, we analyze the optimization dynamics of the energy errors. As we see in the main text, the dynamics of different  $D_{\max}$  almost collapse into a single curve. Finally, we estimate the elapsed time to obtain a quantum state with the desired accuracy by extrapolating this scaling curve. In the following, we elaborate on each step one by one.

As described above, firstly, we estimate the ground state energy by varying  $D_{\max}$ . It is known that the energy difference between the optimized and the exact energies is proportional to the so-called *truncation error*, which is a quantity obtained during the DMRG simulation. Namely, by iteratively updating the low-rank approximation by tensors for the MPS representation, one sums up the neglected singular values to compute the truncation error  $\delta$ . For sufficiently small truncation errors, the energy difference is empirically known to behave as

$$E_{\text{DMRG}}(D_{\max}) - E_{\text{exact}} \propto \delta(D_{\max}), \quad (\text{S5})$$

where  $\delta(D_{\max})$  is the truncation error for the optimized MPS state with  $D_{\max}$  [32, 63, 64]. We extrapolated obtained energies of target models to the zero truncation error using Eq. (S5). Fig. S2 shows typical extrapolation procedures for the  $J_1$ - $J_2$  Heisenberg model and the Fermi-Hubbard model on  $10 \times 10$  square lattice. When the truncation errors are sufficiently small, we observe the expected linear behaviors as in Figs. S2(a) and (b). However, in the case of the Hubbard model (Fig. S2(c)), the fitting by the linear function is not so precise. This is due to the limitation of the maximum bond dimension treated in our study. We also observed similar behavior in larger lattices in the  $J_1$ - $J_2$  model. Although the extrapolations seem to be not so accurate in such parameters, it is still sufficient to estimate the order of computation time, which is relevant in the comparison with the quantum computations.

Using the estimated value of ground state energy  $E_0$ , next we focus on the dynamics of the energy errors for each calculation. In Fig. S3, we show typical optimization dynamics as functions of the elapsed time. In the case of  $J_1$ - $J_2$  Heisenberg models with  $J_2/J_1 = 0, 0.5$ , we see that curves corresponding to various  $D_{\max}$  almost collapse to a universal optimization curve. Because the universal curve is likely a power function, we probably extrapolate optimization dynamics beyond the maximum value of  $D_{\max}$  treated in the calculations properly. In the case of the Hubbard model with  $U/t = 4$ , we did not see a perfect collapse into a universal curve. In addition, the optimization curve seems to be deviated from the power law. Similar behaviors are also observed other combinations of  $L$  and  $U/t$  for the Hubbard model. Although the extrapolation to larger  $D_{\max}$  becomes inaccurate for such cases, to estimate the order of the computation time, we performed a power-law fitting of  $E - E_0$  for the largest  $D_{\max}$  before the saturation.

Based on such power-law fittings of the maximum  $D_{\max}$  dynamics, finally, we estimate the computation time to obtain the ground state with the total energy error  $\Delta E \equiv E - E_{\text{exact}} = 0.01$ , where the unit of the energy is  $J_1$  for the Heisenberg model and  $t$  for the Hubbard model. In this work, we identify this quantity with the target energy accuracy  $\epsilon$ . Fig. S4 shows the estimated computation times for obtaining  $\epsilon = 0.01$  in classical DMRG simulations. The parameters for the DMRG calculations together with the estimated computation times are summarized in Tables S1 and S2. In the case of  $L \times L$  geometry (Fig. S4(a)), we see expected exponential increase of the elapsed time as we increase  $L$ . We find that the nearest neighbor Heisenberg model ( $J_2/J_1 = 0$ ) needs slightly shorter elapsed time than that of the frustrated model ( $J_2/J_1 = 0.5$ ). Although this is related to the difficulty of the problem, the

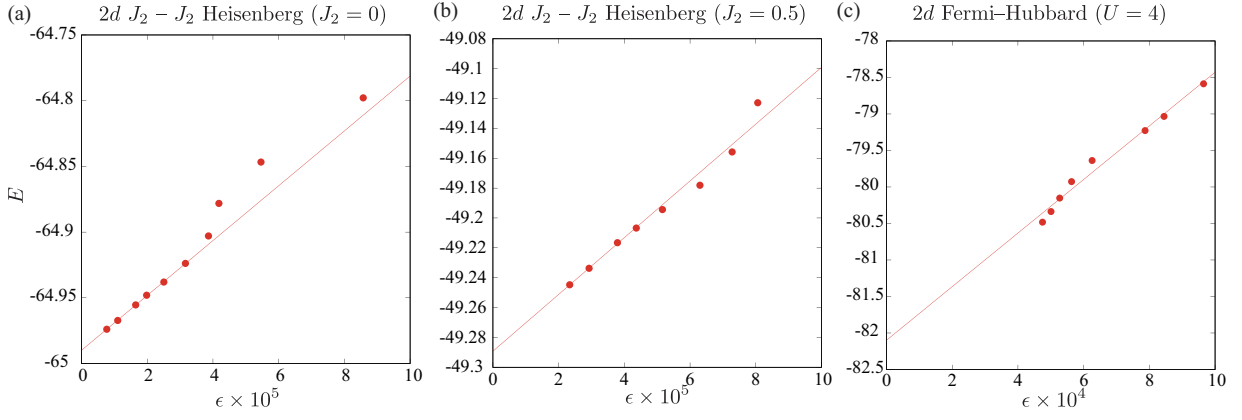


FIG. S2. The extrapolations of the ground state energies for  $10 \times 10$  square lattice models. Lines are the results of the linear fitting by Eq. (S5) (a)  $J_1$ - $J_2$  Heisenberg model with  $J_2 = 0$ . (b)  $J_1$ - $J_2$  Heisenberg model with  $J_2/J_1 = 0.5$ . (c) The Hubbard model with  $U/t = 4$ .

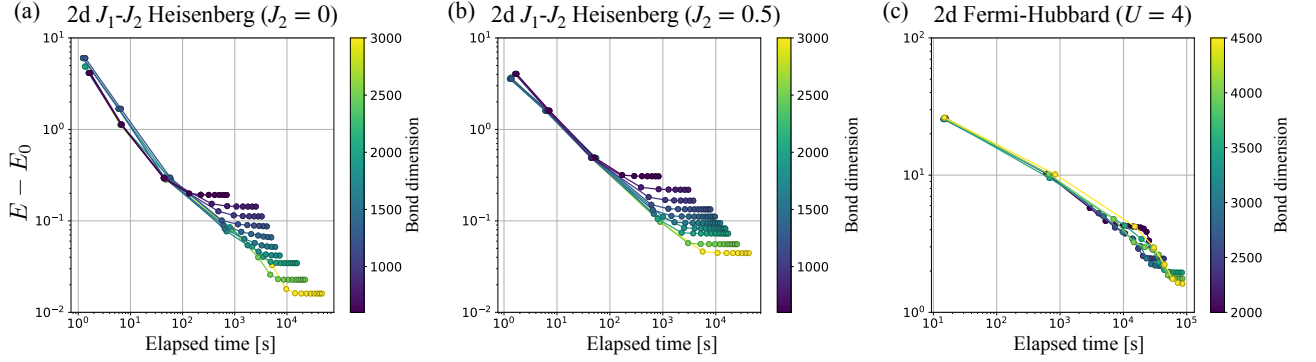


FIG. S3. Dynamics of energy errors for (a)  $J_1$ - $J_2$  Heisenberg model with  $J_2 = 0$ . (b)  $J_1$ - $J_2$  Heisenberg model with  $J_2/J_1 = 0.5$ . (c) The Hubbard model with  $U/t = 4$  in  $10 \times 10$  square lattice models with various  $D_{\max}$ .

difference is not so large when we consider the orders of the elapsed times. We observe rather larger difference between the Heisenberg and the Hubbard models, which is mainly attributed to the difference of number in local degrees of freedoms. In particular, the simulation in the Hubbard model is more time-consuming at  $U/t = 4.0$  than that of the  $U/t = 8.0$ . This is probably explained from the larger energy gap in  $U/t = 8.0$ , which indicates lower entanglement in the ground state.

It may be informative to mention that the runtime under the quasi-1d geometry ( $4 \times L$ ) in the Hubbard model does not increase exponentially (See Fig. S4(b)). Indeed, in this geometry we expect 1d area law of the entanglement entropy even when we increase  $L$ , and therefore the required bond dimension  $D$  to achieve a given target accuracy in the energy density becomes almost independent on  $L$ . Thus, we expect that the elapsed time to obtain  $\epsilon = 0.01$  in the total energy increases in power law as a function of  $L$ .

TABLE S1. Parameters for estimating the computation time in DMRG simulations of  $J_1$ - $J_2$  Heisenberg model.

$J_2/J_1$	$L_x$	$L_y$	largest $D_{\max}$	lowest energy	$E_0$	Estimated computation time (s) for $\Delta E = 0.01$
0	6	6	800	-23.090068	-23.090117	2.3
0	8	8	3000	-41.348977	-41.349310	$1.1 \times 10^2$
0	10	10	3000	-64.973863	-64.989896	$3.7 \times 10^4$
0	12	12	2500	-93.847557	-93.951521	$9.6 \times 10^5$
0.5	6	6	2000	-17.844007	-17.844015	2.9
0.5	8	8	1200	-31.538017	-31.544878	$1.9 \times 10^2$
0.5	10	10	3000	-49.244805	-49.289216	$7.9 \times 10^4$
0.5	12	12	2500	-70.699958	-70.782728	$1.3 \times 10^6$

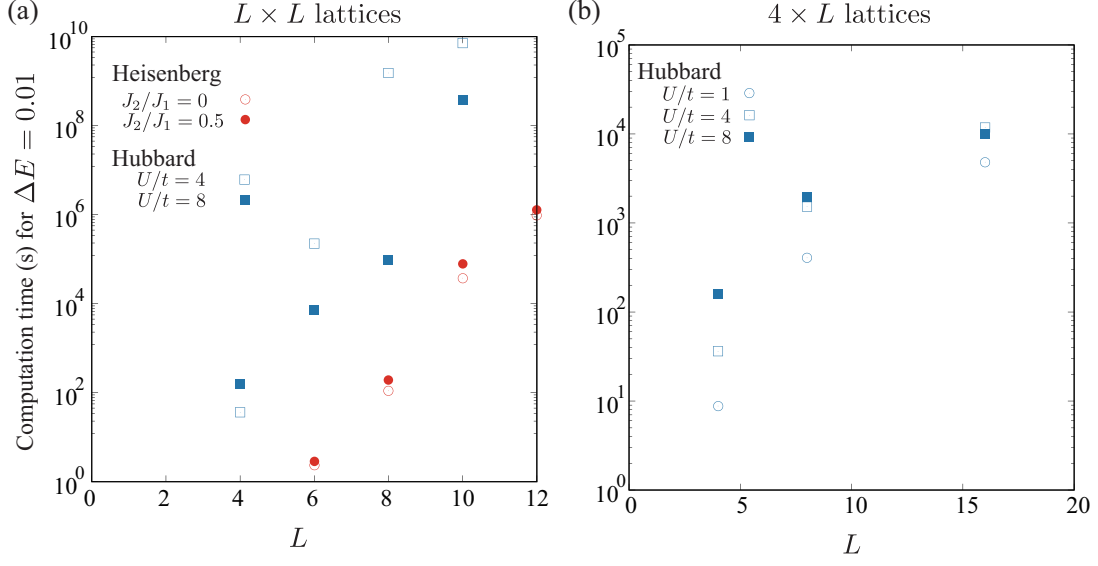


FIG. S4. Estimated computation time to obtain the ground states with the total energy error  $\Delta E \equiv E - E_{\text{exact}} = 0.01$ . (a) The estimated computation time for the  $J_1$ - $J_2$  Heisenberg and Hubbard models for  $L \times L$  square lattices. (b) The estimated computation time for the Hubbard models on  $4 \times L$  quasi-1d square lattices.

TABLE S2. Parameters for estimating the computation time in DMRG simulations of Hubbard model.

$U/t$	$L_x$	$L_y$	largest $D_{\text{max}}$	lowest energy	$E_0$	Estimated computation time (s) for $\Delta E = 0.01$
1.0	4	4	2500	-21.175239	-21.175265	8.8
1.0	8	4	3500	-43.486042	-43.487663	$4.1 \times 10^2$
1.0	16	4	3000	-88.230867	-88.240000	$4.8 \times 10^3$
4.0	4	4	2500	-12.801348	-12.801536	$3.6 \times 10$
4.0	6	6	3500	-29.081849	-29.302504	$2.2 \times 10^5$
4.0	8	4	3500	-26.674309	-26.676826	$1.5 \times 10^3$
4.0	8	8	5000	-52.008298	-52.802798	$1.5 \times 10^9$
4.0	10	10	4500	-80.482124	-82.098947	$7.1 \times 10^9$
4.0	16	4	3500	-54.495584	-54.509963	$1.2 \times 10^4$
8.0	4	4	2500	-7.660925	-7.660942	$1.6 \times 10^2$
8.0	6	6	3500	-17.737197	-17.767700	$7.4 \times 10^3$
8.0	8	4	3500	-16.079582	-16.079696	$2.0 \times 10^3$
8.0	8	8	5000	-31.806322	-31.993896	$9.4 \times 10^4$
8.0	10	10	5000	-49.287802	-51.699085	$3.7 \times 10^8$
8.0	16	4	3500	-32.922474	-32.923098	$9.9 \times 10^3$

In the above estimations, we used a single cpu. In practical calculations, we may expect speed up by GPU, or parallelization using many cpus. Indeed, in our simulation based on ITensor, we observed tens times faster execution by GPU when we did not impose the symmetries. Although ITensor simulation with the symmetry did not run with GPU, unfortunately, this observation indicates the estimated elapsed time can be shorter with a factor of  $10^{-1}$ . In the case of multi-node parallelization, we may consider real-space decomposition of the DMRG algorithm [65]. In this approach, each cpu optimizes different region of the lattice (MPS), and communicates each other to exchange the information of the tensors. Because this approach needs to keep a sufficiently large block (set of tensors) for each cpu to obtain meaningful speed up, in the present systems sizes, we divide the system into dozens at most. Thus, we estimate that the multi-node parallelization may give us shorter elapsed time with a factor of  $10^{-1}$ .

We remark that here we estimated the computation time to actually obtain a quantum state whose energy error is within  $\epsilon = 0.01$ , so that other observables can be extracted consistently. Meanwhile, the runtime becomes much shorter if we merely focus on merely estimating the energy within the error  $\epsilon = 0.01$ , since the zero-truncation extrapolation within error  $\epsilon$  itself can be done with smaller  $D$ . Indeed, we have observed that extrapolations allows

us to reach smaller error than the energies obtained from the actual DMRG simulations. This fact indicates that we might need shorter computation time to estimate the ground state energy within  $\epsilon = 0.01$  in classical computer, although we point out that such a data analysis may also be available in quantum algorithms as well.

### C. Error analysis and computation time estimate for one-dimensional $S = 1$ Heisenberg model

In this subsection, we explain the runtime analysis of the 1d  $S = 1$  Heisenberg model. We consider the following Hamiltonian which is composed of  $N_{\text{site}}$  sites in total, with the edge sites being  $S = 1/2$  spins and the  $N_{\text{site}} - 2$  bulk sites corresponding to  $S = 1$  spins as

$$\mathcal{H} = \sum_{i=1}^{N_{\text{site}}-3} \mathbf{S}_i \cdot \mathbf{S}_{i+1} + J_{\text{end}} (\mathbf{s}_0 \cdot \mathbf{S}_1 + \mathbf{S}_{N_{\text{site}}-2} \cdot \mathbf{s}_{N_{\text{site}}-1}), \quad (\text{S6})$$

where  $J_{\text{end}}$  denotes the interaction amplitude of the  $S = 1$  and  $S = 1/2$  spins. It has been pointed out that, thanks to the additional  $S = 1/2$  spins  $\mathbf{s}_0$  and  $\mathbf{s}_{N_{\text{site}}-1}$ , we avoid degeneracy between the total spin  $S = 0$  and  $S = 1$  sectors in the thermodynamic limit by taking  $J_{\text{end}}$  sufficiently large [32, 66]. Here we exclusively take  $J_{\text{end}} = 0.7$  in the current work. Since the entanglement entropy of ground state is expected to obey 1d area law in this model, the DMRG algorithm is suitable to simulate larger system sizes. We also remark that, by extrapolating the energy gap between  $S = 0$  and  $S = 1$  sectors to  $N_{\text{site}} \rightarrow \infty$ , we can estimate the famous Haldane gap [67].

To estimate the runtime of classical DMRG algorithm, we executed the optimization using ITensor library as in the previous sections [30]. We used  $U(1)$ -symmetric DMRG to calculate the lowest energy states for  $S_z = 0$  and  $S_z = 1$  sectors, which we have confirmed to be the lowest energy states for  $S = 0$  and  $S = 1$ , respectively. In this model, we easily obtain sufficiently small truncation errors around  $\delta(D_{\text{max}}) \simeq 10^{-10}$  with  $D_{\text{max}} \lesssim 300$ . Thus, we regard the lowest energy obtained in each sector along DMRG simulation as  $E_0$  and see  $\epsilon = E - E_0$ . The most of the calculations have been done by a single cpu, 3.3GHz dual core Intel Core i7 on MacBook Pro (13-inch, 2016).

Fig. S5 shows the dynamics of  $\epsilon$  determined from the above procedure. In sharp contrast with the previous 2d models, we can easily reach  $\epsilon \ll 10^{-2}$ . In the case of the total  $S = 0$  sector, we expect a gapped ground state, and therefore the required  $D_{\text{max}}$  is almost independent from  $N_{\text{site}}$ . This nature is also reflected in the very rapid decay of  $\Delta E$ , as can be seen from Fig. S5 (a). On the contrary, in the total  $S = 1$  sector we expect that the lowest energy state to be gapless. Thus, the entanglement entropy gradually increases as  $\log N_{\text{site}}$ , and therefore we need to increase  $D_{\text{max}}$  as we increase  $L$ . This fact is related to relatively slower decays of  $\epsilon$  in Fig. S5(b). We make another remark on the optimization dynamics in the total  $S = 1$  sector; here we observed that  $D_{\text{max}}$  becomes largest at an intermediate steps of the optimization dynamics. Such a non-monotonic behavior in the bond-dimensions might be possibly caused by local minima which presumably arised by imposing symmetry on tensors of MPS ansatz: To escape from local minima we may need larger bond dimension.

Finally, we estimate the computation time as the intersection of  $\epsilon$  dynamics and  $\epsilon = 0.01$ . Thus obtained computation time is shown in Fig. S6(a), and the parameters in the simulation is summarized in Table S3. We see that the computation time is almost proportional to  $N_{\text{site}}$ , which is expected from the almost constant  $D_{\text{max}}$  in the optimized state. We see that the  $D_{\text{max}}$  in the total  $S_z = 1$  sector slightly increases as we increase  $N_{\text{site}}$ . This is probably related to the gapless nature of the lowest energy state within the total  $S = 1$  sector. Such weak  $N_{\text{site}}$  dependence appears also in the estimated computation time of the total  $S_z = 1$  sector, which is always longer than the computation time for the gapped ground state in the total  $S = 0$  sector.

Let us remark that, runtime analysis on quantum algorithm reveals that the quantum advantage in this model is unlikely. In Fig. S6(b), we show the runtime in comparison with the qubitization-based quantum phase estimation (whose detail is described in Sec. S7 and S8). Since the phase estimation algorithm aiming for the current  $\epsilon$  requires runtime that scales at least quadratically with respect to the system size, the large separation already at moderate size of  $N_{\text{site}} = O(10^2)$  implies that there is very low chance of DMRG simulation being surpassed by the quantum algorithm.

## S3. QUANTUM ALGORITHMS FOR ESTIMATING ENERGY SPECTRA

### A. Overview on quantum phase estimation

Quantum phase estimation (QPE) is a quantum algorithm designed to extract the eigenphase  $\phi$  of a given unitary  $U$  up to  $m$  digits, using  $m$  ancilla qubits that indirectly read out the complex phase of the target system. More precise description of the algorithm originally proposed by Kitaev [68] is as follows: given an efficiently prepared trial



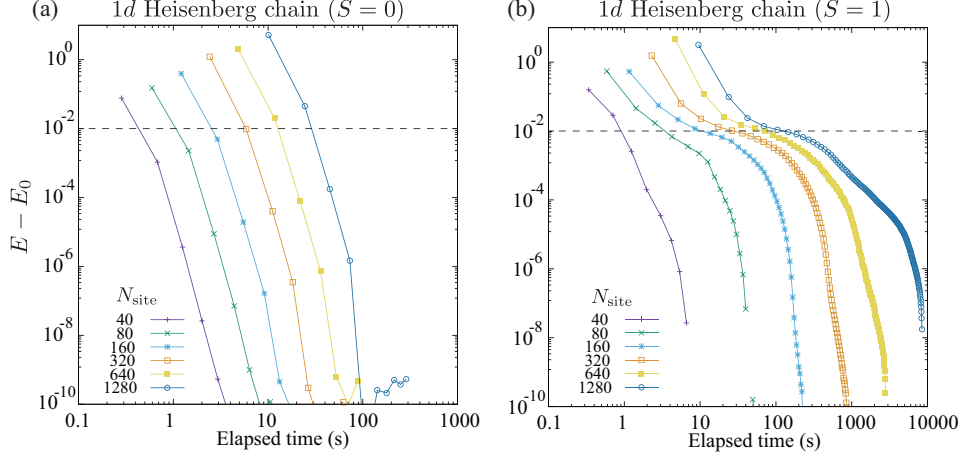


FIG. S5. Dynamics of energy errors for  $S = 1$  Haldane chain for various  $N_{\text{site}}$ . (a)  $S = 0$  sector (b)  $S = 1$  sector. Horizontal dashed line indicate  $\epsilon = E - E_0 = 0.01$ .

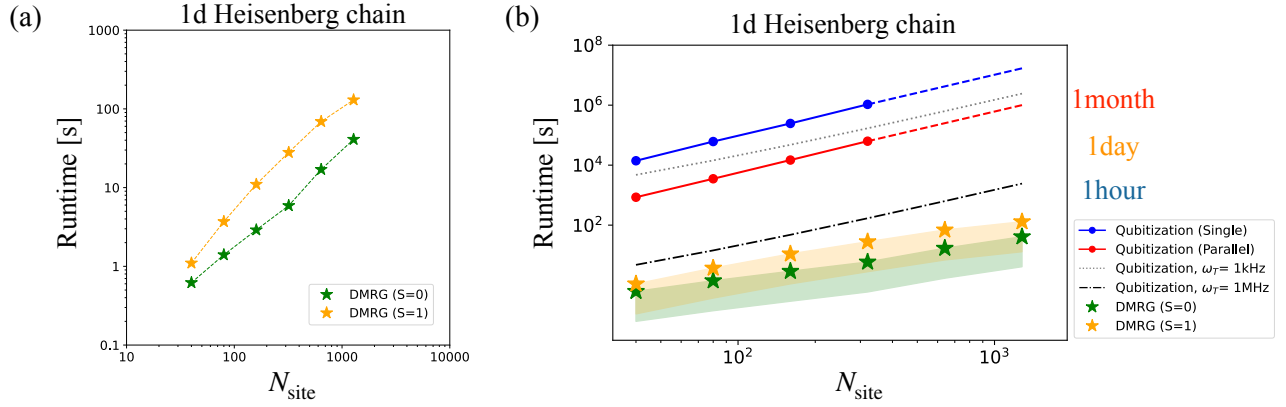


FIG. S6. (a) Estimated computation time to obtain  $\epsilon = 0.01$  in the  $S = 1$  Heisenberg chain defined in Eq. (S6). (b) Runtime comparison with qubitization-based quantum phase estimation. Notations follow those of Fig. 3 in the main text.

state  $|\psi\rangle = |0\rangle$  whose fidelity with the  $k$ -th eigenstate  $|k\rangle$  of the unitary is given as  $f_k = \|\langle k|\psi\rangle\|^2$ , a single run of QPE returns a random variable  $\hat{\phi}$  which corresponds to a  $m$ -digit readout of  $\phi_k$  with probability  $f_k$ . See Fig. S7 for a representative quantum circuit structure for the quantum phase estimation. By plugging a time evolution operator  $U = e^{-iHt}$  of Hamiltonian  $H$  and take  $|\psi\rangle$  to be efficiently-preparable approximation of the eigenstate, for instance, one can simulate the eigenspectrum of the target Hamiltonian  $H$  [38].

In this work, we focus on the simulation of ground state and its eigenenergy, within some target accuracy, of a quantum many-body Hamiltonian considered in condensed matter physics. Although the simulation of the ground state of a general Hamiltonian is a QMA-hard problem, we envision that quantum advantage can be realized in a practical sense, since the Hamiltonian simulation is BQP-complete and cannot be replaced by any classical algorithm efficiently. In this regard, our goal is to elucidate the quantum-classical crosspoint based on the actual runtime to prepare a many-body quantum state up to some fixed accuracy in terms of the energy. The detailed procedure for classical algorithm has already been provided in Sec. S2, and thus we detail on the quantum algorithm in the following. In particular, we explain the abstract protocol of cost/runtime estimation strategy in Sec. S3B, and then proceed to Sec. S3C, S3D in order to provide different flavors of Hamiltonian simulation techniques, which constitute the main building block of the phase estimation algorithm.

TABLE S3. Parameters for estimating the computation time in DMRG simulations of Haldane chain defined as Eq. (S6) with  $J_{\text{end}} = 0.7$ .

total $S_z$	$N_{\text{site}}$	$D_{\text{max}}$ in the optimized state	lowest energy	Estimated computation time (s) for $\Delta E = 0.01$
0	40	90	-53.293707633101	0.62
0	80	90	-109.35306916448	1.4
0	160	90	-221.47179222696	2.9
0	320	90	-445.70923835198	5.9
0	640	90	-894.18413060185	17
0	1280	90	-1791.13391510219	41
1	40	134	-52.861104764355	1.1
1	80	156	-108.934890997408	3.7
1	160	169	-221.058987851845	11
1	320	175	-445.298116034289	28
1	640	177	-893.773481949644	69
1	1280	179	-1790.7233920146	$1.3 \times 10^2$

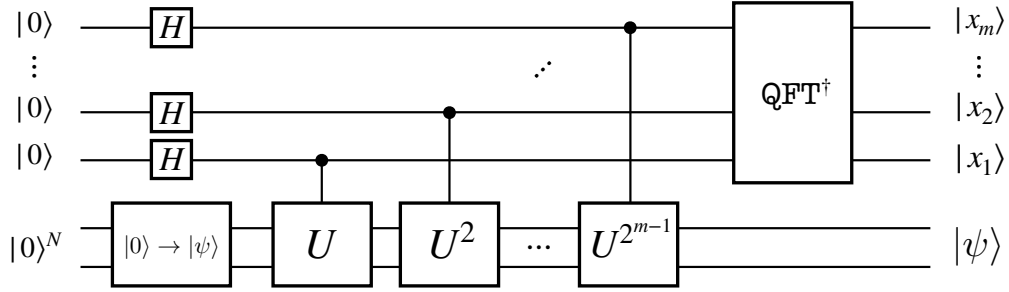


FIG. S7. Quantum circuit structure for  $m$ -digit phase estimation on the trial state  $|\psi\rangle$  for the unitary  $U$ .

### B. General cost estimation strategy for phase estimation

The gate complexity, or more abstractly the cost  $C_{\text{total}}$ , for running the QPE under the circuit structure in Fig. S7 can be given as

$$C_{\text{total}} = C_{\text{trial}} + C_{\text{HS}} + C_{\text{QFT}^\dagger}, \quad (\text{S7})$$

where the cost  $C_{\text{trial}}$  is for preparation of the trial state,  $C_{\text{HS}} = 2^m C_{\text{CU}}$  is for simulating the dynamics with  $C_{\text{CU}}$  each for a single control- $U$  operation, and  $C_{\text{QFT}^\dagger}$  for the inverse quantum Fourier transformation (QFT). As we explain the reason in the following, we exclusively focus on the cost from the second term of Eq. (S7), and discuss the runtime solely from it.

For the first term  $C_{\text{trial}}$ , we assume that the overlap between the trial state  $|\psi\rangle$  and the exact ground state  $|GS\rangle$  does not shrink substantially along the increase of system size, and that  $C_{\text{trial}}$  scales polynomially (in particular with low power) with respect to the system size. For instance, we may perform the adiabatic state preparation, i.e., preparing a ground state by gradually modifying the Hamiltonian from a trivial (or classically well-known) one into the desired one. Many exotic quantum states to be studied are distinct from the trivial phase in terms of the second-order phase transition, rather than the first-order ones, and therefore the gap size  $\Delta$  obeys sub-exponential shrinking (otherwise it negates the quantum advantage of the phase estimation algorithm). Alternatively one may prepare trial states using the Krylov method that is based on the linear combination of unitary technique [69]. The required Krylov dimension scales inverse-quadratically with respect to the spectral gap size as  $D = O(1/\Delta^2)$  under constant target accuracy. In particular in the case of target models we consider in the current work, the spectral gap scales at most as  $\Delta = O(1/\sqrt{N})$  and therefore reasonable to neglect in the resource estimation. A more detailed and holistic analysis on the variety of systems is left as a future work. For the third term  $C_{\text{QFT}^\dagger}$ , we argue that this is the most irrelevant for the runtime; while the second term consumes exponential cost with respect to  $m$ , the inverse QFT can be implemented by  $O(m \log(m))$  (which is also denoted as  $\tilde{O}(m)$  in literature.).

In this paper, we analyze the runtime of the QPE required to reach some target energy accuracy  $\epsilon$  to estimate the ground state energy of a quantum many-body Hamiltonian. We find that the number of gates required to reach

the total energy accuracy  $\epsilon = 0.01$  scales at least quadratically with respect to the system size, and therefore we focus on implementation of fault-tolerant quantum computers. In particular, we investigate the cost by assuming that the quantum gates are synthesized under logical operations available in the framework of the surface code. Among multiple reasons for the choice of the error correcting code, the most notable ones are the realizability in hardware platforms with 2D qubit arrays and the high threshold property.

Estimation of the runtime of the phase estimation is performed via two steps. First, we perform a comprehensive comparison between multiple flavors of Hamiltonian simulation, which are roughly divided into Trotter-based and post-Trotter methods. Given the explicit quantum circuit structure in individual algorithms, we compute the  $T$ -count respectively to determine the best among the existing methods. Note that such an estimation procedure is reasonable; in a situation when the logical Clifford operations can be efficiently implemented through stabilizer measurements and feedback, the runtime is dominated by the execution of  $T$ -gates, which is the most basic unit for non-Clifford operations under the surface code. In the second step, which is detailed in Sec. S7, the runtime of the presumably best quantum algorithm is further analyzed by compiling the quantum circuit at the level of executable instructions. This yields a more precise runtime estimate with plausible quantum hardware setups. In the remainder of this section, we introduce the Hamiltonian simulation techniques considered in our work, and also discuss their  $T$ -complexity and the effect of prefactors.

### C. Trotter-based Hamiltonian Simulation methods for phase estimation

Among various flavors of Hamiltonian simulation algorithms for quantum computers, the ones based on the Suzuki-Trotter decomposition have been known from the earliest days. Since universal quantum computers are mostly designed to execute quantum gates that operate only on constant number of qubits, they cannot directly implement the matrix exponentiation as  $U = e^{-iHt}$  where we assume that the Hamiltonian is decomposed into sum of Pauli operators as  $H = \sum_l w_l H_l$  (we tune the phase so that  $w_l > 0$ ). The Suzuki-Trotter decomposition refers to the deterministic procedure that approximates the unitary evolution by using a sequence of Hermitian operators  $\mathcal{M} = (\dots, M_j, \dots)$  to implement the product formula which is both spacially and temporally discretized as

$$U := \exp\left(-i \sum_l w_l H_l t\right) \approx \left(\prod_j e^{-iM_j t/r}\right)^r. \quad (\text{S8})$$

For instance, in the case of the first-order product formula, the Hermitian operators are simply taken as  $\mathcal{M} = (\dots, w_l H_l, \dots)$  such that

$$U_{\text{Trotter},1} = \left(\prod_l e^{-i w_l H_l t/r}\right)^r, \quad (\text{S9})$$

whose error from the exact implementation is bounded by the operator norm as

$$\|U - U_{\text{Trotter},1}\| = \mathcal{O}\left(\frac{(L\Lambda t)^2}{r}\right). \quad (\text{S10})$$

Here,  $L$  denotes the number of decomposition for Hamiltonian,  $r$  is the number of repetitions, and  $\Lambda = \max_l w_l$  is the largest coefficient. The higher order product formulae were also invented by Suzuki to improve the scaling with respect to the simulated time  $t$  [48]. For instance, the second order product formula is given by taking  $\mathcal{M} = (w_1 H_1/2, \dots, w_{L-1} H_{L-1}/2, w_L H_L, w_{L-1} H_{L-1}/2, \dots, w_1 H_1/2)$  as

$$S_2(\tau) := \prod_{l=1}^L \exp(w_l H_l \tau/2) \prod_{l=L}^1 \exp(w_l H_l \tau/2), \quad (\text{S11})$$

and further the  $2k$ -th order product formula is given by the following recursive procedure as

$$S_{2k}(\tau) := [S_{2k-2}(g_k \tau)]^2 S_{2k-2}((1 - 4g_k \tau) S_{2k-2}(g_k \tau))^2, \quad (\text{S12})$$

where  $g_k = 1/(4 - 4^{1/(2k-1)})$  ( $k > 1$ ). By taking the time evolution unitary as  $U_{\text{Trotter},2k} = (S_{2k}(-it/r))^r$ , it follows that the error of the Hamiltonian simulation can be given as

$$\|U - U_{\text{Trotter},2k}\| = \mathcal{O}\left(\frac{(L\Lambda t)^{2k+1}}{r^{2k}}\right). \quad (\text{S13})$$

Algorithm	Error	Gate complexity
Trotter, 1st order	$\mathcal{O}\left(\frac{(L\Lambda t)^2}{r}\right)$	$\mathcal{O}\left(\frac{L^3(\Lambda t)^2}{\epsilon_{\text{HS}}}\right)$
Trotter, $2k$ -th order	$\mathcal{O}\left(\frac{(L\Lambda t)^{2k+1}}{r^{2k}}\right)$	$\mathcal{O}\left(\frac{L^{2+1/2k}(\Lambda t)^{1+1/2k}}{\epsilon_{\text{HS}}^{1/2k}}\right)$
Random Trotter, $2k$ -th order	$\mathcal{O}\left(\frac{(L^{2k}(\Lambda t)^{2k+1})}{r^{2k}}\right)$	$\mathcal{O}\left(\frac{L^2(\Lambda t)^{1+1/2k}}{\epsilon_{\text{HS}}^{1/2k}}\right)$
qDRIFT	$\mathcal{O}\left(\frac{2\lambda^2 t^2}{r}\right)$	$\mathcal{O}\left(\frac{(\lambda t)^2}{\epsilon_{\text{HS}}}\right)$

TABLE S4. Gate complexity and error scaling of Trotter-based methods to perform Hamiltonian simulation for time  $t$ .

Algorithm	$N_{\text{Rot}}$	$T$ -count	$T$ -complexity
Random, 2nd order Trotter	$16 \frac{\Lambda^3 L^2}{\epsilon^{3/2}}$	$N_{\text{Rot}} \times (8 \log_2 \epsilon_{\text{SS}}^{-1} + 20)$	$\mathcal{O}\left(\frac{N^2}{\epsilon^2} \log(N/\epsilon^{3/4})\right)$
qDRIFT	$35.5192 \frac{\lambda^2}{\epsilon^2}$	$N_{\text{Rot}} \times (8 \log_2 \epsilon_{\text{SS}}^{-1} + 20)$	$\mathcal{O}\left(\frac{N^2}{\epsilon^2} \log(N/\epsilon)\right)$

TABLE S5.  $T$ -count of Trotter-based methods to perform phase estimation up to energy accuracy  $\epsilon$ . Here we assume that the Pauli rotations are implemented with gate synthesis error  $\epsilon_{\text{SS}} = \epsilon_{\text{S}}/2N_{\text{Rot}}$  where  $\epsilon_{\text{S}}$  is the total gate synthesis error. The number of controlled Pauli rotations are estimated under the assumption of using the Hodges-Lehmann estimator, from which the  $T$ -counts are calculated by multiplying the cost per controlled Pauli rotation (Also see Sec. S5 for  $T$ -count of basic quantum operations).

The product formula enables one to systematically improve the error with respect to, e.g., simulation time  $t$ . Meanwhile, when we count the gate complexity on quantum computers, the prefactor suffers from exponential increase with respect to the order  $k$  [46], and therefore is not preferred in practice. An intriguing alternative is to introduce the randomization into the gate compilation [44, 70, 71]. For instance, it has been pointed out that, by randomly permuting the sequence of operators  $\{H_l\}$  in Eq. (S11) for the second-order product formula improves the error dependence on  $L$  [44]. See Table S4 for the comparison on the gate complexity and error scaling.

While the randomized Trotter methods have performed randomization concerning the order of the Pauli rotations, it was proposed by Campbell that we may stochastically choose the Pauli rotations according to their coefficients in the Hamiltonian to suppress the simulation cost for Hamiltonians that are composed of large numbers of Pauli with small coefficients [46]. To be concrete, according to the probability  $p_l = w_l/\lambda$  where  $\lambda := \sum_l w_l$ , we choose the Pauli operator  $H_l$  and append the Pauli rotation  $e^{-iH_l t/r}$  to the circuit, which is repeated for  $r$  times. It has been shown that the error scaling in such a technique, called the qDRIFT, is given rather by the L1 norm of the coefficients  $\lambda$  rather than the number of Paulis  $L$  [See Table S4].

### 1. $T$ -count in Trotter-based methods

The error analysis on the Hamiltonian simulation eventually allows one to analyze the cost to perform the phase estimation up to a target energy accuracy  $\epsilon$ . For instance, Campbell estimated the number of digits  $m$  required to read out the energy with  $\epsilon$  with success probability  $1 - p_f$  as [46]

$$m = \log_2(\epsilon/2\lambda) + \log_2\left(\frac{1}{p_f} + 1\right) - 2. \quad (\text{S14})$$

By optimizing the gate synthesis accuracy for each control- $U^{2^j}$  such that the overall gate count is minimized under a fixed total error, one finds that the total number of rotation gates is given as

$$N_{\text{Rot}} \sim 133 \frac{\lambda^2}{\epsilon^2((3/2)p_f)^3}. \quad (\text{S15})$$



While this analysis assumes to run the QPE for a single shot, Lee *et al.* introduced another layer of “randomization” [18]; by running the phase estimation multiple times, one may sample from the somewhat erroneous probability distribution, whose error can be efficiently suppressed by the Hodges-Lehman estimator to deal with the fat-tail errors. By assuming that the error in the output is symmetric, one obtains the improved number of rotations as

$$N_{\text{Rot}} = 35.5192 \frac{\lambda^2}{\epsilon^2}. \quad (\text{S16})$$

Given the number of rotations, one may estimate the  $T$ -count by multiplying with the gate synthesis cost for controlled rotations. See Table S5 for the summary of the cost required to perform the phase estimation. Note that we also perform a similar analysis in the case of the 2nd order random Trotterization.

#### D. Post-Trotter Hamiltonian simulation methods for quantum phase estimation

One of the main bottlenecks of the Trotter-based Hamiltonian simulation techniques is that their gate complexity is polynomial regarding the dynamics simulation accuracy  $\epsilon_{\text{HS}}$ . Although one may in principle improve the gate-depth scaling as  $O(\epsilon_{\text{HS}}^{-1/2k})$  by employing  $2k$ -th order product formulas, one must pay the cost of significantly increased prefactor, which practically negates the advantage of the scaling in moderate-size problems. This has been recognized as roadblock that prevents us from achieving quantum advantage in a practical sense.

A class of Hamiltonian simulation techniques that achieves exponential improvement with respect to the accuracy  $\epsilon_{\text{HS}}$  is called the “post-Trotter methods.” While Trotter-based methods mainly consist of exponentiated Pauli rotations that act on the system qubits, in post-Trotter methods the class of available operations on the target system is vastly extended to include even non-unitary operations by making use of an extended Hilbert space. This technique is dubbed as *block-encoding*. For instance, Ref. [49, 50] proposed an algorithm that block-encodes the truncated Taylor series for the time evolution operator. The gate complexity to perform the phase estimation based on this so-called *Taylorization* method for lattice systems with size  $N$  with energy accuracy  $\epsilon$  is  $\frac{N}{\epsilon} \log(N/\epsilon_{\text{HS}})/\log \log(N/\epsilon_{\text{HS}})$  [72], which is exponentially more efficient than the Trotter-based methods. A major innovation pointed out by Refs. [73, 74] is that one may completely eliminate the Trotter or Taylor errors in phase estimation by simulating  $e^{i \arccos(H/\lambda)}$  instead of  $e^{iHt/\lambda}$ . This idea has been combined with the concept of *qubitization* [52] to achieve even more efficient implementation of phase estimation algorithm [75]. As we later describe more in detail in Sec. S3 D 2, we construct oracles such that the operation of the block-encoding unitary can be “qubitized” into a direct sum of two-dimensional subspace. Each of such “single-qubit rotation” encodes the eigenvalue of the target operator, and therefore can be directly plugged in as a phase estimation subroutine.

In the following, we first introduce the concept of block encoding and its two core subroutines **PREPARE** and **SELECT**. Then, we further introduce the qubitization and Taylorization algorithms, which are two representative post-Trotter methods to perform Hamiltonian simulation for phase estimation.

##### 1. Block encoding for linear combination of unitaries

It is instructive to start from the definition of the term block encoding. Let us define that block encoding of some bounded-norm target operator  $A \in M_d(\mathbb{C})$  ( $d$ : Hilbert space dimension) is realized when the action of an unitary operator in an extended Hilbert space  $V \in M_{d+d_a}(\mathbb{C})$  ( $d_a$ : auxiliary Hilbert space dimension) reproduces  $A$  at specific subspace. For concreteness, let us consider  $n$ -qubit target system with  $a$  ancillary qubits. We say that “ $A$  is block-encoded into  $V$  via signal state  $|\mathcal{L}\rangle$ ” if the following holds:

$$(\langle \mathcal{L}| \otimes I^{\otimes n}) V (|\mathcal{L}\rangle \otimes I^{\otimes n}) = A, \quad (\text{S17})$$

where  $|\mathcal{L}\rangle$  is a state in auxiliary  $a$ -qubit Hilbert space and  $I$  denotes the identity. Note that we have assumed that  $\|A\| \leq 1$  without loss of generality, since we can rescale the operator as  $A/\alpha$  ( $\alpha \in \mathbb{R}$ ) if needed. While we may also consider block encoding under multiple signal states as  $\Pi V \Pi = A$  where  $\Pi = \sum_{\mathcal{L}} \Pi_{\mathcal{L}} = \sum_{\mathcal{L}} |\mathcal{L}\rangle \langle \mathcal{L}|$ , here we focus on Eq. (S17) for simplicity. It is illustrative to take  $|\mathcal{L}\rangle = |0\rangle^{\otimes a}$  and rewrite Eq. (S17) into an equivalent expression that holds for any target state:

$$V = \begin{pmatrix} A & * \\ * & * \end{pmatrix}, \quad (\text{S18})$$

Observe from Eq. (S18) why the technique is called “block-encoding.” Since we can obtain the desired operation  $A|\psi\rangle$  with finite probability by post-selecting the measured ancillary qubits to be  $|0\rangle^{\otimes a}$ , this is also referred to as

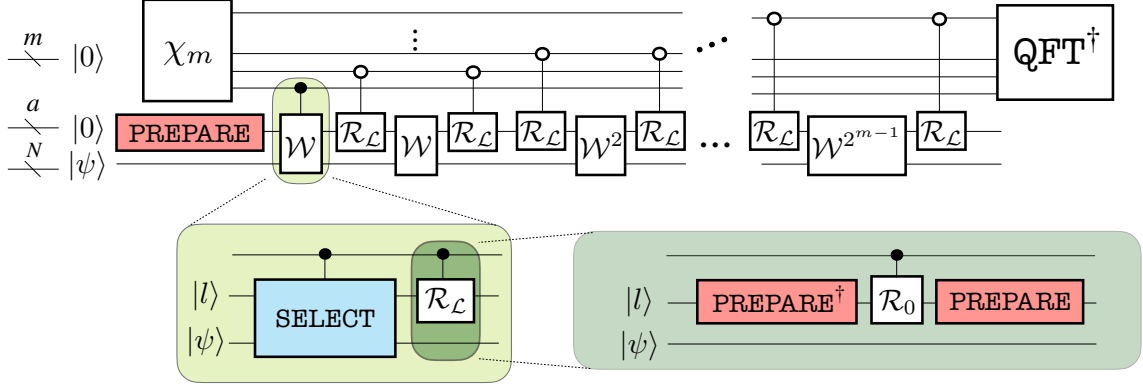


FIG. S8. Quantum circuit structure of qubitization-based phase estimation algorithm. The definitions of **PREPARE** and **SELECT** are given in Eqs. (S20), (S22), where the target block-encoded operator  $A$  is taken as the Hamiltonian here.

“probabilistic implementation of  $A$ .” In reality, we design the algorithm (e.g. use amplitude amplification) so that post selection is not explicitly required.

In phase estimation algorithm based on post-Trotter methods, one aims to extract information on the eigenspectra by making multiple queries to the oracular unitary which block-encodes the Hamiltonian. The underlying assumption is that, there is a systematic and efficient way to encode the spectral information of the Hamiltonian into the oracular unitary  $V$ . As we later observe in the algorithms such as the qubitization and Taylorization, this question essentially falls into the problem of implementing two oracular subroutines named **PREPARE** and **SELECT** efficiently. Roughly speaking, **PREPARE** takes the ancillary quantum state to the properly block-encoded subspace, and **SELECT** performs the block encoding of the Hamiltonian in the subspace given by the first oracle **PREPARE**.

To explicitly write down the operation by two subroutines, first, let us note that any operator  $A$  can be decomposed into a linear combination of unitaries as

$$A = \sum_l w_l A_l \quad (w_l > 0), \quad (\text{S19})$$

where  $w_l$  is a real positive coefficient of the unitary operator  $A_l$ . For  $n$ -qubit systems,  $A_l$  can be thought to be a tensor product of multiple Pauli operators with arbitrary complex phase. The first oracle **PREPARE** is often introduced to perform the following transformation that encodes all  $L$  coefficients of the Hamiltonian into the ancillary qubits as

$$|\mathcal{L}\rangle := \text{PREPARE} |0\rangle^{\otimes a} = \sum_{l=1}^L \sqrt{\frac{w_l}{\lambda}} |l\rangle, \quad (\text{S20})$$

where  $\lambda = \sum_l w_l$  is the  $L_1$  norm of the coefficients of Hamiltonian. One of such **PREPARE** operation can be written for instance as  $\text{PREPARE} = \sum_{l=1}^L \sqrt{\frac{w_l}{\lambda}} |l\rangle \langle 0|$ . Given the orthogonal bases  $\{|l\rangle\}_l$  that encodes the information of the coefficients, next we construct the second oracle **SELECT** so that the desired operator  $A$  is realized in the subspace as

$$(\langle \mathcal{L}| \otimes I) \text{SELECT} (|\mathcal{L}\rangle \otimes I) = \frac{A}{\lambda}. \quad (\text{S21})$$

While the construction of **SELECT** oracle is not unique, it is instructive to introduce an example as follows:

$$\text{SELECT} = \sum_l |l\rangle \langle l| \otimes A_l + \sum_{\bar{l}} |\bar{l}\rangle \langle \bar{l}| \otimes I, \quad (\text{S22})$$

where we have introduced  $\bar{l}$  to denote computational bases of ancillary qubit system on which **SELECT** acts trivially.

## 2. Qubitization

Ref. [52] pointed out that, by choosing the operator  $A$  in Eq. (S19) to be the Hamiltonian of the target system, one may construct a unitary that invokes rotational operation for each eigenstates. Since all the rotation is performed disjointly on two-dimensional subspace, such a specific form of block encoding is referred to as the *qubitization*.

Let  $A = \sum_{\chi} \chi |\chi\rangle \langle \chi|$  be a target Hermitian operator which we wish to block-encode into the **SELECT** operator via the signal state  $|\mathcal{L}\rangle = \text{PREPARE}|0\rangle$  as in Eq. (S20), (S22), (S21). To understand the “qubitized” picture, we focus on a single eigenstate  $|\chi\rangle$ , and also introduce an orthogonal state  $|\perp_{\chi}\rangle = \frac{1}{\sqrt{1-\chi^2}}(\text{SELECT} - \chi I)|\mathcal{L}\rangle|\chi\rangle$  so that

$$\text{SELECT}|\mathcal{L}\rangle|\chi\rangle = \chi|\mathcal{L}\rangle|\chi\rangle + \sqrt{1-\chi^2}|\perp_{\chi}\rangle. \quad (\text{S23})$$

We say that the oracles are qubitized if the action of the **SELECT** is closed within the two-dimensional subspace  $\mathcal{H}_{\chi} = \text{Span}(|\mathcal{L}\rangle|\chi\rangle, |\perp_{\chi}\rangle)$ , which is known to be satisfied if and only if  $\langle \mathcal{L} | \text{SELECT}^2 | \mathcal{L} \rangle = I$  [52]. Observe that **SELECT** defined as Eq. (S22) satisfies this condition;  $A$  is now Hermitian and hence can be decomposed as  $A = \sum_l w_l A_l$  with  $w_l > 0$  and  $A_l^2 = I$ . Meanwhile, this does not hold if  $A$  is not Hermitian (as in the case of truncated Taylor series of unitary time evolution operator). We find that other transition amplitudes can be computed explicitly as

$$\langle \mathcal{L} | \langle \chi | \text{SELECT} | \perp_{\chi} \rangle = \langle \mathcal{L} | \langle \chi | \text{SELECT}(\text{SELECT} - \chi I) | \mathcal{L} \rangle | \chi \rangle / \sqrt{1-\chi^2} \quad (\text{S24})$$

$$= \frac{1-\chi^2}{\sqrt{1-\chi^2}} = \sqrt{1-\chi^2}, \quad (\text{S25})$$

$$\langle \perp_{\chi} | \text{SELECT} | \perp_{\chi} \rangle = \langle \mathcal{L} | \langle \chi | (\text{SELECT} - \chi I) \text{SELECT} (\text{SELECT} - \chi I) | \mathcal{L} \rangle | \chi \rangle / (1-\chi^2) \quad (\text{S26})$$

$$= \langle \mathcal{L} | \langle \chi | (\text{SELECT} - 2\chi I + \chi^2 \text{SELECT}) | \mathcal{L} \rangle | \chi \rangle / (1-\chi^2) \quad (\text{S27})$$

$$= \frac{-\chi(1-\chi^2)}{1-\chi^2} = -\chi, \quad (\text{S28})$$

and therefore the action within the effective Hilbert space  $\mathcal{H}_{\chi}$  is given as follows:

$$\text{SELECT}_{\chi} = \begin{pmatrix} \chi & \sqrt{1-\chi^2} \\ \sqrt{1-\chi^2} & -\chi \end{pmatrix}. \quad (\text{S29})$$

Observe that the action satisfies  $\text{SELECT}_{\chi} \text{SELECT}_{\chi}^{\dagger} = I$  and indeed closed within the subspace.

The framework of the qubitization enables one to perform a vast class of polynomial transformation on the eigen-spectrum of  $A$  as  $\text{Poly}(A)$ . This implies that, one can build up a new block encoding of an operator from an existing block encoded operator, just as one develops a new algorithm by combining subroutines [76]. For instance, given a block encoding of  $A$ , one may construct a block encoding of polynomial approximation for  $e^{iA}$ , from which one may also derive a block encoding of  $A^{-1}$ . Such a methodology to manipulate eigenvalues enable one to extract various information from the block encoded operator.

Now we have confirmed that the oracles defined as in Eqs. (S20), (S22) are readily qubitized. Let us next proceed to construct a Szegedy-type walk operator as  $\mathcal{W} = \mathcal{R}_{\mathcal{L}} \cdot \text{SELECT}$ , which combines **SELECT** with another reflection operator defined as  $\mathcal{R}_{\mathcal{L}} = 2|\mathcal{L}\rangle \langle \mathcal{L}| - I$ . It is straightforward to find that  $\mathcal{W}$  is also qubitized in each two-dimensional subspace  $\mathcal{H}_k$  which is defined from the  $k$ -th eigenstate of the Hamiltonian:

$$\mathcal{W}_k = \begin{pmatrix} E_k/\lambda & \sqrt{1-(E_k/\lambda)^2} \\ -\sqrt{1-(E_k/\lambda)^2} & E_k/\lambda \end{pmatrix} = e^{i \arccos(E_k/\lambda)Y}, \quad (\text{S30})$$

where  $E_k$  denotes the  $k$ -th eigenenergy. Therefore, this walk operator not only block-encodes the Hamiltonian in the signal space as  $\langle \mathcal{L} | \mathcal{W} | \mathcal{L} \rangle = e^{i \arccos(H/\lambda)}$ , but also provides efficient access to its entire eigenspectra.

Using the oracles **PREPARE** and **SELECT** introduced above, we construct the entire circuit as shown in Fig. S8, where we have also introduced the preparation circuit for the readout qubits as [75]

$$\chi_m |0\rangle^m = \sqrt{\frac{2}{2^m+1}} \sum_{i=0}^{2^m-1} \sin\left(\frac{\pi(i+1)}{2^m+1}\right) |i\rangle. \quad (\text{S31})$$

This consumes  $T$ -gates of  $\tilde{O}(m)$  and hence neglected in the resource analysis in the present work. It is crucial to the resource estimate that the number of readout digits  $m$  is determined from the number of repetition  $r$  regarding the the quantum walk operations as [17, 18, 77]

$$r = \left\lceil \frac{\pi\lambda}{2\epsilon} \right\rceil < 2^m. \quad (\text{S32})$$

This leads us to obtain the relation between the cost (i.e.,  $T$ -count or detailed runtime) of the global algorithm and the oracles as

$$C_{\text{HS}} \sim r \times (C_{\text{P}} + C_{\text{P}^{\dagger}} + C_{\text{S}}), \quad (\text{S33})$$

where  $C_{\text{P}(\dagger)}$  and  $C_{\text{S}}$  denotes the cost required for the **PREPARE** and **SELECT** oracles, respectively.

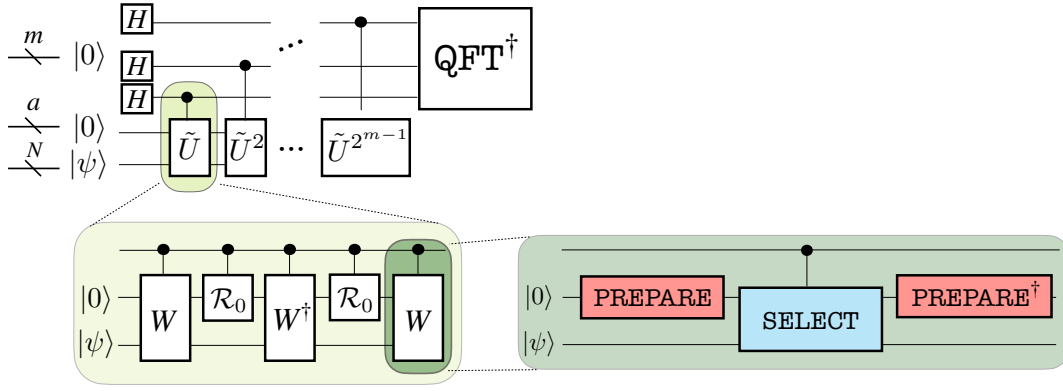


FIG. S9. Quantum circuit structure of Taylorization-based phase estimation algorithm. The definitions of **PREPARE** and **SELECT** are given in Eqs. (S20), (S22), where the target operator is taken as the truncated Taylor series of the time evolution unitary.

### 3. Taylorization

Taylorization is one of the earliest attempts to overcome the polynomial gate complexity  $\text{Poly}(1/\epsilon_{\text{HS}})$  in Trotter-based Hamiltonian simulation methods [73, 74]. In essence, the algorithm uses the technique of block encoding to approximate the time evolution operator  $U = \exp(-iHt)$  with the repetitive operation of truncated Taylor series up to  $K$ -th order (See Fig. S9), which results in  $\text{polylog}(1/\epsilon_{\text{HS}})$  gate complexity. To be concrete, the time evolution is divided into  $r$  steps as  $U = (U_r)^r$  with  $U_r = \exp(-iHt/r)$ , where each step is approximated as

$$\tilde{U}_r := \sum_{k=0}^K \frac{(-iHt/r)^k}{k!} H^k = \sum_{k=0}^K \sum_{l_1, \dots, l_K} w_{l_1} \cdots w_{l_K} A_{l_1} \cdots A_{l_K}. \quad (\text{S34})$$

Hyperparameters such as  $K$  and  $r$  shall be chosen in order to predict the output energy with target precision  $\epsilon$ . Here, we regard the error as accumulation of error from finite-digit truncation in phase estimation  $\epsilon_{PE}$  and Trotter error of the Hamiltonian simulation  $\epsilon_{HS}$ , and in particular focus on the case with  $\epsilon_{PE} = \frac{2}{3}\epsilon$  and  $\epsilon_{HS} = \frac{1}{3}\epsilon$ . Following the discussion of the qubitization and also Ref. [50, 78], we take

$$r = \frac{\pi\lambda}{2\epsilon_{PE}}, \quad K = \left\lceil -1 + \frac{2 \log(2r/\epsilon_{\text{HS}})}{\log \log(2r/\epsilon_{\text{HS}}) + 1} \right\rceil, \quad (\text{S35})$$

where  $\lambda = \sum_l w_l$  is the total sum of coefficients of the Hamiltonian.

Once we construct **PREPARE** and **SELECT** for truncated Taylor series Eq. (S34), we find that the block encoding is realized via a walk operator

$$W := (\text{PREPARE}^\dagger)(\text{SELECT})(\text{PREPARE}), \quad (\text{S36})$$

whose explicit operation is given using  $s = \sum_{k=0}^K \sum_{l_1, \dots, l_K} w_{l_1} \cdots w_{l_K}$  as

$$W |0\rangle |\psi\rangle = \frac{1}{s} |0\rangle \tilde{U}_r |\psi\rangle + \sqrt{1 - \frac{1}{s^2}} |\perp\rangle. \quad (\text{S37})$$

Although the unwanted second term seem to deteriorate the simulation, we may tune the amplitude of the target state via the oblivious amplitude estimation introduced in [49]. Namely, we rescale the time evolution as  $s = 2$  so that the combination of the walk operator and a reflection operator on the ancillary qubits  $\mathcal{R}_0 = I - 2|0\rangle\langle 0|$  gives [50]

$$W \mathcal{R}_0 W^\dagger \mathcal{R}_0 W |0\rangle |\psi\rangle = -|0\rangle \tilde{U} |\psi\rangle. \quad (\text{S38})$$

Finally, by plugging the controlled operation of  $\tilde{U}$  into the quantum circuit of phase estimation as in Fig. S7, we obtain the circuit structure of the entire algorithm as in Fig. S9. The overall cost is given as follows,

$$C_{\text{HS}} \sim r \times (3(C_P + C_{P^\dagger} + C_S) + 2C_{\mathcal{R}_0}), \quad (\text{S39})$$

where  $C_P$  and  $C_S$  is obtained from  $K$ -fold multiplication on cost for the qubitization algorithm, while  $C_{\mathcal{R}_0}$  is simply the cost for multi-controlled Z-gate operated on ancillas.



#### S4. POST-TROTTER ORACLES FOR LATTICE MODELS

In Sec. S3 D, we have introduced the technique of block encoding, which allows us to perform Hamiltonian simulation with gate complexity that scales polylogarithmically with respect to the target accuracy  $\epsilon_{\text{HS}}$ . In this section, we further provide the explicit construction of quantum circuits that cover a broad range of lattice models considered in condensed matter physics. We introduce two methods to construct oracles, which we refer to as sequential and product-wise constructions. Abstract descriptions are provided each for **PREPARE** and **SELECT** oracles in Secs. S4 A and S4 B, respectively. Subsequently we give constructions for quantum spin models and fermionic models whose interaction is geometrically local and translationally invariant. Then, we proceed to show examples in concrete models: spin-1/2  $J_1$ - $J_2$  Heisenberg model and Fermi-Hubbard model on the square lattice, and also the spin-1 Heisenberg chain. From the results of  $T$ -count analysis combined with that for Trotter-based methods presented in Sec. S3 C, we compare the order of computational cost between various phase estimation subroutines to conclude that the qubitization algorithm gives the best practice among the Hamiltonian simulation subroutines. We further guide readers to Sec. S7 for more detailed runtime analysis that compiles quantum circuit of the qubitization algorithm into executable instructions. We importantly remark that we have chosen the product-wise construction to compare  $T$ -counts between Hamiltonian simulation subroutines, while for the runtime analysis we focus on the sequential type of **SELECT** oracle for the sake of simplicity.

##### A. Abstract structure of PREPARE

Here, we present the abstract structure of **PREPARE** circuit that achieves polylogarithmic cost, in terms of both  $T$ -count and ancillary qubit count, for translationally-invariant  $G$ -local Hamiltonians introduced in Sec. S1 as

$$H = \sum_{\mathbf{p}} \sum_{\{\boldsymbol{\mu}, \boldsymbol{\alpha}\}} w_{\boldsymbol{\mu}, \boldsymbol{\alpha}} \hat{\Lambda}_{\mathbf{p}}^{(\alpha_1)} \hat{\Lambda}_{\mathbf{p}+\boldsymbol{\mu}_1}^{(\alpha_2)} \cdots \hat{\Lambda}_{\mathbf{p}+\boldsymbol{\mu}_{G-1}}^{(\alpha_G)}, \quad (\text{S40})$$

where  $\mathbf{p} = (p_1, \dots, p_d)$  labels the site (including the sublattice structure),  $\boldsymbol{\mu} = (\boldsymbol{\mu}_1, \dots, \boldsymbol{\mu}_{G-1})$  is a set of vectors that identifies the connection between interacting sites,  $\hat{\Lambda}_{\mathbf{p}}^{\boldsymbol{\alpha}}$  is an operator for microscopic degrees of freedom (e.g. spin, fermion, boson) on site  $\mathbf{p}$ , and  $w_{\boldsymbol{\mu}, \boldsymbol{\alpha}}$  is the amplitude of the interaction. As we display in Fig. S10, both the **PREPARE** for qubitization and Taylorization consist of the identical subroutine which we call in this paper as **UNIT-PREP**. Therefore, let us first focus on the case of qubitization and later mention the case of Taylorization.

First we introduce the sequential construction, which straightforwardly encodes all the information of coefficients as

$$\text{UNIT-PREP} : |0\rangle \mapsto |\mathcal{L}\rangle = \sum_{\mathbf{p}} \sum_{\{\boldsymbol{\mu}, \boldsymbol{\alpha}\}} \sqrt{\frac{w_{\boldsymbol{\mu}, \boldsymbol{\alpha}}}{\lambda}} |\mathbf{p}\rangle |\boldsymbol{\mu}, \boldsymbol{\alpha}\rangle. \quad (\text{S41})$$

Thanks to the translational invariance of the Hamiltonian, we may split the ancilla for geometrical position  $\mathbf{p}$  and interaction configurations  $\boldsymbol{\mu}, \boldsymbol{\alpha}$ . Note that in the graphical description in Fig. S11(a) we have introduced  $\text{UNIFORM}_N |0\rangle = \frac{1}{\sqrt{N}} \sum_{n=1}^N |n\rangle$ .

One evident difference between the product-wise construction from the sequential one is the  $G$ -fold increase in use of ancilla qubits, from which we benefit in terms of  $T$ -count in **SELECT** oracle (See. S4 B). The general form of product-wise **UNIT-PREP** encodes the interaction amplitudes into ancillary qubits as follows:

$$\text{UNIT-PREP} : |0\rangle \mapsto |\mathcal{L}\rangle = \sum_{\mathbf{p}} \sum_{\{\boldsymbol{\mu}, \boldsymbol{\alpha}\}} \sqrt{\frac{w_{\boldsymbol{\mu}, \boldsymbol{\alpha}}}{\lambda}} |\mathbf{p}, \mathbf{p} + \boldsymbol{\mu}_1, \dots, \mathbf{p} + \boldsymbol{\mu}_{G-1}\rangle |\boldsymbol{\mu}, \boldsymbol{\alpha}\rangle. \quad (\text{S42})$$

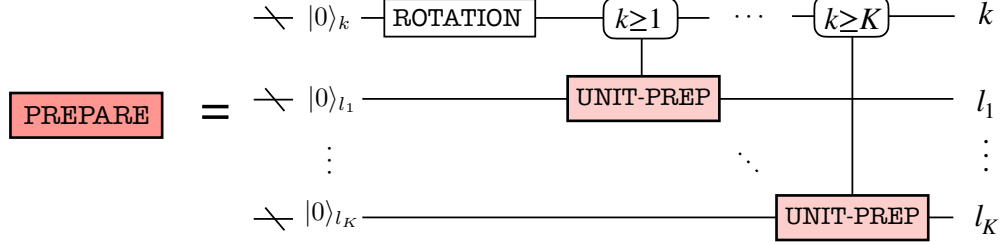
As shown in Fig. S11(b), this can roughly be decomposed into three steps as

$$\begin{aligned} |0\rangle &\xrightarrow{\text{Rotations}} \left( \sum_{\mathbf{p}} |\mathbf{p}\rangle |0\rangle^{(G-1) \log N} \right) \otimes \left( \sum_{\{\boldsymbol{\mu}, \boldsymbol{\alpha}\}} \sqrt{w_{\boldsymbol{\mu}, \boldsymbol{\alpha}}} |\boldsymbol{\mu}, \boldsymbol{\alpha}\rangle \right) = \sum_{\mathbf{p}} \sum_{\{\boldsymbol{\mu}, \boldsymbol{\alpha}\}} \sqrt{w_{\boldsymbol{\mu}, \boldsymbol{\alpha}}} |\mathbf{p}\rangle |0\rangle^{(G-1) \log N} |\boldsymbol{\mu}, \boldsymbol{\alpha}\rangle \\ &\xrightarrow{\text{COPY\_INDEX}} \sum_{\mathbf{p}} \sum_{\{\boldsymbol{\mu}, \boldsymbol{\alpha}\}} \sqrt{w_{\boldsymbol{\mu}, \boldsymbol{\alpha}}} |\mathbf{p}, \mathbf{p}, \dots, \mathbf{p}\rangle |\boldsymbol{\mu}, \boldsymbol{\alpha}\rangle \\ &\xrightarrow{\text{SHIFT\_INDEX}} \sum_{\mathbf{p}} \sum_{\{\boldsymbol{\mu}, \boldsymbol{\alpha}\}} \sqrt{\frac{w_{\boldsymbol{\mu}, \boldsymbol{\alpha}}}{\lambda}} |\mathbf{p}, \mathbf{p} + \boldsymbol{\mu}_1, \dots, \mathbf{p} + \boldsymbol{\mu}_{G-1}\rangle |\boldsymbol{\mu}, \boldsymbol{\alpha}\rangle (= |\mathcal{L}\rangle), \end{aligned} \quad (\text{S43})$$

(a)

$$\boxed{\text{PREPARE}} = \boxed{\text{UNIT-PREP}}$$

(b)



(c)

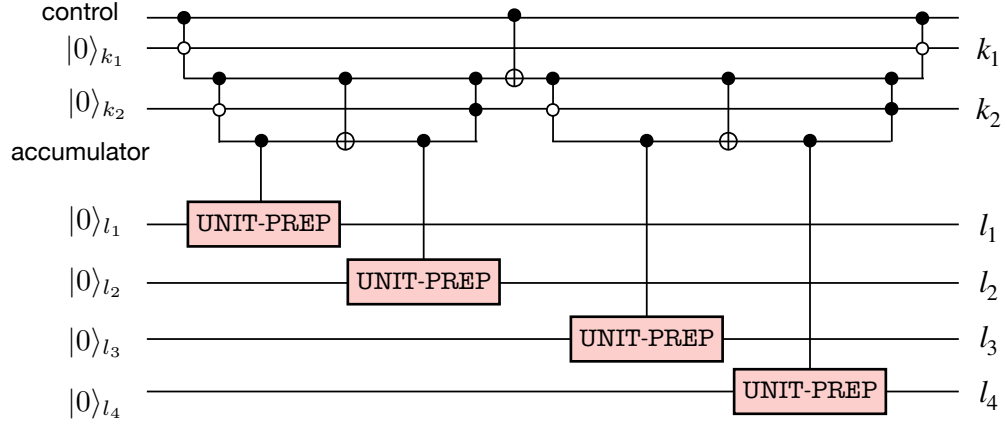


FIG. S10. **PREPARE** structure of (a) qubitization and (b) Taylorization, whose detailed circuit structure for  $K = 4$  case is described in (c).

where  $N$  is the total system size. Note that we have abbreviated overall coefficients in the first and second lines for the sake of simplicity.

The main resource of  $T$ -count is the Solovay-Kitaev decomposition of the rotation gates in the first step, and the adder circuit for **COPY\_INDEX** and **SHIFT\_INDEX**. Regarding the dynamics simulation error  $\epsilon_{\text{HS}}$ , the order of the  $T$ -count can be obtained as  $\mathcal{O}(\log N/\epsilon_{\text{HS}})$  where the required number of ancillary qubits can be estimated as  $(G + 1) \log N + \log N_{\alpha, \mu} + \mathcal{O}(1)$ , with  $N_{\alpha, \mu} = N_{\alpha} N_{\mu}$  denoting the total number of combinations of  $(\alpha, \mu)$ . Here, we assume to use the efficient implementation of logical adder that use auxiliary qubits to store the information of “carry-on” [79], resulting in additional use of ancillary qubits of  $\log N_{\alpha, \mu}$ . Note that, for the **PREPARE** circuit for Taylorization, we prepare  $N_{\alpha, \mu} \log L + \log N_{\alpha, \mu}$  ancilla qubits to encode information on higher order contribution from Taylor expansion, as can be seen from Fig. S10.

Last but not least, let us mention how to deal with the boundary condition. Be aware that the above-mentioned construction assumes translationally invariant Hamiltonian defined under the periodic boundary condition. However, of course we are not limited to this situation: open, cylinder, or twisted boundary conditions can also be readily treated as well. One straightforward way is to encode the boundary terms individually, which can be done by sparing  $T$ -count of  $\log(N^{d-1/d})$ . However, in this work we consider an alternative method to simulate Hamiltonians defined on cylindrical boundary condition which solely relies on simple postprocessing and rescaling of the Hamiltonian. The details are explained in Sec. S6.

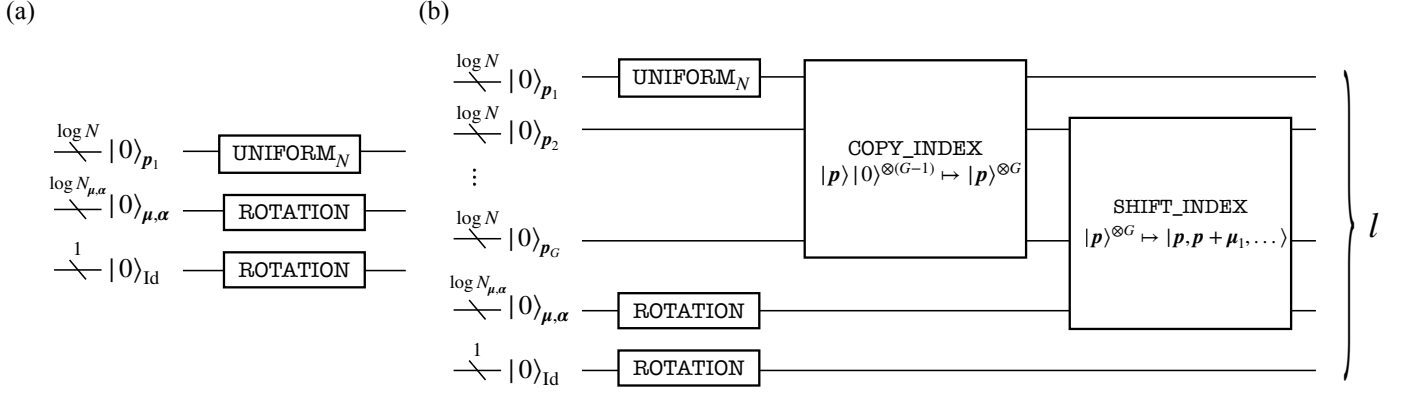


FIG. S11. General structure of **PREPARE** for lattice systems with  $G$ -local translationally invariant interactions. (a) Circuit structure of the common subroutine named **UNIT-PREP**. This is identical to **PREPARE** in the case of qubitization.

### B. Abstract structure of SELECT

Next, we present the sequential and product-wise structure of **SELECT** oracles that are used to block-encode an operator  $H = \sum_{l=1}^L w_l H_l$ . In the sequential construction, we perform one-hot encoding of individual unitary  $H_l$  as defined in Eq. (S22) as

$$\text{SELECT} = \sum_l |l\rangle \langle l| \otimes H_l + \sum_{\bar{l}} |\bar{l}\rangle \langle \bar{l}| \otimes I. \quad (\text{S44})$$

In particular, we assume that every  $H_l$  is a tensor product of Pauli operators (with global phase  $\pm i$  or  $\pm 1$ ) so that we can implement  $H_l$  and controlled  $H_l$  with Clifford operations. Babbush *et al.* has proposed a quantum circuit that realizes Eq. (S44) with  $T$ -count of  $4L - 4$  [75], whose structure is explicitly shown in Fig. S12(a).

While Fig. S12(a) is applicable to general form of Hamiltonian, we find that in many cases the translational symmetry allows even more efficient implementation via product-wise construction. For instance, let us consider quantum spin models whose Hamiltonian is expressed in terms of spin- $S$  operators with maximum  $G$ -local terms as

$$H = \sum_{\mathbf{p}} \sum_{\{\mu, \alpha\}} w_{\mu, \alpha} S_{\mathbf{p}}^{(\alpha_1)} S_{\mathbf{p}+\mu_1}^{(\alpha_2)} \cdots S_{\mathbf{p}+\mu_{G-1}}^{(\alpha_G)}. \quad (\text{S45})$$

Here, we find that the quantum circuit depicted in Fig. S12(b) enables us to implement **SELECT** with  $T$ -count of  $8GSN_{\alpha}N_{\text{site}} - 4$ , where  $N_{\text{site}}$  is the total number of sites. For instructive purpose, we mention that,  $(G, N_{\alpha}) = (2, 3)$  for arbitrary Heisenberg Hamiltonians, while  $(G, N_{\alpha}) = (4, 2)$  for the surface code Hamiltonian. Note that the product-wise construction covers the entire  $G$ -site connectivity, and therefore does not depend on the lattice geometry. More explicitly, observe that we do not see any dependence on  $N_{\mu}$ .

The difference of two implementations is highlighted in densely coupled situations due to, e.g., high dimensionality or long-range interaction. For instance, let us consider a spin- $S$  Heisenberg model on  $d$ -dimensional hypercube with  $r$ -nearest-neighbor interaction, each site of which is coupled to  $\gamma_{r,d}$  sites. Under such a procedure, the number of Pauli operator is given as

$$L = 3 \times (2S)^2 \times \frac{\gamma_{r,d}}{2} \times N_{\text{site}}. \quad (\text{S46})$$

Meanwhile, as we show in Table S6, the product-wise construction of **SELECT** is not affected by the connectivity of the interaction profile; this gives improvement for arbitrary interaction profile except for the case of spin-1/2 1d nearest-neighbor interaction.

Let us remark briefly on the estimation of the actual runtime. While we may use  $T$ -counts as the baseline to compare the performance between different Hamiltonian simulation algorithms, we further discuss in Sec. S7 that the actual runtime (which is more related with the  $T$ -depth) can be further improved by distributed implementation of the controlled  $H_l$  operation.

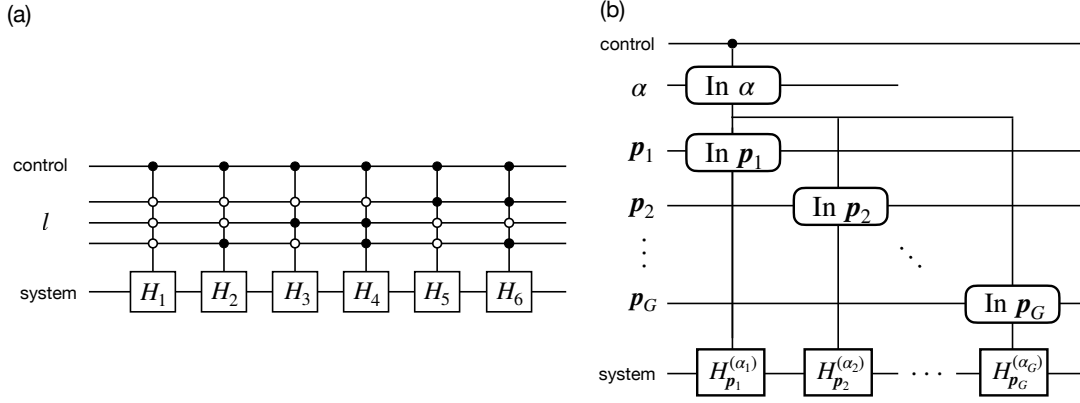


FIG. S12. General quantum circuit structure of **SELECT** oracle. (a) Sequential structure based on the unary encoding of efficiently-implementable unitaries. Here we assume that the Hamiltonian is a sum over  $L = 6$  Pauli terms. (b) Product-wise structure exploiting the  $G$ -local translational symmetric structure of Hamiltonian.

SELECT type	General $T$ -count	Heisenberg chain	2d $J_1$ - $J_2$ Heisenberg	3d $J_1$ - $J_2$ - $J_3$ Heisenberg	General lattice Heisenberg ( $r, d, S$ )
Sequential	$4L - 4$	$48S^2N_{\text{site}} - 4$	$192S^2N_{\text{site}} - 4$	$624S^2N_{\text{site}} - 4$	$24S^2\gamma_{r,d}N_{\text{site}} - 4$
Product-wise	$8SGN_{\alpha}N_{\text{site}} - 4$	$48SN_{\text{site}} - 4$	$48SN_{\text{site}} - 4$	$48SN_{\text{site}} - 4$	$48SN_{\text{site}} - 4$

TABLE S6.  $T$ -count of **SELECT** for spin- $S$  Heisenberg model on  $d$ -dimensional hypercube with  $r$ -nearest-neighbor interactions. Here, we denote the number of edges per site as  $\gamma_{r,d}$  and the total number of sites as  $N_{\text{site}}$ . To be concrete, Heisenberg chain satisfies  $(r, d) = (1, 1)$  with  $\gamma_{r,d} = 2$ , 2d  $J_1$ - $J_2$  Heisenberg corresponds to  $(r, d) = (2, 2)$  with  $\gamma_{r,d} = 8$ , where 3d  $J_1$ - $J_2$ - $J_3$  Heisenberg model is described by  $(r, d) = (3, 3)$  with  $\gamma_{r,d} = 26$ .

### C. Explicit construction of oracles

We are now ready to dive into the explicit construction of quantum circuits for executing post-Trotter methods. Since it is straightforward to modify the circuits generated for qubitization into those for Taylorization, we exclusively discuss the oracles for qubitization.

#### 1. 2d $J_1J_2$ Heisenberg model

The Hamiltonian of spin-1/2  $J_1$ - $J_2$  Heisenberg model on the square lattice is defined as in Eq. S2 as

$$H = J_1 \sum_{\langle p, q \rangle} \sum_{\alpha \in \{X, Y, Z\}} S_p^\alpha S_q^\alpha + J_2 \sum_{\langle\langle i, j \rangle\rangle} \sum_{\alpha \in \{X, Y, Z\}} S_p^\alpha S_q^\alpha, \quad (\text{S47})$$

where the summation of the first and second terms concerns nearest-neighbor and next-nearest-neighbor sites, respectively, and  $S_p^\alpha$  is now the spin-1/2 operator. Here we exclusively consider a square lattice of  $N = M \times M$  sites, and focus on the model with  $J_1 = 1, J_2 = 0.5$  where quantum spin liquid phase is expected to show up.

First, let us briefly introduce the sequential construction of **UNIT-PREP** oracle. The circuit structure shown in Fig. S13(a) realizes the following action:

$$\text{UNIT-PREP} |0\rangle \mapsto \sum_p \sum_{\alpha \in \{X, Y, Z\}} \sum_{\mu=1,2} \sqrt{\frac{J_1}{\lambda}} |p\rangle |\alpha\rangle |\mu\rangle + \sum_{\mu=3,4} \sqrt{\frac{J_2}{\lambda}} |p\rangle |\alpha\rangle |\mu\rangle, \quad (\text{S48})$$

where  $\mu \in \{1, 2, 3, 4\}$  correspond to the coupling between  $(p_x, p_y)$  and  $(p_x + 1, p_y), (p_x, p_y + 1), (p_x + 1, p_y + 1), (p_x - 1, p_y + 1)$ , respectively.

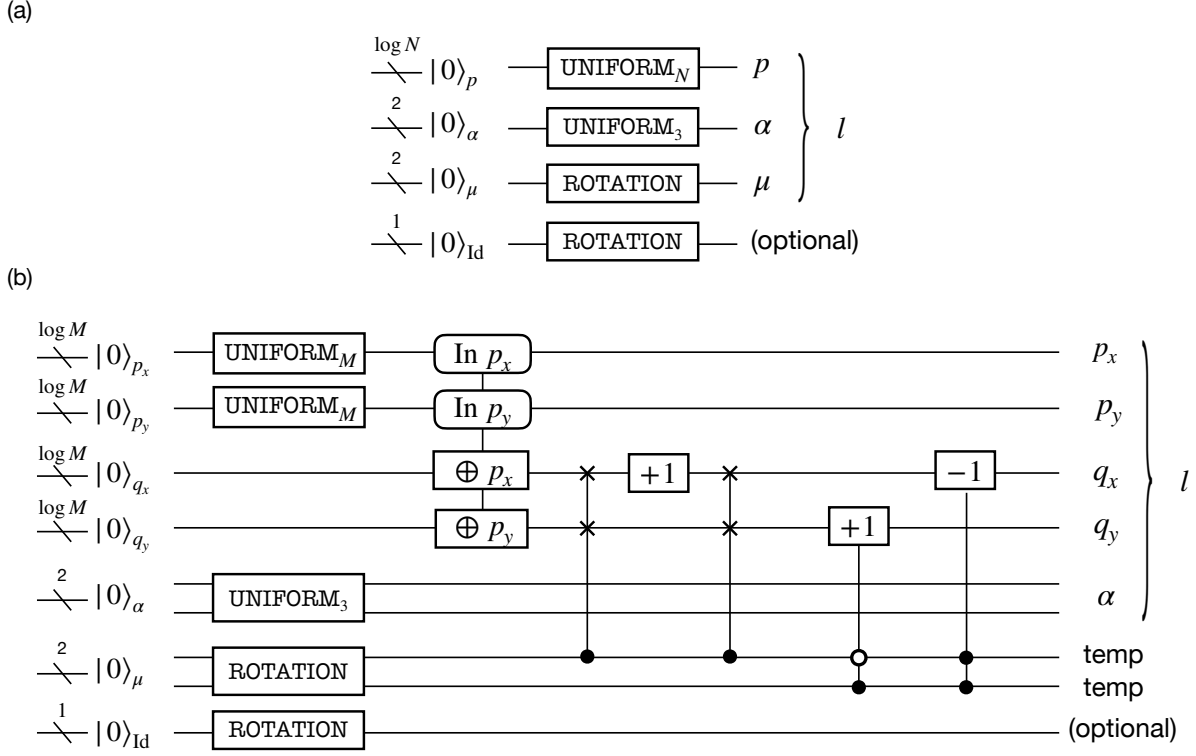


FIG. S13. Circuit structure of UNIT-PREP for spin-1/2  $J_1$ - $J_2$  Heisenberg model on square lattice. (a) The sequential construction requires  $T$ -count of  $8 \log N + 32 \log(1/\epsilon_{SS})$  and the  $\log N + O(1)$  ancilla qubits, where (b) product-wise construction consumes  $T$ -count of  $20 \log N + 44 \log(1/\epsilon_{SS})$  and spans  $3 \log N + 5$  ancillary qubits. Note that we have introduced  $M^2 = N$  in the figure.

On the other hand, for product-wise construction, UNIT-PREP circuit is designed to generate the following state:

$$\begin{aligned}
 \text{UNIT-PREP } |0\rangle \mapsto & \sum_{p_x, p_y} \sum_{\alpha \in \{X, Y, Z\}} \sqrt{\frac{J_1}{\lambda}} |p_x, p_y\rangle |p_x + 1, p_y\rangle |\alpha\rangle \\
 & + \sqrt{\frac{J_1}{\lambda}} |p_x, p_y\rangle |p_x, p_y + 1\rangle |\alpha\rangle \\
 & + \sqrt{\frac{J_2}{\lambda}} |p_x, p_y\rangle |p_x + 1, p_y + 1\rangle |\alpha\rangle \\
 & + \sqrt{\frac{J_2}{\lambda}} |p_x, p_y\rangle |p_x - 1, p_y + 1\rangle |\alpha\rangle,
 \end{aligned} \tag{S49}$$

whose graphical description is shown in Fig. S13(b). Note that, the required number of ancillary qubits is  $3 \log N + O(1)$  rather than  $2 \log N + O(1)$  that is obtained by simply adding up the numbers in Fig. S13(b). This is because the most efficient implementation of adders (in terms of  $T$ -count) require as many quantum registers as the number of qubits to be simulated [79]. Furthermore, by counting the number of required  $T$ -gates using the table presented in Sec. S5, we find that the UNIT-PREP can be implemented with  $T$ -count of  $20 \log N + 48 \log(1/\epsilon_{SS})$ .

As for the SELECT oracle, we follow the framework presented in Sec. S4B for sequential construction. Meanwhile, if we use the product-wise SELECT oracle, the operation on computational bases that are not included in the signal state also becomes nontrivial, while this does not affect the dynamics encoded in the signal state. In this case, the  $T$ -count becomes  $24N - 4$ , which is approximately halved compared to the vanilla sequential type of SELECT oracle.



## 2. 2d Fermi-Hubbard model

The Hamiltonian of Fermi-Hubbard model on the square lattice reads as defined in Sec. S1 as

$$H = -t \sum_{\langle p,q \rangle, s} (c_{p,\sigma}^\dagger c_{q,s} + \text{h.c.}) + U \sum_p n_{p,\uparrow} n_{p,\downarrow}, \quad (\text{S50})$$

where  $c_{p,\sigma}^{(\dagger)}$  is the fermionic annihilation (creation) operator on site  $p$  with spin  $\sigma \in \{\uparrow, \downarrow\}$ ,  $n_{p,\sigma} = c_{p,\sigma}^\dagger c_{p,\sigma}$  is the corresponding number operator,  $t$  is the hopping amplitude, and  $U$  is the repulsive onsite potential. As in the case for spin-1/2  $J_1$ - $J_2$  Heisenberg model, we mainly consider the lattice of  $M \times M$  sites, and thus the total number of qubits required to simulate the system is  $N = 2M^2$ . While we take  $t$  to be unity in this work, we explicitly keep it among expressions when it is more informative.

For concreteness, we assume to employ the Jordan-Wigner transformation to encode fermionic degrees of freedom into quantum computer:

$$c_{p,s}^{(\dagger)} = \text{sgn}(s) \prod_{r < p} \prod_{s=\uparrow, \downarrow} \sigma_{r,s}^{+(-)} \quad (\text{S51})$$

where  $p = p_x + p_y M$  and  $\text{sgn}(s)$  takes  $\pm 1$  according to whether the spin is up or down. This leads us to the expression of Hamiltonian as follows,

$$H = -\frac{t}{2} \sum_{\langle p,q \rangle, s} (\sigma_{p,s}^X \sigma_{q,s}^Z \sigma_{q,s}^X + \sigma_{p,s}^Y \sigma_{q,s}^Z \sigma_{q,s}^Y) + \frac{U}{8} \sum_p \sigma_{p,\uparrow} \sigma_{p,\downarrow} - \frac{U}{4} \sum_{p,s} \sigma_{p,s}^Z + \frac{UN}{4} I, \quad (\text{S52})$$

where we have introduced  $\sigma^Z$  to represent the Z-string generated by Jordan-Wigner transformation.

In similar to the case with 2d  $J_1$ - $J_2$  Heisenberg model, we first introduce the sequential construction of UNIT-PREP. Our construction simply aims to generate

$$\begin{aligned} \text{UNIT-PREP } |0\rangle \mapsto & \sum_{p_x, p_y} \left[ \sqrt{\frac{U}{8\lambda}} |p, \uparrow\rangle |\text{onsite interaction}\rangle_{\alpha, \mu} + \sum_{s=\uparrow, \downarrow} \sqrt{\frac{U}{4\lambda}} |p, s\rangle |\text{potential}\rangle_{\alpha, \mu} \right. \\ & \left. + \sum_{s=\uparrow, \downarrow} \sum_{\mu=e_x, e_y, e_{-x}, e_{-y}} \sqrt{\frac{t}{2\lambda}} |p, s\rangle |\text{hopping towards } \mu\rangle_{\alpha, \mu} \right], \end{aligned} \quad (\text{S53})$$

which is realized by circuit shown in Fig. S14(a). Note that the ancillary quantum states such as  $|\text{onsite interaction}\rangle$  functions as “flag” to tell the **SELECT** oracle which interaction term must be operated.

By carefully examining the coefficients and the commutation relation, we find out that UNIT-PREP presented in Fig. S14(b) provides the the product-wise construction via the following operation:

$$\begin{aligned} \text{UNIT-PREP } |0\rangle \mapsto & \sum_{p_x, p_y} \left[ \sqrt{\frac{U}{8\lambda}} |p_x, p_y, \uparrow\rangle |p_x, p_y, \downarrow\rangle |0, 1\rangle_\alpha \right. \\ & + \sum_{s=\uparrow, \downarrow} \sqrt{\frac{U}{4\lambda}} |p_x, p_y, s\rangle |p_x, p_y, s\rangle |1, 0\rangle_\alpha \\ & + \sum_{s=\uparrow, \downarrow} \sqrt{\frac{t}{2\lambda}} \left( |p_x, p_y, s\rangle |p_x + 1, p_y, s\rangle |0, 0\rangle_\alpha + |p_x, p_y, s\rangle |p_x, p_y + 1, s\rangle |0, 0\rangle_\alpha \right) \\ & \left. + \sum_{s=\uparrow, \downarrow} \sqrt{\frac{t}{2\lambda}} \left( |p_x, p_y, s\rangle |p_x - 1, p_y, s\rangle |0, 0\rangle_\alpha + |p_x, p_y, s\rangle |p_x, p_y - 1, s\rangle |0, 0\rangle_\alpha \right) \right], \end{aligned} \quad (\text{S54})$$

where  $\alpha$  specifies the type of interaction term.

Now we proceed to the operation of **SELECT**. We remark that the sequential construction is straightforward, and can be done by following the procedure explained as in Fig. S12(a). In contrast, the product-wise construction of

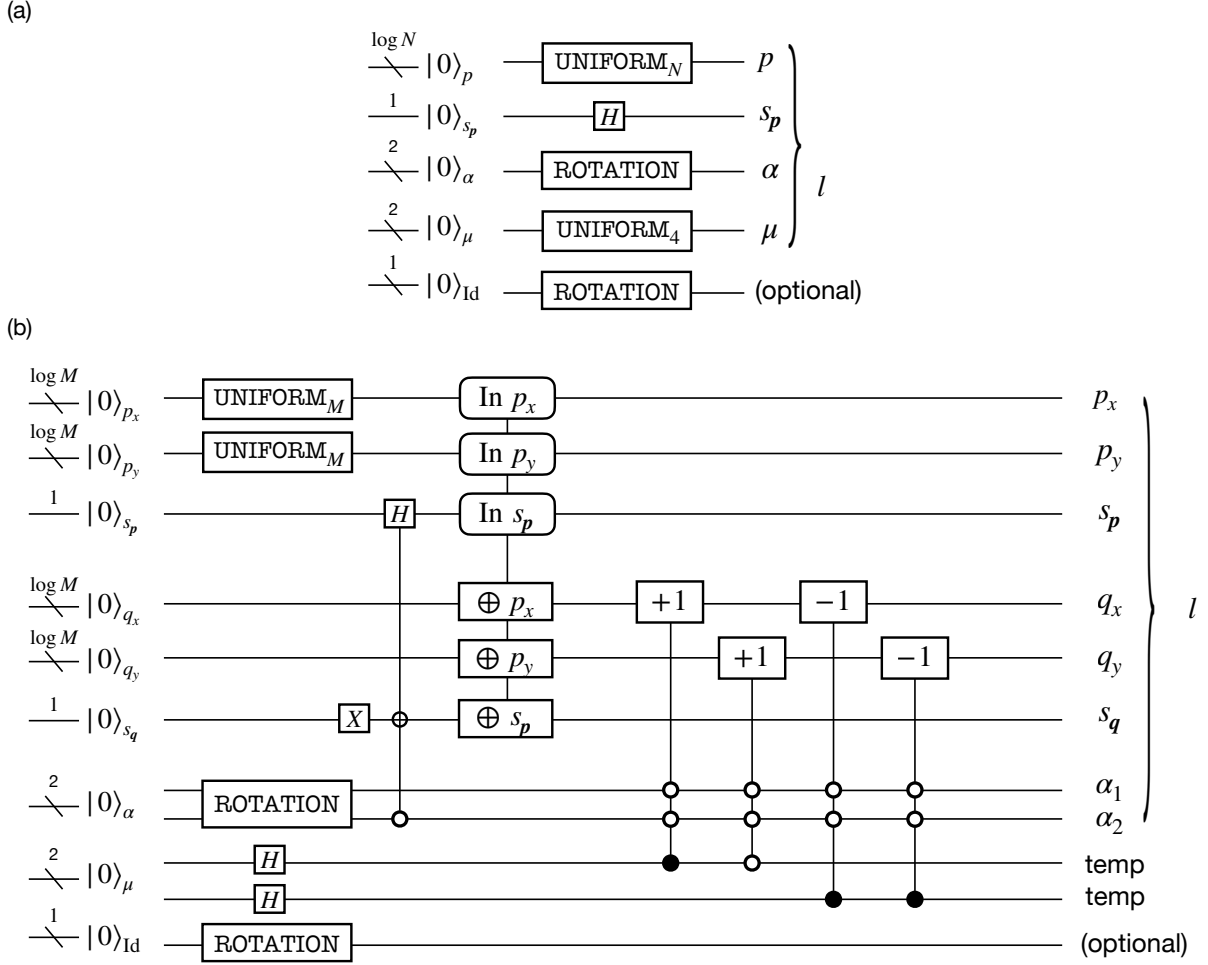


FIG. S14. Circuit structure of UNIT-PREP for 2d Fermion Hubbard model on square lattice. (a) Sequential construction requires  $T$ -count of  $8 \log N + 32 \log(1/\epsilon_{SS})$  with  $\log N + O(1)$  ancilla qubits, while (b) product-wise construction consumes  $T$ -count of  $28 \log N + 32 \log(1/\epsilon_{SS})$  and  $3 \log N + O(1)$  ancilla qubits. The construction of **SHIFT\_INDEX** is slightly more efficient than the one presented in Ref. [75]; the required number of  $T$ -gates is reduced from  $32 \log N$  to  $28 \log N$ . However, the dominant factor is the **SELECT** circuit that consumes  $T$ -count of  $\mathcal{O}(N)$  and hence the difference is negligible in large-scale limit.

**SELECT** is rather nontrivial; given a signal state as presented in Eq. (S54), the operation of **SELECT** shall satisfy

$$\begin{aligned}
 & \text{SELECT} |p_x, p_y, s_{\mathbf{p}}, q_x, q_y, s_{\mathbf{q}}, \alpha\rangle |\psi\rangle \\
 &= |p_x, p_y, s_{\mathbf{p}}, q_x, q_y, s_{\mathbf{q}}, \alpha\rangle \otimes \begin{cases} -\sigma_{p, s_{\mathbf{p}}}^Z |\psi\rangle & \text{if } (p, s_p) = (q, s_q), (\alpha_1, \alpha_2) = (0, 1) \\ \sigma_{p, \uparrow}^Z \sigma_{q, \downarrow}^Z |\psi\rangle & \text{if } p = q, (s_p, s_q) = (\uparrow, \downarrow), (\alpha_1, \alpha_2) = (1, 0) \\ \sigma_{p, s_p}^X \left( \prod_{p < r < q, s_r} \sigma_{r, s_r}^Z \right) \sigma_{q, s_q}^X |\psi\rangle & \text{if } p < q, s_p = s_q, |\mathbf{p} - \mathbf{q}| = 1, (\alpha_1, \alpha_2) = (0, 0) \\ \sigma_{q, s_q}^Y \left( \prod_{q < r < p, s_r} \sigma_{r, s_r}^Z \right) \sigma_{p, s_p}^Y |\psi\rangle & \text{if } q < p, s_p = s_q, |\mathbf{p} - \mathbf{q}| = 1, (\alpha_1, \alpha_2) = (0, 0) \end{cases} \quad (\text{S55})
 \end{aligned}$$

where the operation on subspace outside the signal state is unrestricted as long as  $\text{SELECT}^2 = I$  is satisfied. Note that comparison between  $p$  and  $q$  is based on the integer  $p = p_x + p_y M$  and  $q = q_x + q_y M$  while  $\|\mathbf{p} - \mathbf{q}\|$  denotes the Manhattan distance on the square lattice. Product-wise construction of **SELECT** oracle for the Fermi-Hubbard model has been suggested by Babbush et al., which pointed out that the construction can be done by structure shown in Fig. S15 with  $T$ -count of  $10N$ , as opposed to the one by the sequential type of  $22N$  [75].

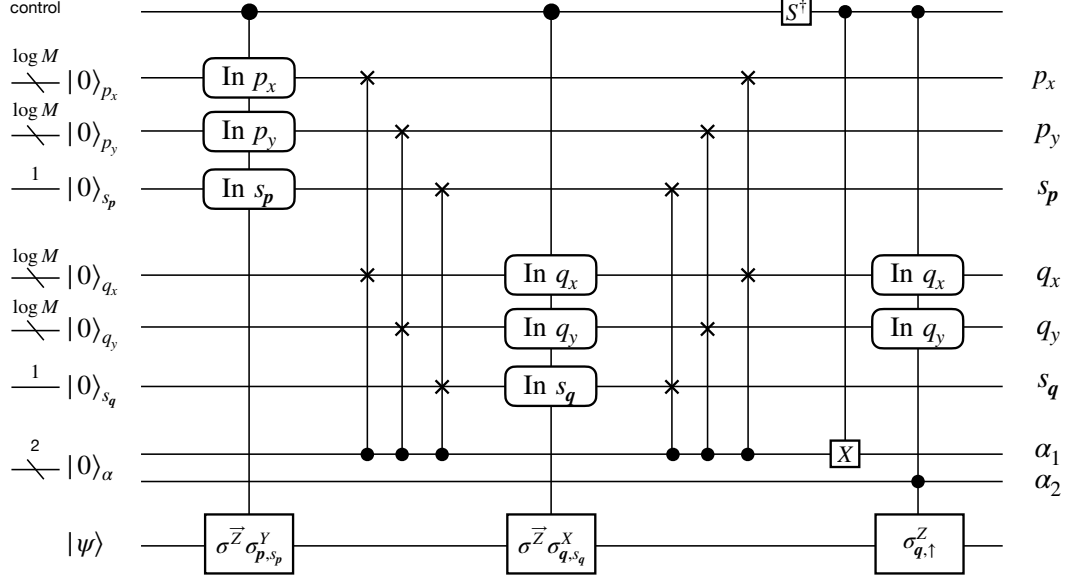


FIG. S15. Product-wise construction of **SELECT** for 2d Fermion Hubbard model on square lattice proposed in Ref. [75].

### 3. Spin-1 antiferromagnetic Heisenberg chain

Recall that the Hamiltonian of spin-1 antiferromagnetic Heisenberg chain reads

$$H = \sum_{p=1}^{N_{\text{site}}} \sum_{\alpha \in \{X,Y,Z\}} S_p^\alpha S_{p+1}^\alpha, \quad (\text{S57})$$

where  $S_p^\alpha$  is the spin-1 operator acting on the  $p$ -th site and  $N_{\text{site}}$  denotes the number of sites in the system. To render the problem compatible with quantum computers that take qubits as a elementary unit of quantum registers, we shall encode the system into enlarged Hilbert space spanned solely by qubits. In this regard, we represent each spin operator  $S_p^\alpha$  as a sum of Pauli operators as  $S_p^\alpha = \frac{1}{2} \sum_{\nu=1}^{2S} \sigma_{p,\nu}^\alpha$  and rewrite the Hamiltonian as

$$H = \frac{1}{4} \sum_{p=1}^{N_{\text{site}}} \sum_{\nu,\tau=1}^{2S} \sum_{\alpha \in \{X,Y,Z\}} \sigma_{p,\nu}^\alpha \sigma_{p+1,\tau}^\alpha. \quad (\text{S58})$$

Note that we also assume that the trial state for quantum phase estimation is also represented using the qubit encoding.

From the expression of Hamiltonian, we deduce that the **UNIT-PREP** circuit under periodic boundary condition can be composed as shown in Fig. S16 to generate the following state:

$$\text{UNIT-PREP } |0\rangle^{\log N_{\text{site}}+2} \mapsto \sum_{p,\alpha \in \{X,Y,Z\}} \sqrt{\frac{1}{\lambda}} |p\rangle |\alpha\rangle. \quad (\text{S59})$$

Correspondingly, the **SELECT** in the case of qubitization is constructed following the one presented in Fig. S12(a) such that

$$\text{SELECT } |p, \alpha, \nu, \tau\rangle |\psi\rangle = |p, \alpha, \nu, \tau\rangle \sigma_{p,\nu}^\alpha \sigma_{p+1,\tau}^\alpha |\psi\rangle, \quad (\text{S60})$$

which can be realized by the general sequential implementation of **SELECT** by  $T$ -count of  $48S^2N_{\text{site}} - 4$ . One may alternatively consider the product-wise implementation of **SELECT** as in Fig. S12(b) by consuming  $T$ -count of  $48SN_{\text{site}} - 4$ . However, we point out that there is no advantage in terms of  $T$ -count for  $S = 1$  case, while it requires additional  $\log N_{\text{site}}$  ancillary qubits. Therefore, we perform our runtime estimation based on the former implementation.

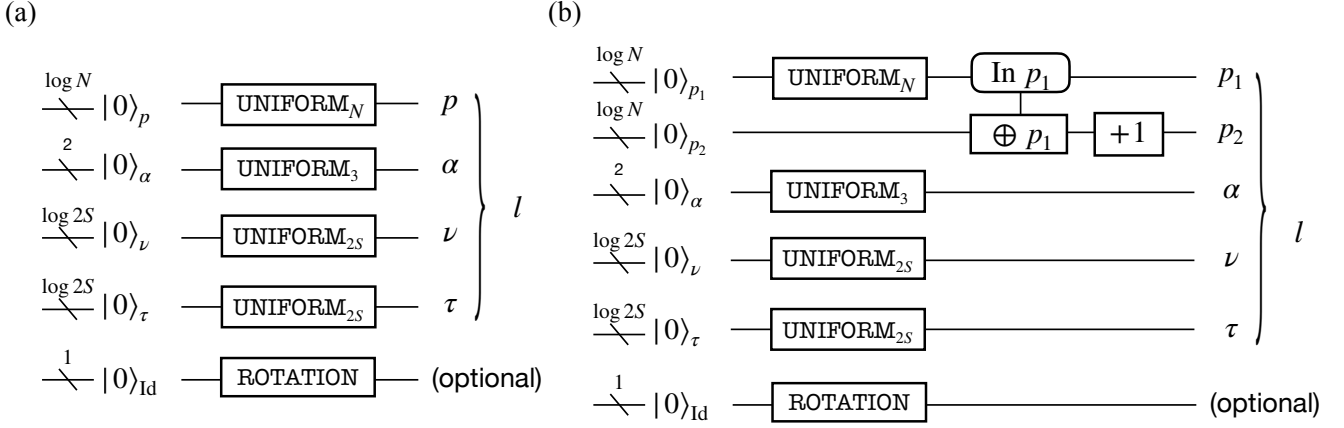


FIG. S16. Circuit structure of UNIT-PREP for spin-1 Heisenberg chain. We display both (a) sequential construction that consumes  $T$ -counts of  $8 \log N + 52 \log(1/\epsilon_{SS})$  and  $\log N + 2 \log S + O(1)$  ancillary qubits and (b) product-wise construction that consumes  $T$ -counts of  $16 \log N + 52 \log(1/\epsilon_{SS})$  and  $3 \log N + 2 \log S + O(1)$  ancillary qubits. Note that it is redundant to include `COPY_INDEX` and `SHIFT_INDEX` for (b), since the site index is unambiguously related with the interaction terms. If one desires to simulate the model under open boundary condition, one may add a qubit to take care of the boundary terms as described in Sec. S6.

Operation	$T$ -count
Addition/Subtraction [79] ( <code>COPY_INDEX</code> )	$4n$
Single-qubit rotation [80]	$10 + \Gamma \lceil \log_2(1/\epsilon_{SS}) \rceil$
<code>UNIFORM_L</code> [75]	$8 \log L + 12 \log(1/\epsilon_{SS})$
Arbitrary state synthesis [81]	$2^{n+1} - 2$ arbitrary rotations
Controlled operation	$T$ -count
$m$ -controlled addition/subtraction	$4(m-1) + 8n$
$m$ -controlled NOT	$\begin{cases} 0 & (m = 0, 1) \\ 4(m-1) & (m \geq 2) \end{cases}$
$m$ -control SWAP	$\begin{cases} 0 & (m = 0) \\ 4m & (m \geq 1) \end{cases}$
$m$ -controlled rotation	$8(m-1) + 20 + 2\Gamma \log_2(1/\epsilon_{SS})$

TABLE S7.  $T$ -count required to perform basic operations that involves  $n$  qubits. Here,  $\Gamma$  is a constant that takes 4 or 12 depending on whether the single-qubit rotation is within  $R_{x,y,z}$  or not, and  $\epsilon_{SS}$  denotes the accuracy of rotation synthesis.

## S5. COMPLEXITY OF BASIC QUANTUM OPERATIONS

Here we provide the details on the basic quantum operations that are used for circuit construction and  $T$ -count analysis.

One of the most important operation that are commonly used in various basic gates presented in Table S7 is the logical AND operation, whose explicit Clifford+ $T$  construction is provided in Fig. S17(a). Gidney showed that, by consuming ancillary qubits to store the temporal results of addition, we can implement  $n$ -qubit logical adder with  $T$ -count of  $4n + O(1)$  and controlled adder with  $8n + O(1)$  [79] (Fig. S17(b)). We further push the use of temporary ancilla qubit to reduce the  $T$ -count for other controlled operations, such as  $m$ -controlled addition, SWAP, or rotation (See Fig. S17(c), (d)). Also, we implement the `UNIFORM` operation following the construction scheme presented in Ref. [75].

## S6. SZEGEDY QUANTUM WALK WITH IMPERFECT PREPARE

In Sec. S3D, we have seen that the Szegedy-type quantum walk operator enables us to explore the energy spectra of the block-encoded Hermitian operator. In particular, the oracular unitaries can be implemented efficiently if the Hamiltonian exhibit spatially periodic structure with  $N_\alpha = O(1)$  types of interaction coefficients. However, this

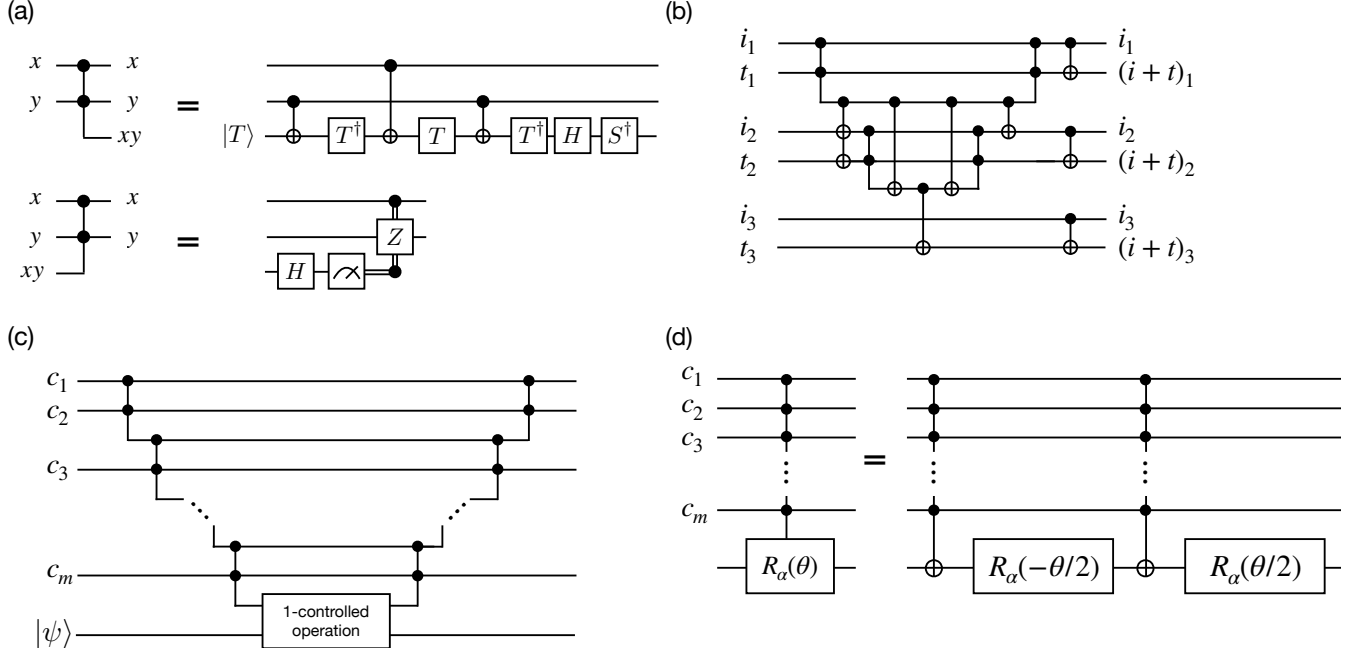


FIG. S17. Graphical representation of basic quantum operations. (a) Computation and uncomputation of logical AND operation. (b) 3-qubit logical adder. (c)  $m$ -controlled operation. (d)  $m$ -controlled rotation expressed using  $m$ -controlled NOT and single-qubit rotation.

argument strongly depends on the boundary condition; when the model is defined with open boundary condition or cylindrical boundary condition, the interaction configurations differ at the boundary sites, which affects the complexity of the PREPARE oracle in particular. Although the  $T$ -gate complexity of PREPARE remains to be  $\log(N/\epsilon)$  and therefore does not dominate the total cost even when we incorporate boundary effect, it is desirable to deal with minimal effort.

Here, we present a method that use homogeneous implementation of PREPARE and still extract simulation results for lattice systems defined under boundary conditions that are not necessarily periodic along all directions. To be concrete, we find that the error in the operation can be readily absorbed by constant shift in the Hamiltonian.

Let us first consider a perfect and also a slightly erroneous PREPARE operation that takes the ancillary system to the following states:

$$\text{PREPARE}_0 : |0\rangle^{\otimes a} \mapsto |\mathcal{L}_0\rangle = \sum_{l=1}^L \sqrt{\frac{w_l}{\lambda}} |l\rangle, \quad (\text{S61})$$

$$\text{PREPARE} : |0\rangle^{\otimes a} \mapsto |\mathcal{L}\rangle = \beta_1 |\mathcal{L}_0\rangle + \beta_2 |\perp\rangle, \quad (\text{S62})$$

where  $|\perp\rangle$  is orthogonal to any  $|l\rangle$ . Our goal is to perform unbiased simulation of Szegedy quantum walk so that the obtained results correctly extracts the eigenspectra of the Hamiltonian. One naive solution is to “correct” the state from  $|\mathcal{L}_0\rangle$  to  $|\mathcal{L}\rangle$  via, e.g., amplitude amplification. Meanwhile, by making use of the specific structure of SELECT considered in this work, we can eliminate the error with negligible cost. To be specific, we assume that the SELECT operates nontrivially only in the subspace  $\Pi\mathcal{H}\Pi$  where  $\Pi = (\sum_{l=1}^L I^{\otimes n} \otimes |l\rangle\langle l|)$  and  $\mathcal{H}$  is the total Hilbert space (confirm that this is satisfied in our construction presented in Sec. S3D.). Under such an assumption, we introduce a constant shift  $\gamma$  to the Hamiltonian to absorb the error. The overlaps are explicitly written as

$$(\langle \mathcal{L}_0| \otimes I) \text{SELECT}(|\mathcal{L}_0\rangle \otimes I) = \frac{H_0}{\lambda} + \gamma(-I), \quad (\text{S63})$$

$$(\langle \perp| \otimes I) \text{SELECT}(|\perp\rangle \otimes I) = I, \quad (\text{S64})$$

$$(\langle \perp| \otimes I) \text{SELECT}(|\mathcal{L}_0\rangle \otimes I) = 0, \quad (\text{S65})$$

which leads to

$$(\langle \mathcal{L}| \otimes I) \text{SELECT}(|\mathcal{L}\rangle \otimes I) = \frac{|\beta_1|^2 H_0}{\lambda} + (-\gamma|\beta_1|^2 + |\beta_2|^2)I. \quad (\text{S66})$$



Therefore, if we pick  $\gamma = |\beta_2|^2/|\beta_1|^2$ , we can simulate the rescaled version of Hamiltonian.

For concreteness, let us consider a case where we want to simulate a lattice system with cylindrical boundary condition using **PREPARE** that is intended for periodic boundary condition. We argue that the overhead due to the rescaling is negligible. This can be understood from the fact that the  $T$ -count for estimating the eigenenergy (at arbitrary precision) using the Taylorization or qubitization algorithm is proportional to  $\lambda$ . As can be seen from Eq. (S66), the L1 norm of the coefficient is amplified under the erroneous signal state  $|\mathcal{L}\rangle$  as  $\lambda \rightarrow \lambda/|\beta_1|^2$ . Since the ratio of coefficients is given as  $|\beta_2/\beta_1|^2 = \mathcal{O}((N^{\frac{d-1}{d}}/N)^2) = \mathcal{O}(N^{-2/d})$  in  $d$ -dimensional lattice systems with local interactions, we straightforwardly obtain  $|\beta_1|^2 \approx 1$ , and thus does not affect the overall cost up to the leading order. Throughout this work, for  $T$ -count and runtime analysis we assume to employ **PREPARE** oracle designed to implement a signal state for periodic boundary condition.

## S7. RUNTIME ANALYSIS OF QUBITIZATION-BASED QUANTUM PHASE ESTIMATION

### A. Overview

In this section, we explain the details of the runtime analysis for the quantum phase estimation that is based on the qubitization algorithm. As we have shortly mentioned in Sec. S3D, the runtime of quantum circuits represented with the Clifford+ $T$  formalism is typically evaluated with the number of  $T$ -gates, known as  $T$ -count, in the compiled quantum circuits. This is because each application of  $T$ -gates requires a time-consuming procedure consisting of magic-state injection, distillation, and teleportation in typical quantum error-correcting codes stabilized by Pauli operators. This is why we have compared the Hamiltonian simulation subroutines in Table I in the main text. While the  $T$ -count can capture the time-scaling of quantum algorithms when magic-state preparations are the most time-consuming factors, this estimation loses several vital factors in time analysis, and the actual execution time can vary a few orders of magnitudes depending on the strategy of compilation and executions. Here, we review several standard strategies and show how we calculated the execution times.

Throughout this paper, we assume the following situations: 1) Physical qubits are allocated on the vertices of 2d grids, which we call a qubit plane. 2) Logical qubits are encoded with surface codes [82–85]. 3) Logical operations on multiple logical qubits are performed with twist-based lattice surgery [86]. 4) The method introduced by Litinski [87] is applied to the construction of magic-state distillation, and purpose-specific strategies are employed for the compilation of **SELECT** and **PREPARE** oracles. Note that these assumptions may change or become unnecessary in the future by using devices with more flexible connectivity or employing other logical-operation strategies such as defect-pair braiding [85] and twist-free approach [88]. Nevertheless, we focus on the above scenario since they are standard assumptions in relevant studies on the runtime analysis [18, 89], and we leave the other scenario as future work.

### B. Surface code and lattice surgery

In fault-tolerant quantum computing with surface codes, each logical qubit is allocated as a  $d \times d$  block on the qubit plane, where  $d$  is the distance of surface codes. The error rates of logical qubits decrease exponentially with respect to  $d$ , as far as the error rates of physical qubits are smaller than the value called threshold. The required  $d$  is determined from physical error rates of given devices, logical-error suppression rate in error-correcting codes, and required logical error rates. During the computation, we repeat a subset of of Pauli measurements called stabilizer measurements, according to the generator set of a stabilizer group. A period for all the stabilizer Pauli measurements is called a code cycle. The recovery Pauli operations are estimated with a delay due to classical processing and stored in the unit logic called Pauli frame [84, 90].

All the basic logical operations must be achieved fault-tolerantly. The lattice surgery [86] is known to be the most promising strategy to efficiently achieve a multi-qubit logical operations in fault-tolerant quantum computing. In this strategy, the logical Pauli measurements on multiple logical qubits are realized by connecting corresponding blocks with a proper circumference, and all the logical Clifford operations are performed via the logical measurements using lattice surgery and logical  $H$  and  $S$  gates. The time required for the multi-qubit logical Pauli measurements with the lattice surgery is independent of the number of the target logical qubits but linearly scales to the code distance  $d$ . Thus, it is convenient to define another unit, code beat, as the latency of  $d$  code cycles. We need 2 code beats for logical  $S$  and CNOT gates and 3 code beats for logical  $H$  gates. Thanks to the nature of CSS codes, the latency for destructive single-qubit Pauli- $X, Z$  measurements and the preparation of the logical eigenstate of Pauli- $X, Z$  are finished within a single code cycle. Since we can take their latency into account by increasing the code beat, we neglect their latency hereafter.

The non-Clifford gates, such as  $T$  and Toffoli gates, cannot be performed with the combinations of the above, and are known to take a longer time compared with the other operations. These operations are achieved with the gate-teleportation technique that consume quantum resource named the magic states. For instance, when one desires to operate a  $T$ -gate through its teleportation, we need a logical qubit prepared in a magic state  $|A\rangle = 1/\sqrt{2}(|0\rangle + e^{i\pi/4}|1\rangle)$ . While the noisy preparation of magic states can be achieved with the magic-state injection protocol, its infidelity is unacceptable for fault-tolerant operations. Therefore, we must create a magic state from a protocol called the magic-state distillation, which allows generation of magic state with an arbitrarily small infidelity. A standard magic-state distillation protocol is 15-to-1 distillation. This protocol creates a single clean magic state from 15 noisy magic states to reduce the infidelity of magic state from  $p$  to  $35p^3$ , and succeeds with probability  $1 - 15p$  [84].

The latency of a single trial of magic-state injection requires constant code cycles. Typically, we need two-level distillation for the required logical error rate, and each generation requires 15 code beats [87]. Note that large code distances are not required at the first distillation level since we only need to protect noisy magic states during distillation. Thus, the latency may be smaller. We typically assign a region of the qubit plane just for repeating magic-state preparation, which we call a magic-state factory. The teleportation of non-Clifford gates requires the feedback of a Clifford operation or the adaptive change of consequent Pauli measurement basis.

Thus, successive gate teleportation will be blocked for a period of error-estimation delay, which is called a reaction time. The reaction time is determined by the throughput of the error-estimation algorithm for surface codes, physical error rates, chosen code distances, and its circuit implementation.

### C. Time estimation without topological restriction

Since we have readily introduced the overall framework of fault-tolerant quantum computation based on surface codes, now we explain how to estimate the runtime of circuits that are written in terms of Clifford+ $T$  formulation. If quantum circuits consume magic states with a constant rate, we can roughly estimate the execution time by counting the number of  $T$ -gate. On the other hand, the consumption rate of magic states is not necessarily constant and the execution time may be not linear to the number of  $T$ -gates. Fortunately, there is a canonical form proposed by Litinski [87] that ensures almost constant consumption rate of magic states. In this formalism, we convert the Clifford+ $T$  circuits to two stacks of layers; first one is a sequence of  $\pi/8$  Pauli rotations, and the latter is a sequence of Pauli measurements. The number of  $\pi/8$  Pauli rotations is equal to the number of  $T$ -gates  $N_T$ . The execution of  $\pi/8$  Pauli rotation consumes a single magic state, and is achieved with a single code beat and post-processing on the ancillary qubits.

As we detail in below, the appropriate estimation heavily relies on the hardware configuration. In the following, we introduce the  $T$ -count limited and reaction limited estimations as one of the most commonly employed estimation strategy. We subsequently point out their defects and explain how to overcome them by explicitly considering the *routing* of logical qubits.

The estimation of the execution time with the Clifford+ $T$  formalism in a qubit-restricted situation is simple. Assuming that we have a small qubit plane and the number of the magic-state factory is very restricted, we can expect that the latter Pauli measurement part is negligible compared to the first  $\pi/8$  rotation parts. Thus, the execution time can be estimated as the  $\tau_T N_T$ , where  $\tau_T$  is the average time for generating a magic state and teleporting it. This is called a  $T$ -count limited estimation. In the most pessimistic scenario, we can only place a single factory on the qubit plane and the consumption rate of  $T$ -gate is much more frequent than the generation rate of a magic state factory. In this case, the execution time can be obtained by multiplying the number of  $T$ -gates for **SELECT** and **PREPARE** oracles.

We can also consider the opposite scenario; we have a large qubit plane and can create an arbitrary many magic-state factories. In this case, we can effectively have an on-demand magic-state supply. Thus, we can teleport multiple  $T$ -gates as far as they can be executed in parallel. Therefore, we assume that each simultaneous application is achieved with  $\tau_{\text{group}} = \min(\tau_{\text{tel}}, \tau_{\text{react}})$ , where  $\tau_{\text{tel}}$  is the latency of lattice-surgery operations for the magic-state teleportation and  $\tau_{\text{react}}$  is the reaction time. This quantity is directly related with the execution time as  $D_T \tau_{\text{group}}$ , where  $D_T$  is the number of  $T$ -depth. When  $\tau_{\text{tel}} > \tau_{\text{react}}$ , we can hide the latency  $\tau_{\text{tel}}$  by time-optimal construction [87, 91]. With ancillary qubits, we can convert the iterations of gate teleportation to parallel teleportation and a sequence of reactions. When we can utilize  $K$  times larger qubit space, we can force  $\tau_{\text{group}} \sim D_T \tau_{\text{tel}}/K + D_T \tau_{\text{react}}$ . This situation is called a reaction-limited. An actual scenario would be the intermediate of the above two, and the actual execution time varies according to the size of the available qubit plane size.

It should be noted that the above estimations ignore the topological restriction of the qubit plane. Since each logical qubit is placed at a certain position on the qubit plane and we need to connect the target blocks for lattice surgery, we sometimes cannot execute operations due to the conflict of their paths. This means  $T$ -gates are not necessarily teleported in parallel even if they are located in parallel on the quantum circuits. To take them into account, we need to consider the allocation and routing of logical qubits, which is discussed later.

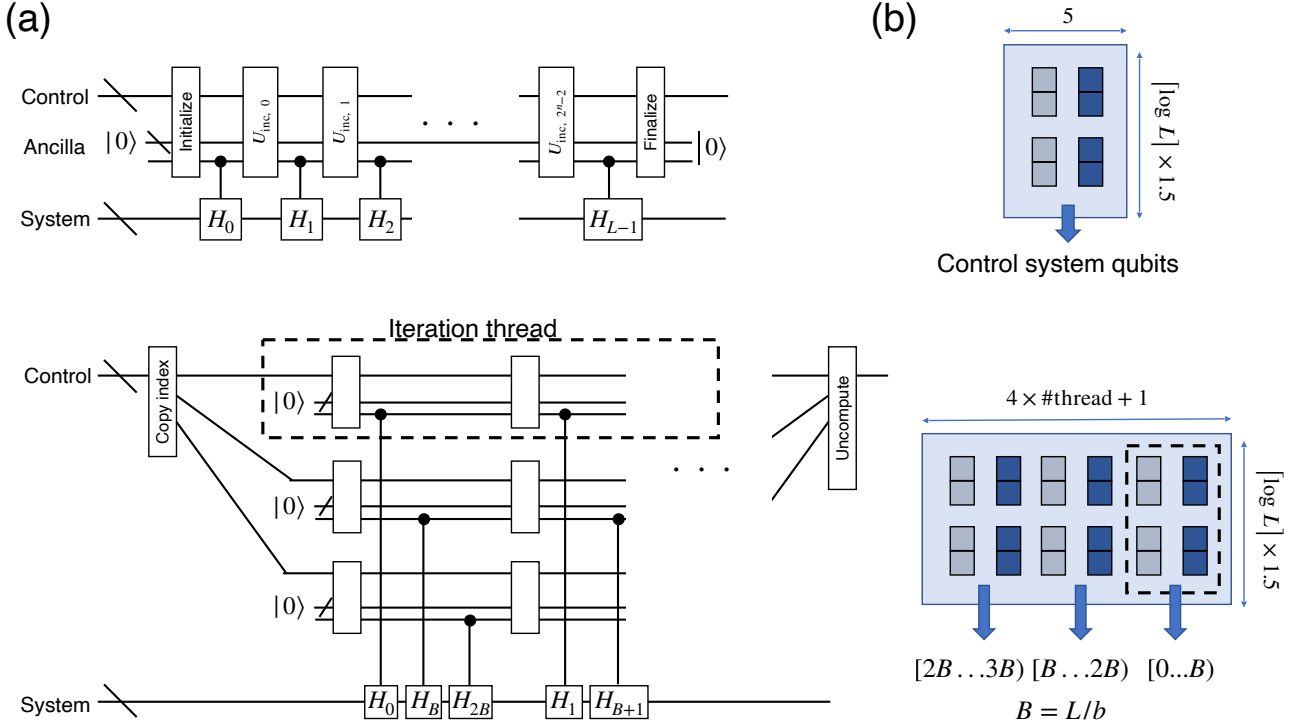


FIG. S18. (a) Quantum circuits showing the concept of parallelization for SELECT operations. (b) The floor plans for SELECT control qubits with and without the parallelization technique.

We also note that a similar technique can be applied to the formalism by Litinski [87]. We can divide a sequence of  $\pi/8$  Pauli rotations into several commuting groups. Since the feedback incurred by the Pauli rotations in the same commuting group are independent,  $D_T$  is equal to the number of commuting rotation groups. On the other hand, since the canonicalization of Litinski's format induces  $\pi/8$  rotations acting on a massive number of logical qubits, and thus the achieved  $T$ -depth is expected to be far from the optimal. This motivates us to construct a qubitization-specific minimization of the  $T$ -depth [89].

The quantum circuits of qubitization-based quantum phase estimation consist of iterations of SELECT and PREPARE oracles. In the case of the ground-state energy estimation for condensed matter Hamiltonians, the coefficients of Hamiltonians are nearly uniform, and therefore the execution time is expected to be dominated by SELECT modules (See Sec. S3 D). A standard SELECT operation is constructed as a serial sequence of Toffoli gates, and its  $T$ -depth is almost equal to  $T$ -count. This means there is no room to reduce  $T$ -depth even when several magic-state factories are available. To enable a flexible performance tuning of SELECT operations according to available magic-state supply rates, we show a technique to reduce the  $T$ -depth with a similar idea of loop-parallelization (See Fig. S18). Suppose that the target Hamiltonian consists of  $L$  terms of Pauli operators acting on  $n$  qubits. In this technique, we divide the task of SELECT operations to  $b$  parallelized executions using  $b$  times the number of control qubits as follows. First, we clone the input control registers to GHZ states  $\sum_x \alpha_x |x\rangle \mapsto \sum_x \alpha_x |x\rangle^{\otimes b}$ , and we call each cloned registers as a thread. Then, we divide the  $L$  terms to  $b$  blocks, where the  $i$ -th block contains from the  $iL/b$ -th to  $(i+1)L/b - 1$ -th terms, and SELECT operations is performed as  $b$  independent iterations by  $b$  threads. Finally, we uncompute the cloned registers. This construction effectively reduces the  $T$ -depth from  $O(L)$  to  $O(L/b + \log L)$  with an additional  $O(b \log n)$  qubits. The brief construction of this parallelization is shown in Fig. S18 (a). Note that as far as we keep  $b$  sufficiently small than  $n$ , the overhead of  $O(b \log n)$  ancillary qubits would be negligible compared to the system size  $n$ . The detailed decomposition and parallelization efficiency will be presented in another paper.

#### D. Placement of logical qubits and routing for lattice surgery

Once quantum circuits are translated to the sequence of intrinsic lattice-surgery operations, we need to place each logical qubit to a certain block on the qubit plane. While we should choose dense allocations to avoid the redundant

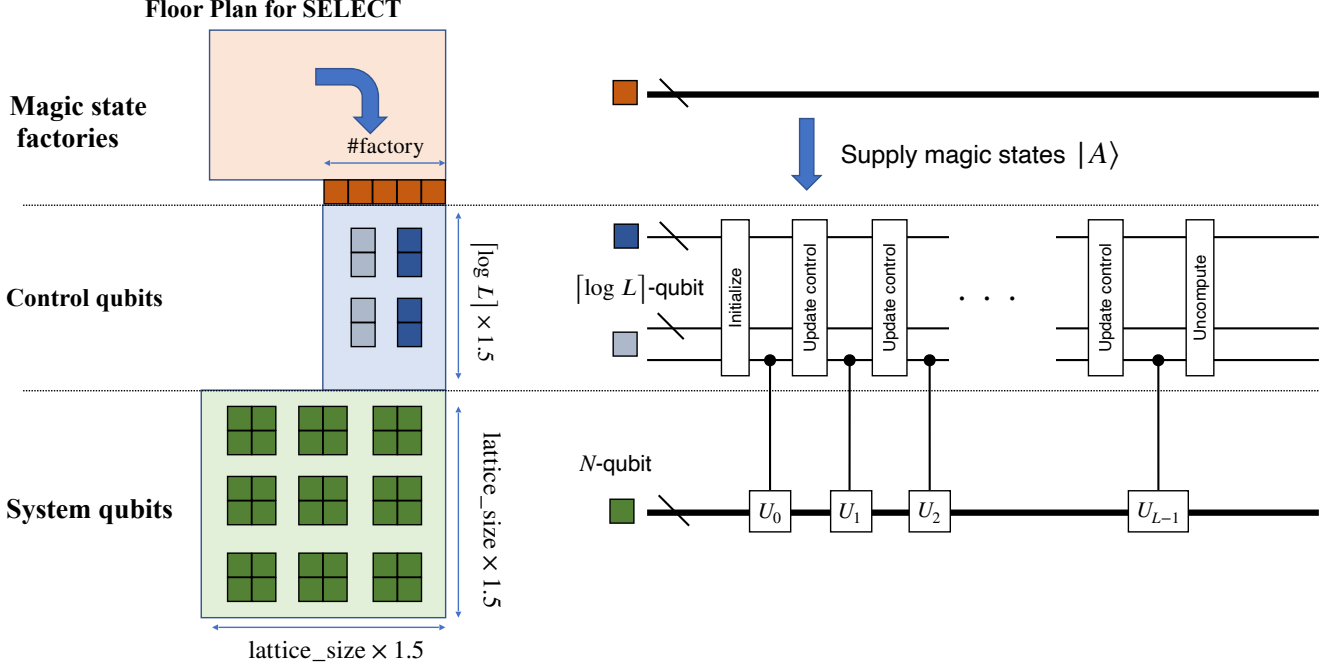


FIG. S19. The floor plan of the qubit plane for the sequential construction of the **SELECT** operation.

usage of the qubit plane, too dense allocations may lead to path conflicts and the degradation of instruction throughput. In this paper, we heuristically designed the placement of logical qubits for condensed matter Hamiltonians for 2d spins by utilizing the feature of spatially local interactions, as shown in Fig. S19. In our design, the qubit plane is divided into three parts; factory, control, and system. We allocate logical qubits for storing the system qubits in each row of system space so that vertical and horizontal edges of each logical qubit block touch a corridor of ancillary logical qubits, i.e., there is  $\sqrt{n}$  corridors with  $\sqrt{n}$  length. We place the control part at the side of the system blocks, and the magic state factories are placed behind it. The logical qubits of control and system parts are separated with corridors to make room for lattice surgery. In the **SELECT** operations, a single ancillary qubit performs controlled operations on system parts. Thus, we allocate the qubit at the nearest position to the system part.

When we utilize the parallelization to the control part, we modify the floor plan as shown in Fig. S18(b). If the threads are randomly allocated, all the thread tries to touch target logical qubits on the system part, and conflicts may occur during the operations. This problem can be resolved by re-ordering the Pauli terms and appropriate block allocations. Since we now consider nearly uniform coefficients, the cost of **PREPARE** oracle is almost independent from the ordering of coefficients. Thus, we can change the order of Pauli terms to minimize the execution time for **SELECT** operations. Suppose the list of sorted indices in the  $i$ -th Pauli operator is  $(j_1, \dots, j_k)$ . Then, we sort the Pauli terms with the set in ascending order, separate them into  $b$  blocks, and assign them to each thread. When the thread number  $b$  satisfies  $\sqrt{n} > b$ ,  $\sqrt{n}/b + k$  corridors are relevant to each thread. With this assignment, there are no potential conflict as far as  $k < \sqrt{n}/b$ . Thus, we can expect this assignment will prevent the potential conflict of lattice-surgery paths.

### E. Parameter estimation and numerical evaluation

Here, we estimate the relevant parameters according to the recent device technologies. We define  $d$ ,  $L$ , and  $m$  as a code distance, the number of terms in the target Hamiltonian, and the required digit of the ground energy, respectively. They are left as variables since they depend on the problem size. While a shorter code cycle is preferable to shorten the execution time, it is lower-bounded by the time for stabilizer measurements and error estimation algorithms. Currently, the latter is the dominant factor and is expected to be no shorter than  $1 \mu\text{s}$  [92]. Thus, the code beat, which is defined by  $d$  code cycles, is  $d \mu\text{s}$ . The time for two-level magic-state distillation  $\tau_T$  is  $15d \mu\text{s}$ . The reaction

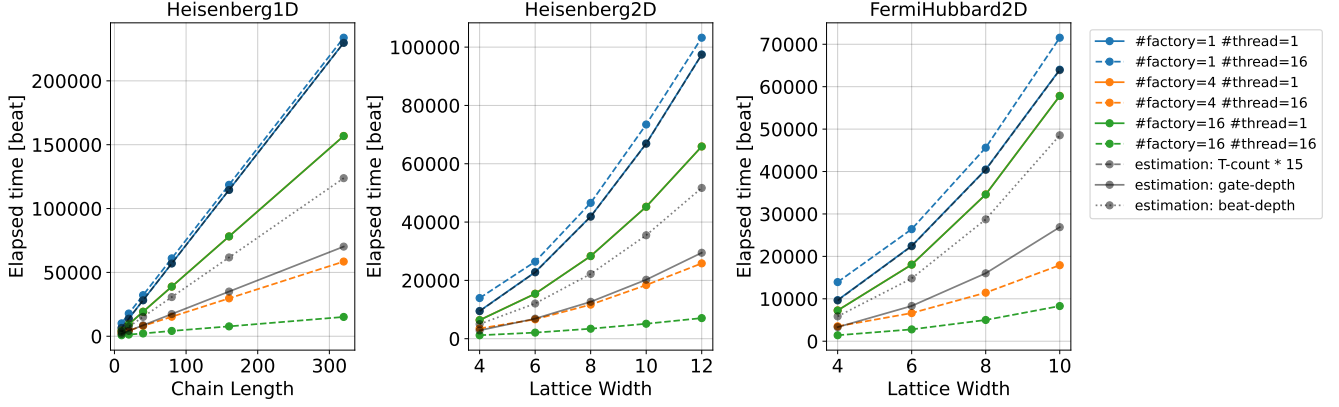


FIG. S20. The required code beats for executing SELECT operations for several Hamiltonian models.

time is typically assumed to be  $10 \mu\text{s}$ . The  $T$ -count for the SELECT operation is  $4L$  and the  $T$ -depth is  $4L/b$ , where  $b$  is a parallelization level.

Summarizing the above, we can estimate the total execution time using several variables depending on the problem. In the case of  $T$ -count limited scenario, the execution time for SELECT operation is about  $15d [\mu\text{s}] \times 4L = 60dL [\mu\text{s}]$ . In the case of  $T$ -depth limited case, the execution time for SELECT operation is  $10 [\mu\text{s}] \times 4L/b = 40L/b [\mu\text{s}]$ , which is  $bd$  times smaller than the  $T$ -count limited case. Assuming the other parts, such as PREPARE, initial-state preparation, and quantum Fourier transform, are negligible compared to the SELECT, the whole execution time can be estimated by multiplying  $2^m$  (or number of repetitions determined as  $r = \pi\lambda/2\epsilon$  as discussed in Sec. S3D) to that for SELECT.

Finally, we verified our analysis with numerical calculation. We have synthesized the quantum circuits of SELECT operations with and without parallelization, allocate logical qubits as shown in the floor plan, determine the routing of lattice surgery with depth-first search algorithms, and calculate the required code beat for SELECT circuits with simulation. The observed coded beats to finish SELECT operations are plotted as a function of problem sizes and the type of Hamiltonians in Fig. S20. In the numerical simulation, we used the following approximations to simplify the evaluation:

- We assumed each magic-state factory generates a single magic state per 15 code beat. Note that this value may be improved by using more efficient magic-state distillation strategy, such as the construction proposed in Ref. [84, 87].
- When Clifford operations are conditioned by previous measurement outcomes, the operations are error-corrected and become available after 1 code beat.
- While logical  $S$  gates are required after  $T$ -gate teleportation with only probability of 0.5, we pessimistically assume that the logical  $S$  gate is always required.
- Due to the implementation of PREPARE,  $L$  Hamiltonian terms are not necessarily assigned to the computational basis from  $|0\rangle$  to  $|L-1\rangle$  in the control qubits. Nevertheless, we assumed it is enough to iterate from 0-th to  $L-1$ -th for simplicity. The conciliation between the cost of SELECT and PREPARE is future work.

According to the numerical results, when we do not perform parallelization and only have a single factory (solid blue line), the runtime is close to the product of the rate of magic-state generation and  $T$ -count (broken black line). When the number of factories increases to 4, the runtime saturates at about half of  $T$ -count limited estimation (solid green line). Compared to the depth of circuit (black dotted line), it is about 1.2 times larger. We expect that this discrepancy comes from the latency of reactions or path conflicts. When we employ parallelization, the runtime can be reduced to a smaller value while it requires a larger number of qubits and factories. With four threads and 16 factories, the runtime can be suppressed to 0.1 times smaller values. Thus, we can conclude that when there are several magic-state factories, the parallelization is effective in further reducing the computational time with a small overhead of required logical qubits. The required code beats for all the configurations are summarized in Table. S8.

TABLE S8. The calculated runtimes for a single **SELECT** operations for several Hamiltonian models. The execution times are shown with the unit of code beats, and  $n_F$  means the number of magic-state factories. The runtime in terms of expected walltime is shown in Table S9.

Hamiltonian	lattice size	#thread	runtime [beat] ( $n_F = 1$ )	runtime [beat] ( $n_F = 4$ )	runtime [beat] ( $n_F = 16$ )
2d $J_1$ - $J_2$ Heisenberg	$4 \times 4$	1	9511	6389	6374
2d $J_1$ - $J_2$ Heisenberg	$4 \times 4$	16	13939	3514	1185
2d $J_1$ - $J_2$ Heisenberg	$6 \times 6$	1	22840	15433	15412
2d $J_1$ - $J_2$ Heisenberg	$6 \times 6$	16	26419	6634	2091
2d $J_1$ - $J_2$ Heisenberg	$8 \times 8$	1	41929	28348	28327
2d $J_1$ - $J_2$ Heisenberg	$8 \times 8$	16	46583	11678	3424
2d $J_1$ - $J_2$ Heisenberg	$10 \times 10$	1	66958	45261	45239
2d $J_1$ - $J_2$ Heisenberg	$10 \times 10$	16	73465	18400	5127
2d $J_1$ - $J_2$ Heisenberg	$12 \times 12$	1	97498	65939	65917
2d $J_1$ - $J_2$ Heisenberg	$12 \times 12$	16	103225	25840	7065
spin-1 Heisenberg chain	10	1	6559	4441	4407
spin-1 Heisenberg chain	10	16	10093	2547	780
spin-1 Heisenberg chain	20	1	13828	9391	9355
spin-1 Heisenberg chain	20	16	17779	4472	1308
spin-1 Heisenberg chain	40	1	28237	19227	19185
spin-1 Heisenberg chain	40	16	32179	8072	2172
spin-1 Heisenberg chain	80	1	57046	38887	38845
spin-1 Heisenberg chain	80	16	60983	15278	4157
spin-1 Heisenberg chain	160	1	114655	78208	78165
spin-1 Heisenberg chain	160	16	118585	29680	7728
spin-1 Heisenberg chain	320	1	229864	156848	156805
spin-1 Heisenberg chain	320	16	233789	58484	15116
2d Fermi-Hubbard	$4 \times 4$	1	9688	7267	7252
2d Fermi-Hubbard	$4 \times 4$	16	13939	3515	1407
2d Fermi-Hubbard	$6 \times 6$	1	22477	18069	18048
2d Fermi-Hubbard	$6 \times 6$	16	26419	6631	2787
2d Fermi-Hubbard	$8 \times 8$	1	40486	34609	34588
2d Fermi-Hubbard	$8 \times 8$	16	45623	11439	5007
2d Fermi-Hubbard	$10 \times 10$	1	64015	57837	57815
2d Fermi-Hubbard	$10 \times 10$	16	71545	17920	8290

## S8. ESTIMATION OF THE NUMBER OF PHYSICAL QUBITS, CODE DISTANCES, AND ACTUAL RUNTIME

Here, we explain how to estimate required number of physical qubits  $N_{\text{ph}}$  via determining the code distance  $d$  of the surface code. Once the code distance is determined, we may combine all the results and further estimate the actual runtime required for the qubitization-based phase estimation algorithm.

We assume that the qubits are allocated as depicted in the floor plan of Fig. S19 which consists of system qubits, control qubits, and magic state factory. By assuming that all logical qubits are encoded by framework of surface code with homogeneous code distance of  $d$ , the number of physical qubits  $N_{\text{ph}}$  is provided as

$$N_{\text{ph}} = (1.5^2 N_S + 1.5(4b + 1) \log L + n_F A_F) \times (2d^2), \quad (\text{S67})$$

where  $N_S$  is number of system qubits,  $b$  is the number of parallelization threads,  $n_F$  is the number of magic state factory, and  $A_F$  is the floor area per single magic state factory. In our estimation, we follow the construction of Ref. [87] and employ  $A_F = 176$ . Meanwhile, as was also noted in Sec. S7B, we may reduce the code distance of logical qubits that are used for the first-level magic state distillation (e.g. two-fold), which results in significant reduction of physical qubits especially when number of magic state factories  $n_F$  is large.



An important factor that cannot be determined solely from hardware configuration or Hamiltonian size is the code distance  $d$ . Here, we take sufficiently large  $d$  so that the logical error rate  $p_{\log}$  is smaller than the number of logical operations  $N_{\text{op}}$ :

$$p_{\log} < 1/N_{\text{op}}, \quad (\text{S68})$$

where we estimate  $p_{\log} = 0.1(p/p_{\text{th}})^{(d+1)/2}$  with the ratio of physical error rate over error threshold  $p/p_{\text{th}} = 0.1$ . Note that this choice has been commonly employed in existing runtime estimation literature such as Refs. [18, 19, 87]. The number of logical operations is roughly estimated from the repetition count  $r$  of qubitization oracle by neglecting the contribution from the subdominant PREPARE oracle as

$$N_{\text{op}} = (\# \text{logical qubits involved in SELECT}) \times (\# \text{code cycle per SELECT}) \times r. \quad (\text{S69})$$

By solving Eq. (S68) using these quantities, we find that it is sufficient to take  $d$  around 21 or 25 around the quantum-classical crosspoint.

The total runtime can be estimated as

$$t \sim t_{\text{beat}} \times N_{\text{beat}} \times r, \quad (\text{S70})$$

where  $t_{\text{beat}} = t_{\text{cycle}} \times d$  is the required time per code beat that is determined from the time per code cycle of surface code  $t_{\text{cycle}} = 1 \mu\text{s}$ , and  $N_{\text{beat}}$  is the number of code beat per SELECT oracle obtained in Sec. S7. The overall runtime estimation results and quantum resource are summarized in Table S9, which is displayed in comparison with classical algorithms in Fig. 3 in the main text. Here, we clearly observe that quantum advantage is achieved in runtime of hours, with use of physical qubits of  $O(10^5)$ .

Our results imply that code distance 21 is the minimum requirement to demonstrate the quantum advantage under the assumption of  $p/p_{\text{th}} = 0.1$  and target of  $\epsilon = 0.01$  (See Sec. S8 A for discussion with various hardware/algorithmic requirements.). In other words, we need a classical control unit of FTQC that can estimate/correct (non-logical) errors of  $d = 21$  logical qubits with  $10^{-3}$  physical error rate and  $1 \mu\text{s}$  code cycle. However, according to Ref. [93], the current state-of-the-art implementation of lattice-surgery-compatible error decoders allows a code distance up to 11 with these assumptions. Therefore, achieving physical error rates ten-times smaller than the code threshold and increasing the number of qubits are not enough to demonstrate quantum computational advantage in the field of condensed matter physics.

We expect several possible directions to overcome this difficulty. First, as we discuss more in detail in Sec. S8 A, achieving smaller physical error rates can reduce the required code distance and number of physical qubits. The execution times are also reduced since it is proportional to code distances. Second strategy is to improve encoding strategies and error-estimation algorithms for quantum error correction, which effectively increase the code threshold or allowed code distances. Third, increasing physical qubits allows more allocations of magic-state factories, which enables further parallelization of SELECT modules and reduction of the required code distances. Fourth, there is room for improving the workspace utilization for lattice surgery. We can use prepared logical Bell pairs [89] for more efficient scheduling, re-use dirty logical qubits [94], or find more suitable Hamiltonian models to demonstrate advantage. Finally, we can utilize longer code cycles to allow larger code distances. However, it should be noted that this approach also increases the runtime, and more resources are demanded to demonstrate an advantage. A possible direction is considering heterogeneous architecture, i.e., using superconducting qubits for the frequent-access region and ion qubits for low-access regions, but this requires careful consideration of the communication bandwidth between different qubit species. We expect that one of these approaches cannot solely resolve the problems, and the co-design of the application, algorithm, system, and hardware is demanded in future. Our resource estimation is the first step towards such advanced designs.

#### A. Quantum resource under various algorithmic/hardware requirements

Up to now, we have discussed thoroughly under assumption of 1) using hardware that consists of physical qubits with error rate of  $p = 10^{-3}$ , 2) performing computation that aims for constant total energy accuracy  $\epsilon = 0.01$ . Meanwhile, as we have shortly mentioned in the previous section, it is informative to modify the hardware/algorithmic requirements to explore variation of quantum-classical crosspoint. For instance, we find from Eq. (S68), (S70) that the code distance depends on  $p$  and  $\epsilon$  as

$$d = O\left(\frac{\log(N/\epsilon)}{\log(p)}\right). \quad (\text{S71})$$

Note that this also affects the number of physical qubits via the number of physical qubit per logical qubit  $2d^2$ . We visualize the above relationship explicitly in Fig. S21, which considers the near-crosspoint regime of 2d  $J_1$ - $J_2$

Hamiltonian	lattice size	$(n_F, \#thread)$	code distance $d$	$N_{ph}$	Repetition count $r$	Runtime [sec]
2d $J_1$ - $J_2$ Heisenberg	$4 \times 4$	(1, 1)	19	1.93e+05	4.71e+03	8.52e+02
2d $J_1$ - $J_2$ Heisenberg	$4 \times 4$	(16,16)	17	2.06e+06	4.71e+03	9.49e+01
2d $J_1$ - $J_2$ Heisenberg	$6 \times 6$	(1, 1)	21	2.83e+05	1.13e+04	5.42e+03
2d $J_1$ - $J_2$ Heisenberg	$6 \times 6$	(16,16)	19	2.69e+06	1.13e+04	4.49e+02
2d $J_1$ - $J_2$ Heisenberg	$8 \times 8$	(1, 1)	23	4.13e+05	2.07e+04	2.00e+04
2d $J_1$ - $J_2$ Heisenberg	$8 \times 8$	(16,16)	21	3.42e+06	2.07e+04	1.49e+03
2d $J_1$ - $J_2$ Heisenberg	$10 \times 10$	(1, 1)	23	5.05e+05	3.30e+04	5.08e+04
2d $J_1$ - $J_2$ Heisenberg	$10 \times 10$	(16,16)	21	3.55e+06	3.30e+04	3.55e+03
2d $J_1$ - $J_2$ Heisenberg	$12 \times 12$	(1, 1)	25	7.25e+05	4.81e+04	1.17e+05
2d $J_1$ - $J_2$ Heisenberg	$12 \times 12$	(16,16)	23	4.42e+06	4.81e+04	7.81e+03
spin-1 Heisenberg chain	10	(1, 1)	19	4.36e+05	4.90e+03	6.91e+02
spin-1 Heisenberg chain	10	(16,16)	17	2.57e+07	4.90e+03	6.80e+01
spin-1 Heisenberg chain	20	(1, 1)	21	9.03e+05	9.61e+03	3.16e+03
spin-1 Heisenberg chain	20	(16,16)	19	6.22e+07	9.61e+03	2.46e+02
spin-1 Heisenberg chain	40	(1, 1)	23	1.97e+06	1.90e+04	1.40e+04
spin-1 Heisenberg chain	40	(16,16)	19	1.22e+08	1.90e+04	8.52e+02
spin-1 Heisenberg chain	80	(1, 1)	25	4.43e+06	3.79e+04	6.12e+04
spin-1 Heisenberg chain	80	(16,16)	21	2.96e+08	3.79e+04	3.51e+03
spin-1 Heisenberg chain	160	(1, 1)	25	8.63e+06	7.56e+04	2.46e+05
spin-1 Heisenberg chain	160	(16,16)	23	7.07e+08	7.56e+04	1.48e+04
spin-1 Heisenberg chain	320	(1, 1)	27	1.99e+07	1.51e+05	1.06e+06
spin-1 Heisenberg chain	320	(16,16)	25	1.67e+09	1.51e+05	6.29e+04
2d Fermi-Hubbard ( $U = 4$ )	$4 \times 4$	(1, 1)	21	2.65e+05	1.63e+04	3.32e+03
2d Fermi-Hubbard ( $U = 4$ )	$4 \times 4$	(16,16)	19	2.58e+06	1.63e+04	4.37e+02
2d Fermi-Hubbard ( $U = 4$ )	$6 \times 6$	(1, 1)	23	4.23e+05	3.77e+04	1.95e+04
2d Fermi-Hubbard ( $U = 4$ )	$6 \times 6$	(16,16)	21	3.33e+06	3.77e+04	2.21e+03
2d Fermi-Hubbard ( $U = 4$ )	$8 \times 8$	(1, 1)	23	5.63e+05	6.79e+04	6.32e+04
2d Fermi-Hubbard ( $U = 4$ )	$8 \times 8$	(16,16)	23	4.22e+06	6.79e+04	7.81e+03
2d Fermi-Hubbard ( $U = 4$ )	$10 \times 10$	(1, 1)	25	8.74e+05	1.07e+05	1.71e+05
2d Fermi-Hubbard ( $U = 4$ )	$10 \times 10$	(16,16)	23	4.46e+06	1.07e+05	2.04e+04

TABLE S9. The estimated number of physical qubits, required code distance, and actual runtime for our target Hamiltonians.

Heisenberg model and 2d Fermi-Hubbard model. It can be seen from Fig. S21(a),(b),(d),(e) that the improvement of the error rate directly triggers the reduction of required code distance, which results in significant suppression of number of physical qubits. This is even better captured by Fig. S21(c) and (f). By achieving the physical error rate of  $p = 10^{-4}$  or  $10^{-5}$ , for instance, one may realize 4-fold or 10-fold reduction of the number of physical qubits.

We find that the target accuracy  $\epsilon$  does not play a significant role in terms of qubit counts; it is rather relevant with the runtime, since the total runtime scaling is given as

$$t = O\left(\frac{\log(N/\epsilon)}{\epsilon \log(p)}\right), \quad (\text{S72})$$

which now shows *polynomial* dependence on  $\epsilon$ . As is highlighted in Fig. S22, we observe that in the regime with higher  $\epsilon$  the computation is completed within minutes. However, we do not regard such a regime as optimal field for the quantum advantage. The runtime of classical algorithms typically show higher-power dependence on  $\epsilon$ . Classical algorithms, therefore, are likely to run even faster than quantum algorithms with large  $\epsilon$ . We thus argue that the setup of  $\epsilon = 0.01$  provides a platform that is both plausible by quantum algorithm and challenging by classical algorithm (DMRG).

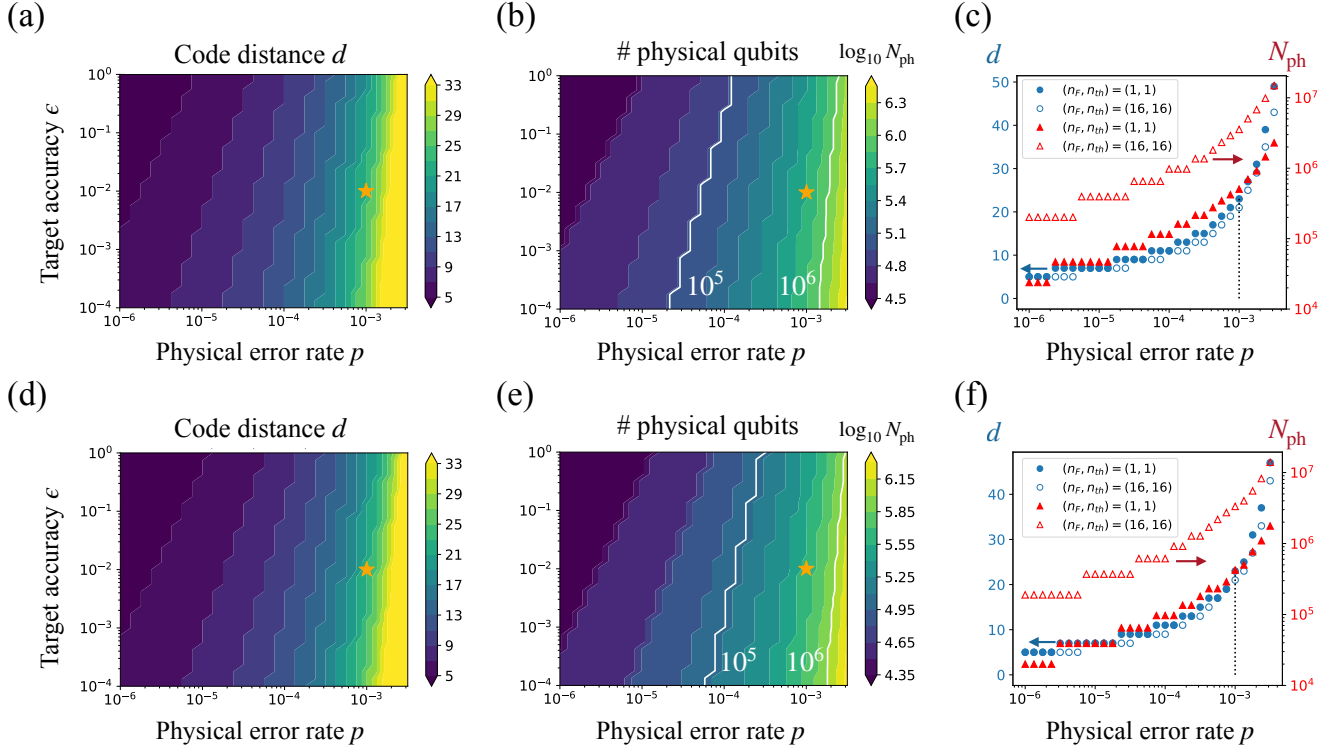


FIG. S21. Requirements for logical and physical qubits by the phase estimation algorithm based on the qubitization to achieve target accuracy  $\epsilon$  with physical error rate  $p$ . The panels denote (a) code distance  $d$  and (b) number of physical qubits  $N_{\text{ph}}$  required to simulate the ground state of 2d  $J_1$ - $J_2$  Heisenberg model with lattice size of  $10 \times 10$  with  $J_2 = 0.5$ . Here, the qubit plane is assumed to be organized as  $(n_F, \text{\#thread}) = (1, 1)$ . The setup used in the maintext,  $\epsilon = 0.01$  and  $p = 10^{-3}$ , is indicated by the orange stars. (c) Focused plot at  $\epsilon = 0.01$ . Blue and red points show the results for code distance  $d$  and  $N_{\text{ph}}$ , respectively, where the filled and empty markers correspond to floor plans with  $(n_F, \text{\#thread}) = (1, 1)$  and  $(16, 16)$ , respectively. (d-f) Plots for 2d Fermi-Hubbard model of lattice size  $6 \times 6$  with  $U = 4$ , corresponding to (a-c) for the Heisenberg model.

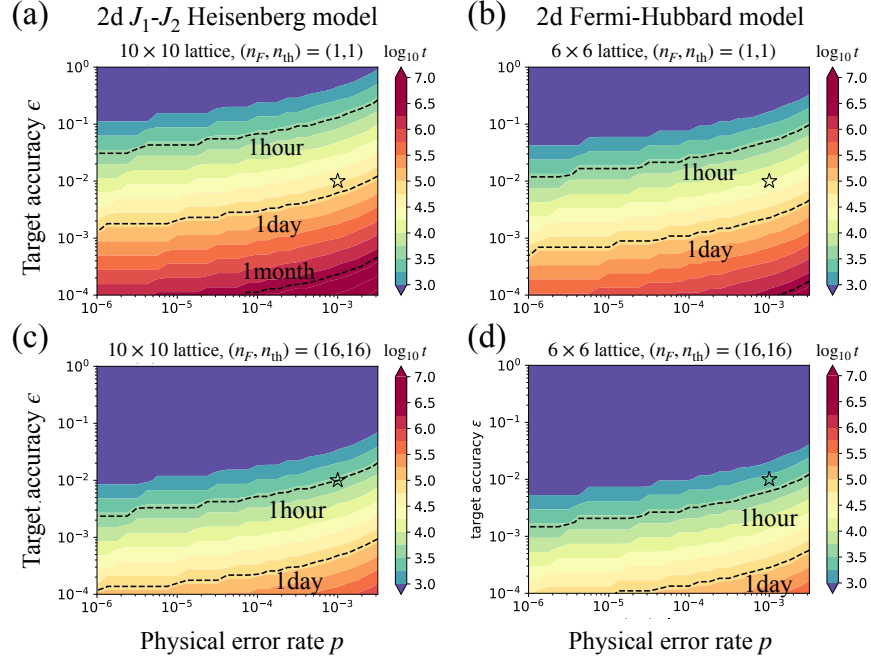


FIG. S22. Estimated runtime for various simulation setups for (a), (c) 2d  $J_1$ - $J_2$  Heisenberg model of lattice size  $10 \times 10$  with  $J_2 = 0.5$  and (b), (d) 2d Fermi-Hubbard model of lattice size  $6 \times 6$  with  $U = 4$ . The floor plan of the qubit plane is assumed as  $(n_F, \#thread) = (1, 1)$  and  $(16, 16)$  for (a),(b) and (c),(d), respectively. The setup  $\epsilon = 0.01$  and  $p = 10^{-3}$ , as employed in the maintext, is shown by the black open stars.